

Next-Generation Polarized ^3He Targets for Electron Scattering Experiments

Yunxiao Wang

Anqing, Anhui, China

B.S. in Physics University of Science and Technology of China May 2009

A Dissertation presented to the Graduate Faculty
of the University of Virginia in Candidacy for the Degree of
Doctor of Philosophy

Department of Physics

University of Virginia

Dec, 2016

Abstract

Historically, ^3He targets for electron scattering experiments have been polarized through spin-exchange optical pumping (SEOP). Polarized laser light passes its circular polarization to alkali metal vapor, which then transfers its polarization to ^3He through spin-exchange collisions.

This thesis discusses the basics of SEOP and the polarimetry techniques used in our lab. Narrowband laser and alkali-hybrid SEOP have improved the performance of targets significantly. In alkali-hybrid SEOP, potassium is used together with rubidium for transferring polarization to ^3He nuclei. We discussed the data collected over many pure-rubidium targets and alkali-hybrid targets. In the course of analyzing the data, we also studied the “X factor” which limits the highest achievable polarization of ^3He .

Because the experiments planned for the 12GeV era in Jefferson National Laboratory (JLAB) will use much higher electron beam current, we are exploring the possibility of using metal (instead of glass) as the entry points (commonly referred to as “end windows”) for future targets. We established the metal composition and developed the techniques to incorporate metal to targets without introducing significant spin-relaxation rates. We have successfully demonstrated that future targets can be constructed with metal end windows and are very close to making such targets.

Acknowledgements

First and foremost, I'd like to give my thanks to my advisor, Gordon Cates, for supporting me in the past five years in the group. Not only because I have learned a lot about physics from you, but also for your incredible enthusiasm that kept motivating me to push towards earning my degree. I am honored to have worked with you.

I'd like to thank Peter Dolph and Yuan Zheng, who have taught me the basics of spin-exchange optical pumping and ^3He and alkali polarimetry. Even though the time we spent working together was not long, it laid the very foundation for my work in the following years.

I would like to thank Dr. W. Al Tobias and Dr. Vladimir Nelyubin as well. Al has helped us fill almost every cell we have studied and also taught me the right way to do experiments and the importance of documentation. Vladimir always made sure our experiments could go as smoothly as possible with his laser expertise. We would not have been able to do it without the help from Al and Vladimir.

I also would like to thank all the other graduate students in the group. Maduka Kaluarachchi and Dan Matyas, the two of you made the hours in lab such a joy. I will always miss our talks and of course, the "Young Chicken" we shared at Taste of China. Graduate school was not an easy time for me, I could not have done it without the help from you guys. Sumudu Katugampola and Dave Keder, the two of you are already doing great work, I have no doubt that you will have tremendous amount of success in the future. I look forward to seeing what our lab will be able to achieve because of you.

I'd like to thank the members of my committee: Nilanga Liyanage, Don Crabb, Wilson Miller, for helping me complete the final step towards my degree. I also owe my thanks to my parents and all my friends who have supported me through all these

years. It means a lot to me knowing that no matter what comes next, I will always have your support.

Last but not least, I would like to thank my girlfriend. Shuangshuang, every bit of success I was able to achieve since I met you was at least partly because of your love and support. You gave me something to hold on to so I could pull myself through a tough time. I would not have been able to move on to the next chapter of my life the same way I did without you.

Contents

Abstract	ii
Acknowledgements	iii
List of Tables	ix
List of Figures	xii
1 Introduction	1
1.1 Motivation and Approved JLab Experiments	1
1.2 Overview of Recent Target Development	3
1.3 New Generation Target Cells	5
1.4 Structure of This Thesis	6
2 Spin-Exchange Optical Pumping	8
2.1 Overview	8
2.2 Optical pumping	9
2.2.1 Rb for SEOP	9
2.2.2 Vapor Pressure Curves	10
2.2.3 Energy Levels of Alkali Metal in External Magnetic Field . . .	10
2.2.4 Optical Pumping Process Overview	13

2.2.5	Optical Pumping Rate	14
2.2.6	Polarization Time Evolution	17
2.2.7	Rb Spin Destruction Rate	19
2.3	Spin Exchange	21
2.3.1	Spin-Dependent Interactions	21
2.3.2	Spin Exchange Rate	26
2.4	^3He Spinup and Relaxation	26
2.5	X Factor	28
3	^3He Polarimetry	30
3.1	Overview	30
3.2	Adiabatic Fast Passage	31
3.2.1	Nuclear Magnetic Resonance	31
3.2.2	The Rotating Coordinate System	32
3.2.2.1	Classical Formulation	32
3.2.2.2	Quantum Mechanical Formulation	33
3.2.3	Adiabatic Fast Passage	34
3.2.4	AFP Loss	38
3.3	Electron Paramagnetic Resonance	41
3.3.1	Overview	41
3.3.2	The Breit-Rabi Equation	42
3.3.3	Shift of Zeeman Frequency	43
3.3.4	Experimental Methods	45
3.3.4.1	Overview	45
3.3.4.2	Locating Zeeman Transition Frequency	46
3.3.4.3	EPR Spin Flip Process	47

3.4	Pulsed Nuclear Magnetic Resonance	50
3.4.1	The Rotating Coordinate System	51
3.4.2	Free Induction Decay	51
3.4.3	Experimental Methods	54
4	Development of Hybrid Targets	58
4.1	Overview	58
4.2	Development of Hybrid Targets	59
4.2.1	Experimental Methods	61
4.2.1.1	The ^3He Targets	61
4.2.1.2	Target Cell Polarization Dynamics	63
4.2.1.3	Initial Spinup	67
4.3	The K- ^3He Spin-Exchange Rate Constant	70
4.4	The X Factor	74
5	Development of Cells with Metal End Windows	83
5.1	Overview	83
5.2	Wall Relaxation of ^3He	84
5.2.1	Relaxation on Glass Surfaces	84
5.2.2	Relaxation on Metal Surfaces	88
5.3	Test Cell Fabrication	90
5.3.1	Overview	90
5.3.2	Glass-Metal Seal	91
5.3.3	Mechanical Polishing and Electropolishing	93
5.3.4	Electroplating	94
5.3.5	Final Assembly of the Cell	95
5.4	Cell Fill Procedure	98

5.4.1	Cell Fill Preparation	98
5.4.2	Cell Fill	99
5.5	Experimental Setup and Procedure	100
5.5.1	Pickup Coils	101
5.5.2	Gradient Coils	101
5.5.3	Laser Setup	104
5.5.4	PNMR Losses and Corrected Lifetime	105
5.6	Relaxation Measurement Results and Discussion	111
5.6.1	Gold Coated Spherical Cell	112
5.6.2	Gold Coated Spool Pieces	112
5.6.3	Vertical Cells	114
5.6.4	Horizontal Cells	117
5.6.5	GE180 Cells	119
5.6.6	Titanium Tubes	121
6	Conclusions and Discussion	122
6.1	Overall Design of Next-Generation Polarized ^3He Targets	123
6.2	Incorporating Metal End Windows	125
6.3	Summary	126
Bibliography		127

List of Tables

2.1 Pressure broadening of Rb D ₁ lines by ³ He, ⁴ He and N ₂ . The broadening and shifting density coefficients are listed. The 4th and 6th columns are the temperature dependence for He and N ₂ , respectively. All coefficients are given for 353 K, values for different temperatures can be calculated with the temperature dependence.	15
4.1 The table contains the names, total and pumping chamber volumes, fill densities and target chamber lengths of the 24 target cells. The fill densities are the average of the results from gas system measurements and pressure broadening measurements.	63

4.2	Cell Performance for three sets of experiments: saGDH (top), GEN (middle), and Transversity & d_2^m (bottom). Within each experiment grouping, data is grouped by type of laser used (B = Broadband, N = Narrowband). I_0 is the nominal incident laser intensity at the center of the pumping chamber. T_{pc}^{set} is the oven set temperature. P_{pc}^∞ is the equilibrium polarization in the pumping chamber and Γ_s is the slow time constant extracted from the five parameter fit to the polarization build up curve. Γ_c is the cell-averaged room temperature spin relaxation rate. $\langle P_A \rangle / P_A^l$ is the volume averaged to line averaged alkali polarizaiton ratio determined from the optical pumping simulation. P_A^l is the measured line averaged alkali polarization. D_{fr} & D_{pb} are the K to Rb density ratios determined from Faraday rotation and pressure broadening measurements. $[Rb]_{fr}$ is the Rb number density measured from Faraday rotation. ΔT_{He} is the temperature of Rb inferred from the number density relative to the oven set temperature. ΔT_{He} is the temperature of 3He inferred from temperature tests relative to the oven set temperature. X is the best combined value for the X-factor. * indicates X was measured using only spinup, alkali polarization, and Faraday rotation data. \dagger indicates X was also measured using the early-time behavior of the spinup.	75
4.3	Shown are the values of the X factor at the indicated over set temperatures. The last column is a weighted average of results from either the first two methods or all four methods. A \dagger indicates combined values computed with all 4 methods.	80

5.1 Shown are the fill information, design and maximum measured lifetime of the test cells. Fill type is the method used to clean the gas. † indicates the maximum lifetime was obtained at an elevated position. Although canary glass is not metal, it is listed in the column of metal for Tweety and Sylvester for the sake of keeping the structure of the table simple.	112
---	-----

List of Figures

1.1	A schematic representation of a target cell. The dimensions of different parts of the cell are not to scale.	4
1.2	A diagram of convection style target cell with metal end windows.	6
2.1	Rb And K Number Density Curves	11
2.2	Level Diagram of ^{87}Rb . The splittings are not to scale. Adapted from Dolph's PhD thesis.	12
2.3	The interaction of alkali-metal atoms with left-circularly (σ^+) polarized light. (from Ref. [1])	13
2.4	Absorption cross section for Rb D_1 line in the presence of three different densities of ^3He . (from Ref. [2])	15
2.5	The shift and the broadening due to presence of ^3He for Rb D_1 and D_2 lines. (from Ref. [2])	16
2.6	A. Formation and breakup of alkali-metal/noble-gas van der Waals molecule. B. Binary collision between an alkali-metal atom and a noble-gas atom. (from Ref. [1])	22
2.7	Strengths of various spin-dependent interactions as functions of separation(from Ref. [1])	24

3.1	EPR (left) and AFP (right) setup. Adapted from Dolph's PhD thesis.	34
3.2	Effective field in the rotating frame during an Adiabatic Fast Passage measurement. The ^3He spins follow the direction of the effective field. B_1 is exaggerated to show different components of effective field clearly.	37
3.3	A typical AFP signal. y axis is in arbitrary unit.	38
3.4	Fractional AFP loss (single flip) as a function of field gradient. . . .	40
3.5	A typical FM sweep on a hybrid cell. The central region between the minimum and maximum is fitted to a line. The zero crossing point corresponds to the Zeeman transition frequency.	48
3.6	The same P.I. circuit that was first used by Romalis in our lab. The drawing was then corrected by Peter Dolph.[3]	49
3.7	An EPR measurement for a hybrid cell at 235°C.	49
3.8	PNMR setup.	52
3.9	A PNMR signal taken with gold coated test cell.	56
4.1	Shown are two figures of merit (FOM) for targets built for the indicated experiments. The circles (left axis) indicate the luminosity weighted by the square of polarization. The bars (right axis) represent the total number of spins being polarized per second weighted by the square of polarization. While the right FOM is an indication of the potential of the polarization technique, the left FOM indicates performance achieved during an experiment. The scales have been normalized so that the two FOMs have the same height for the cell marked E142 . .	61
4.2	A target cell. The dimensions of different parts of the cell are not to scale.	62

4.3	(a) Shown is a spinup of the target Brady. The spinup data has been fit with a 3-parameter and a 5-parameter formalism. (b) The residuals of the two fits. The error for 3-parameter fit is larger because it does not account for diffusion between two chambers.	64
4.4	^3He polarization as a function of time for both the pumping chamber and the target chamber. The top curve is the pumping chamber and the bottom curve is the target chamber. Data was taken at a fast pace so there would be enough points to demonstrate the initial behavior.	68
4.5	Plotted is the ratio m_{pc}^F/m_{pc}^s for eight separate measurements. The numbers above the cell names are the oven set temperatures at which the measurements were made. Difference between open and closed points is discussed in the text.	73
4.6	The cell-averaged spin-exchange rate $\langle \gamma_{se} \rangle$ is calculated using data from Faraday rotation and the spin-exchange constants k_{se}^{Rb} and k_{se}^K . The three linear fits shown here are constrained to go through zero. The errors quoted in values of X factor include the uncertainty in our determination of k_{se}^K	78
4.7	Shown are the combined values for X factor (either X_{12} or X_{1234} depending on the availability of data) versus temperature for the cell Sosa, Simone and Antoinette.	81
5.1	Shown on the left is a glass-to-metal-to-glass seal. The metal tube is 5" long by 1" outer diameter. The glass is wetted onto the knife-edge of copper on both ends. Shown on the right is a finished cell with the glass-to-metal-to-glass tube attached.	92
5.2	Glass-to-metal seals survived pressure higher than 20 atm.	93

5.3	Electropolishing [4]	95
5.4	Shown left is the inner surface of a gold coated OFHC copper tube. Shown right is a OFHC copper tube without coating.	96
5.5	Ultrasonic cleaner with 3 tubes being cleaned.	96
5.6	Shown is the design of a typical string for our test cells.	97
5.7	A diagram of a Pyrex string with a cell and a retort attached while connected to the gas system through the bellows. Adapted from Matyas [5].	98
5.8	Diagram of the coils. Adapted from Zheng [6].	102
5.9	Optics for spin-exchange optical pumping. Adapted from Zheng [6]. .	106
5.10	PNMR setup.	107
5.11	A PNMR signal taken with gold coated test cell.	109
5.12	3 spindowns of the cell GoldenVec1 each with a different sampling rate.	110
5.13	A linear fit to extract lifetime corrected for relaxation due to PNMR losses.	110
5.14	A diagram of target cell with metal end windows.	111
5.15	A picture of Gold Maiden, generally referred to as the “spool piece”.	113
5.16	Design and picture of Goldfinger.	114
5.17	The observed degradation of lifetime for Goldfinger (left) and Cupid (right). Shown in each of the two plots were several spindowns at different stage during the tests. The initial amplitude of the spindowns were scaled to 1 for better comparison of lifetime.	115
5.18	A picture of GoldenEye, the only test cell made with a valve.	116
5.19	Four spindowns of Goldrush before elevating the cell. All four measurements display similar lifetime with no obvious sign of degradation.	117

5.20 Shown on the right is the inhomogeneities vs. vertical distance from the center of the field. Shown on the left is the cell Goldrush with relaxation time due to field inhomogeneities as displayed on the right.	118
5.21 Design of the horizontal cell GoldenVec.	118
6.1 Design of next-generation target for upcoming SBS G_E^n experiments.	123

Chapter 1

Introduction

Nuclear-polarized noble gases have been proven to be very useful in various applications, such as polarized targets for electron scattering experiments [7], magnetic resonance imaging [8] and neutron scattering experiments [9]. Polarized ${}^3\text{He}$ has been particularly useful for studying spin-dependent interactions involving neutrons because, to first-order approximation, a ${}^3\text{He}$ nucleus has a pair of protons with paired spins and a single neutron that carries most of the nuclear spin. Free neutrons are not used as targets because they decay with a lifetime of about 14 minutes, 42 seconds.

1.1 Motivation and Approved JLab Experiments

The neutron electromagnetic form factors, G_E^n and G_M^n play essential roles for understanding nucleon structure. At non-relativistic energies, they are the Fourier transforms of the electric charge and magnetic moment distributions. Even at relativistic energies, the elastic form factors provide unique information on the transverse structure of the nucleon [10, 11]. Double-polarization experiments on the proton showed that the ratio of the proton's electric and magnetic elastic form factors, G_E^p/G_M^p , de-

clines nearly linearly as the four momentum transfer squared, Q^2 , increases, in sharp contrast to expectations [12]. These measurements caused a resurgence of interest in nucleon structure, and shed light on the importance of quark orbital angular momentum. More recent double-polarization experiments measured the neutron electric form factor G_E^n up to a Q^2 of 3.4 GeV^2 (E02-013) [13], and showed behavior that was generally consistent with models that described well the earlier proton results. The neutron results, when combined with the proton results, also made it possible to extract the form factors for the individual up- and down-quark flavors [14]. Significantly different Q^2 dependence was seen for the up- and down-quarks, a difference that some theorists have interpreted as evidence for the importance of diquark correlations.

The multiple surprises that have emerged from the study of nucleon elastic form factors at Jefferson Laboratory (JLab) have underscored the value of performing such studies at high values of Q^2 . For the neutron, predictions for the behavior of the ratio of the electric and magnetic elastic form factors, G_E^n/G_M^n , vary significantly from one model or calculation to another. A particularly compelling example, based on the Dyson-Schwinger Equation (DSE) formalism, predicts a dramatic turnover and zero crossing in the vicinity of $Q^2 = 10 \text{ GeV}^2$ [15]. The verification of this prediction would have profound impact on our understanding of nucleon structure. An important part of the future program at JLab to explore the high- Q^2 behavior of the elastic nucleon form factors is the Super Bigbite Spectrometer (SBS) program. The SBS experiment to measure G_E^n/G_M^n up to $Q^2 = 10 \text{ GeV}^2$, E12-09-016, is a major motivating factor for the work described in this thesis. The count rate associated with the elastic form factors drops off very quickly with increasing Q^2 . This in turn puts pressure on all aspects of the experiment to achieve adequate statistics, including running the polarized ${}^3\text{He}$ target at high luminosity.

Another important issue in understanding nucleon structure is the spin structure

associated with the quarks. Polarized deep inelastic scattering provides a window into the spin carried by the quarks, and a particularly useful observable is the spin asymmetry A_1^n , that describes the spin dependence of the virtual photo absorption cross section. It is particularly useful to measure A_1^n at high values of Bjorken x , where several predictions exist. Both constituent quark models and perturbative QCD predict that $A_1^n \rightarrow 1$ as $x_{\text{Bj}} \rightarrow 1$, but it is also the case that count rates drop quickly toward high values of x_{Bj} . Two experiments are currently approved at JLab that will measure A_1^n up values of x_{Bj} in excess of 0.7; they are E12-06-122 in Hall A, and E12-06-110 in Hall C. Both of these experiments will require a polarized ${}^3\text{He}$ target capable of running at high luminosity and thus depend critically on the work described here.

1.2 Overview of Recent Target Development

An early use of polarized ${}^3\text{He}$ targets in electron scattering experiments was at the Stanford Linear Accelerator Center (SLAC) in the year of 1992. The experiment was known as E142 and investigated the spin structure of neutrons [7]. Recent experiments were conducted at Jefferson Laboratory (JLAB) in Newport News, Virginia, such as the aforementioned E02-013, also known as “Measurement of the Neutron Electric Form Factor G_E^n at High Q^2 ”. Other experiments involved the investigation of single-spin asymmetries in semi-inclusive deep inelastic scattering [16].

The ${}^3\text{He}$ targets used in these experiments were polarized with the technique of Spin-Exchange Optical Pumping (SEOP). Fig. 4.2 shows schematically a typical target, also referred to as a “target cell”. These cells were made of GE180 glass and used a two-chambered design. The top chamber, known as the pumping chamber, is where ${}^3\text{He}$ is polarized through SEOP. The bottom chamber, known as the target

chamber, is where electron scattering occurs. The two ends of the target chamber where electron beam enters and exits are known as the “end windows”. Great effort has been made in our lab to develop this generation of cells. Alkali-hybrid SEOP together with narrowband laser-diode arrays have increased the ${}^3\text{He}$ polarization from 37% to 70%. Among other things, we also carefully studied an additional spin relaxation mechanism that limits the maximum achievable ${}^3\text{He}$ polarization, which can be characterized by something referred to as the “X Factor” [17]. Analysis of data accumulated through developing this generation of target cells were thoroughly discussed in Ref. [18], part of which will be presented in chapter 4.

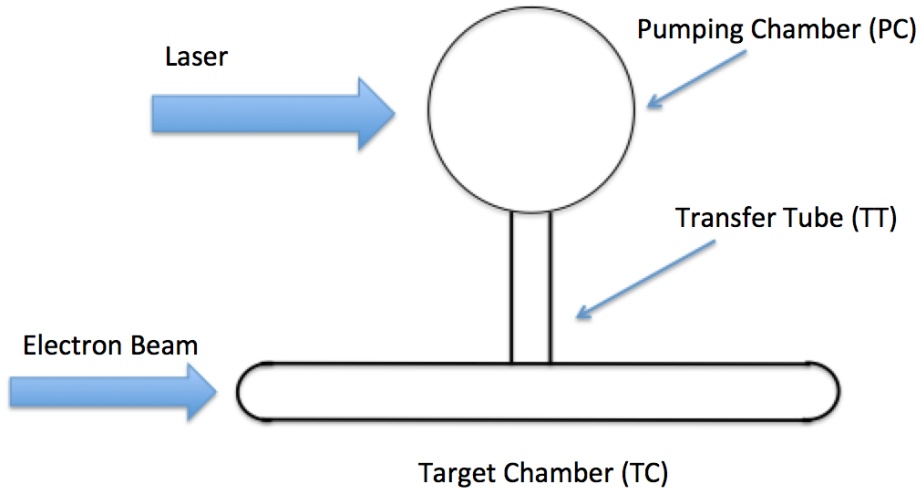


Figure 1.1: A schematic representation of a target cell. The dimensions of different parts of the cell are not to scale.

1.3 New Generation Target Cells

The future experiments planned for the JLab 12GeV era after the energy upgrade will be much more demanding in terms of target cell performance. In particular, there is a desire to run experiments with higher luminosity, where luminosity is the product of gas density in the target, interaction length and beam current. Increased luminosity will lead to more interactions that depolarize the target. We have designed and tested a new style cell that utilizes convection instead of diffusion to increase the rate at which the polarization in the target chamber is replenished by polarized gas from pumping chamber [19]. We have obtained over 50% polarization with controllable convection speed so far.

An additional problem that comes with higher beam current is that the glass end windows of traditional design are not likely to survive the experiments. Our group started exploring the option of using metal end windows eight years ago. Fig 5.14 shows an example configuration of such a target. The first problem to solve is to find out the correct material and the proper technique to incorporate metal without introducing significant spin relaxation while still being able to hold high pressure gas (12 atm) inside. This is a brand new technique that may have a profound impact on future cell designs once fully developed. Although no metal end windows have been tested so far, through carefully examining multiple glass cells with different kinds metal tubes (much larger in area compared to the end windows that will be used in JLAB experiments) attached, we have developed a reliable way of incorporating metal into target cells without introducing excessive spin relaxation. We believe the next generation target cells used in the 12GeV era will be able to utilize metal end windows. In our test cells, the metals tubes were connected to Pyrex glass with Houskeeper seals [20] and stayed intact through high pressure tests. After exploring



Figure 1.2: A diagram of convection style target cell with metal end windows.

options such as pure copper, gold coated copper, titanium, stainless steel, gold coated titanium, we have established that electroplating gold on a copper substrate yields the best result so far. We have achieved a 15.6 h relaxation time with a Pyrex cell that had a 5" long by 1" diameter gold coated copper tube attached horizontally. The additional relaxation rate introduced by the metal surface is proportional to the area of the gold surface. By comparing relaxation rates of test glass-and-metal cells with pure-glass control cells, the relaxation rate due to the gold surface was extracted. With this result, we believe the relaxation rate introduced by small metal windows in a target will be less than $1/93.06 \text{ hr}^{-1}$. To the best of our knowledge, our group was the first to have proved the potential of incorporating metal into target cells in the presence of alkali vapor.

1.4 Structure of This Thesis

This thesis focuses on both a discussion of the development of high-performance polarized ${}^3\text{He}$ targets that utilize spin-exchange optical pumping (SEOP) and the

development of future target cells that incorporate metal end windows. Chapter 2 gives a general description of SEOP. Chapter 3 introduces polarimetry techniques used in our lab for target cell characterization. Chapter 4 discusses the results collected in our lab from over a decade of development of ${}^3\text{He}$ target cells, in which the spin-exchange rate constant for K and ${}^3\text{He}$ is calculated and the so-called “X Factor” is studied. Chapter 5 presents the development process of target cells with metal parts that aims to incorporate metal end windows into future cells for the JLab 12 GeV era experiments. Chapter 6 presents some conclusions and discusses the implications for future work.

Chapter 2

Spin-Exchange Optical Pumping

2.1 Overview

Spin-polarized noble gases have been widely used for various purposes [7, 16, 21, 22]. In JLAB (Thomas Jefferson National Accelerator Facility), polarized ^3He is used as target for electron-scattering experiments. This is because a ^3He nucleus has a pair of protons with paired spins and a single neutron that contributes the most of the nuclear spin. In MRI, polarized ^3He has seen uses such as detecting structural damage in the lungs.

There are generally two ways of polarizing ^3He : Metastability-Exchange Optical Pumping (MEOP) [23] and Spin-Exchange Optical Pumping (SEOP) [24–26]. Our group focuses on SEOP as MEOP polarizes gas at relatively low pressure (~ 1 torr), thus further compression is required to produce target cells of several atms that meet the need of JLab experiments.

In SEOP, alkali metal is polarized by circularly polarized laser light tuned to the D1 transition of the particular alkali species used. ^3He obtains polarization from alkali metal through spin-exchange process [27]. With the combination of hybrid

alkali mixtures (typically Rb and K) and spectrally narrowed lasers [28, 29], more than 80% polarizations have been produced.

2.2 Optical pumping

2.2.1 Rb for SEOP

In optical pumping, Rb is often the alkali metal chosen to be optically pumped by circularly polarized laser light. The angular momentum of polarized photons are transferred to the valence electrons of Rb atoms [1]. Sometimes hybrid mixtures of Rb and K are used together, in which case Rb is still the alkali metal that is directly pumped by laser light while K serves as an efficient medium to transfer the polarization from Rb to ${}^3\text{He}$. Because the spin destruction rates are much lower for lighter alkali metals, K- ${}^3\text{He}$ spin-exchange process is a lot more efficient than that of Rb- ${}^3\text{He}$. Rb is still selected as the alkali metal to be pumped directly because of the relative ease of acquiring laser at the Rb D₁ line wavelength and the wide separation its between D₁ (794.7nm) and D₂ line (780nm).

The Rb melting point is at 39.5°C, so it's easy to achieve enough Rb vapor without having to drive the oven temperature too high. In our lab, depending on if the cell contains pure Rb or Rb/K mixture, the oven temperature can be between 85°C to as high as 255°C. Perhaps the most used oven temperature for hybrid cells is 235°C which has empirically been a good temperature to produce Rb/K mixture vapor, while around 170°C is typically enough for pure Rb.

2.2.2 Vapor Pressure Curves

When the alkali metal is heated to above its melting point, a small amount of alkali metal atoms evaporate. The equilibrium vapor pressure is temperature dependent:

$$P = 10^{5.006+\alpha+\beta/T} \text{ Pa} \quad (2.1)$$

where α and β are listed in Table 2.2.2 [30].

	Potassium	Rubidium
α	4.402	4.312
β	-4453	-4040

Thus the number density is

$$[A] = \frac{10^{5.006+\alpha+\beta/T}}{k_B T} \quad (2.2)$$

The number density curves of pure Rb and K vapor are shown in Fig. 2.1.

2.2.3 Energy Levels of Alkali Metal in External Magnetic Field

The Hamiltonian for ground state ($L=0$) alkali metal atoms in external magnetic field is:

$$\mathbf{H} = A\mathbf{I} \cdot \mathbf{S} - g_e \mu_B S_z B_z - g_N \mu_N I_z B_z \quad (2.3)$$

The first term $A\mathbf{I} \cdot \mathbf{S}$ describes the coupling of the nuclear spin \mathbf{I} with the electron spin \mathbf{S} and is key to spin exchange, where A is the isotropic magnetic-dipole coupling coefficient [31]. The resulting energy levels from the first term are referred to as

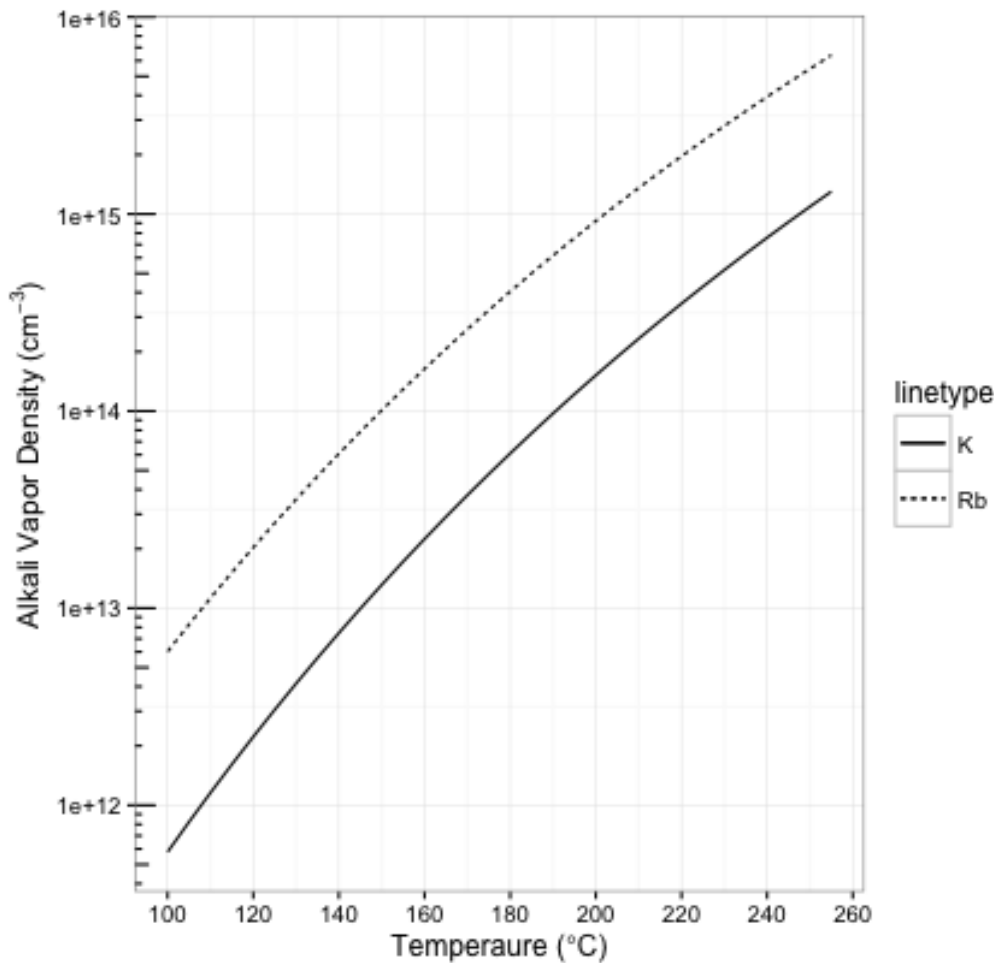


Figure 2.1: Rb And K Number Density Curves

hyperfine structure. The second and third terms describe the Zeeman splitting due to the presence of an external magnetic field. $\mu_B = 9.274 \times 10^{-24} \text{ J/T}$ and $\mu_N = 5.051 \times 10^{-27} \text{ J/T}$ are the Bohr and nuclear magnetons. $g_e \approx 2$ and $g_N \approx 5.59$ are the electronic and nuclear Lande g-factors.

The linear relationship between energy levels and magnetic field only holds for weak magnetic fields which applies to our lab where ~ 13 Gauss is used most of the time. When the Zeeman splitting grows comparable to the hyperfine energy difference one would have to take into account the quantum mixing of the states, the result is described by Breit-Rabi Formula. With ~ 13 Gauss, the hyperfine term dominates

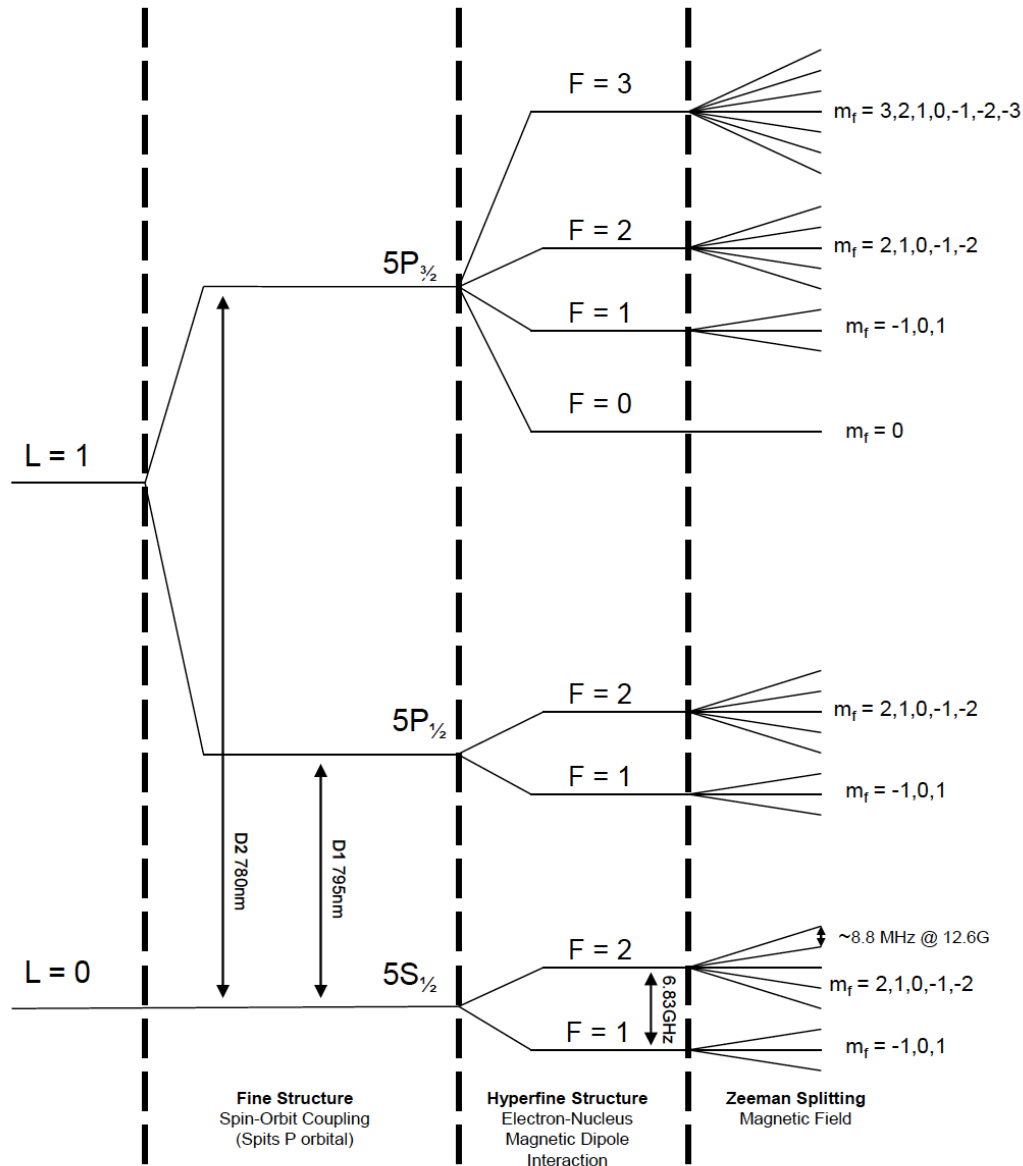


Figure 2.2: Level Diagram of ^{87}Rb . The splittings are not to scale. Adapted from Dolph's PhD thesis.

the total Hamiltonian. ^{85}Rb and ^{87}Rb are both present in the alkali metal used for SEOP, the energy levels of ^{87}Rb are shown in Fig. 2.2.

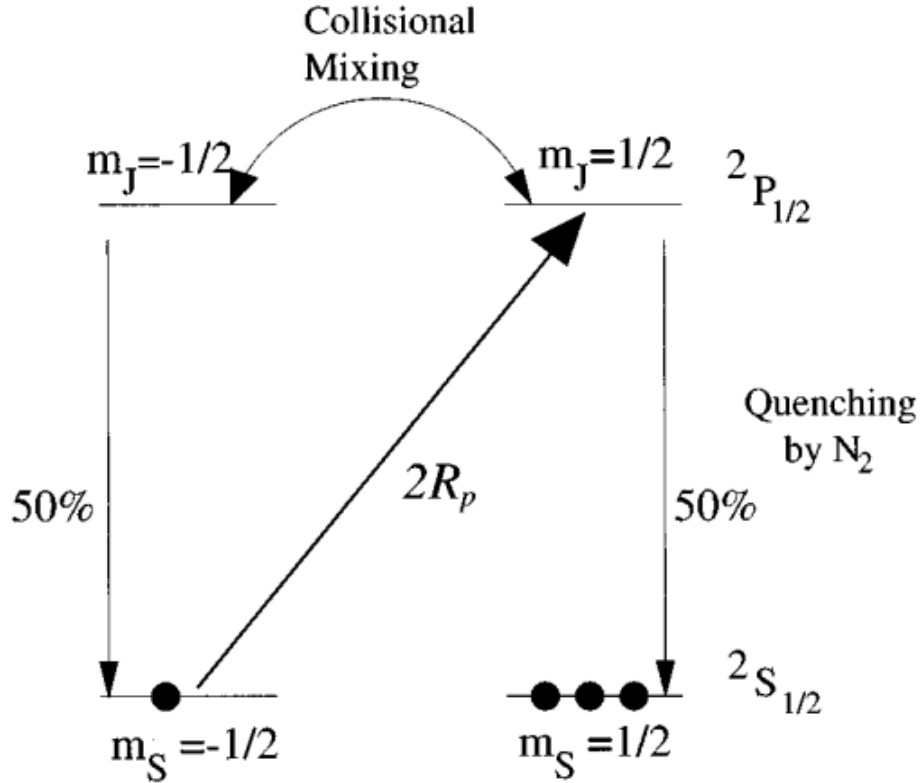


Figure 2.3: The interaction of alkali-metal atoms with left-circularly (σ^+) polarized light. (from Ref. [1])

2.2.4 Optical Pumping Process Overview

For simplicity, the following discussion will ignore the nuclear spins for now. The inclusion of nuclear spins will increase the number of energy states but the optical pumping mechanism remains the same. In our typical setup, circularly polarized laser light is tuned to the D1 line of Rb and excites valence electrons of Rb from $5S_{1/2}$ state to $5P_{1/2}$ state as shown in Fig. 2.3[1].

Left-circularly polarized light is assumed in the figure. Conservation of angular momentum requires $\Delta m = +1$ as the figure shows. Through collisions with other Rb atoms, excited electrons will mix and evenly distribute between the two $2P_{1/2}$

states. Electrons then decay to the two ground states with equal probabilities. The selection rule for the decay process is $\Delta m = 0$ or ± 1 . Even though both ground states receive electrons from the decay, only the $m = -1/2$ state absorbs the circular polarized photons and is being depleted, so atoms are in effect pumped to the $m = +1/2$ state. When we consider Rb with nuclear spins, both $5S_{1/2}$ and $5P_{1/2}$ states are split into more energy levels, but the net effect is still that the ground state with highest m accumulate atoms over time.

When the excited electrons decay back to the ground state, they emit unpolarized photons with angular momentum in random directions which can depolarize the gas. A small amount of N_2 gas is added into the cell (typically around 0.1 Amagats) to non-radiatively quench the excited electrons as N_2 molecules can absorb the released energy of spontaneous decays into their rotational and vibrational modes of oscillation. With an appropriate amount of N_2 [32], the photon-emitting decays can be reduced to less than 3%.

2.2.5 Optical Pumping Rate

The optical pumping rate at position \vec{r} can be described by

$$R = \int \Phi(\nu, \vec{r}) \sigma(\nu) d\nu \quad (2.4)$$

where $\Phi(\nu, \vec{r})$ is the position dependent photon spectral flux density and $\sigma(\nu)$ is the photon absorption cross section. The cross section has a natural Lorentzian lineshape which is broadened by the Doppler effect and pressure broadening. The pressure broadening effect dominates the lineshape as our cells normally have densities well above one amagat. The collisions of Rb with ^3He and N_2 cause the broadening as well as a slight frequency shift of the D_1 line. The coefficients of pressure broadening for

Table 2.1: Pressure broadening of Rb D₁ lines by ³He, ⁴He and N₂. The broadening and shifting density coefficients are listed. The 4th and 6th columns are the temperature dependence for He and N₂, respectively. All coefficients are given for 353 K, values for different temperatures can be calculated with the temperature dependence.

	⁴ He	³ He	Temp. depen.	N ₂	Temp. depen.
D ₁ full width (GHz/amg)	18.0±0.2	18.7±0.3	T ^{0.05±0.05}	17.8±0.3	T ^{0.3}
D ₁ line shift (GHz/amg)	4.3±0.1	5.64±0.15	T ^{1.1±0.1}	-8.25±0.15	T ^{0.3}

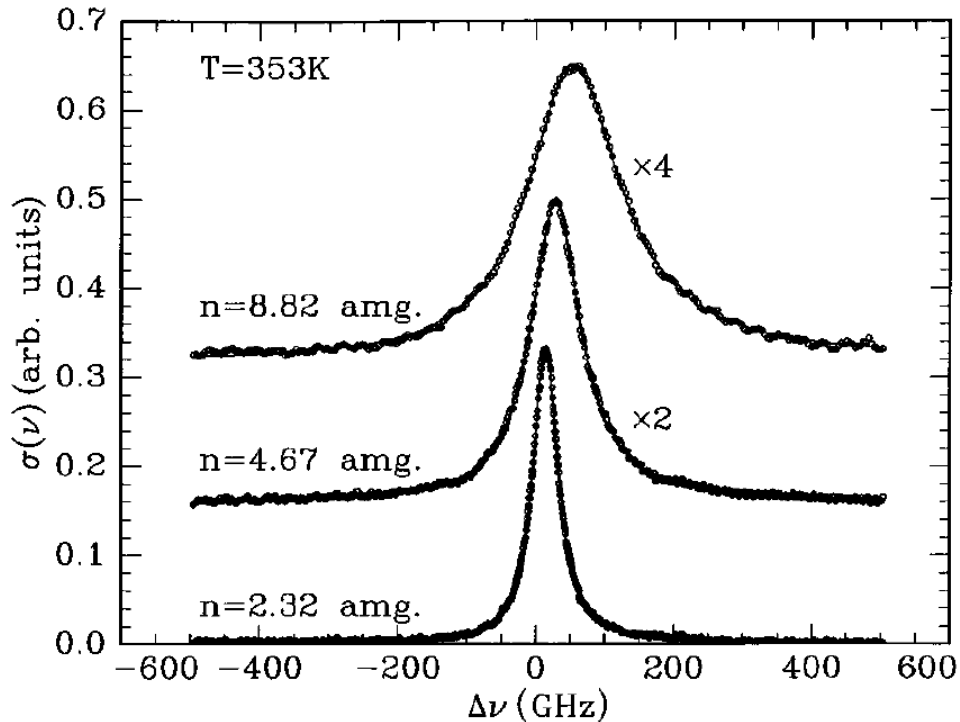


Figure 2.4: Absorption cross section for Rb D₁ line in the presence of three different densities of ³He. (from Ref. [2])

³He, ⁴He and N₂ are listed in Table 2.1, and can be used to calculate the broadened line width and the shifted line center.

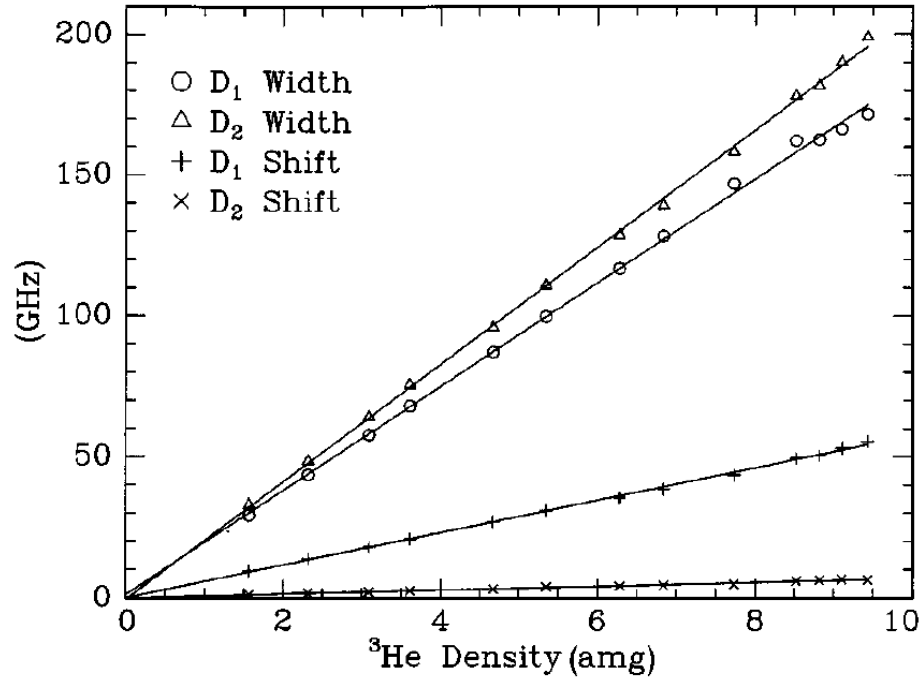


Figure 2.5: The shift and the broadening due to presence of ${}^3\text{He}$ for Rb D_1 and D_2 lines. (from Ref. [2])

$\sigma(\nu)$ follows the sum rule[33]:

$$\int \sigma(\nu) d\nu = \pi r_0 c f \quad (2.5)$$

where $r_0 = 2.82 \times 10^{-13}$ cm is the classical electron radius and $f = 0.337$ [25] is the transition oscillator strength. Since our lineshape is dominated by pressure broadening, the photon absorption cross section is well approximated by a Lorentzian lineshape:

$$\sigma(\nu) = f r_e c \frac{\frac{\Gamma_A}{2}}{(\nu - \nu_0)^2 + (\frac{\Gamma_A}{2})^2} \quad (2.6)$$

where Γ_A is the pressure dependent FWHM, $\Gamma_A \approx 0.04\text{nm}/\text{amg} \cdot [{}^3\text{He}]$. At the front of the cell, the photon spectral flux density is reasonably described as the product of

a Gaussian spatial distribution and a Gaussian spectrum.

$$\phi(\nu, \vec{r}) = \phi_0(\vec{r})G(\nu) \quad (2.7)$$

with

$$\phi_0(\vec{r}) = \frac{P}{h\nu} \frac{2}{\omega^2 \pi} e^{2r^2/\omega^2} \quad (2.8a)$$

$$G(\nu) = \frac{1}{\sqrt{2\pi}\sigma_l} e^{-(\nu-\nu_l)^2/2\sigma_l^2} \quad (2.8b)$$

where P is the laser power; ω is the beam waist; σ_l is the Gaussian width of the laser and ν_l is the central laser frequency.

2.2.6 Polarization Time Evolution

${}^3\text{He}$ nuclei have an intrinsic nuclear spin of $1/2$, thus it is relatively simple to explain the math of polarization accumulation with ${}^3\text{He}$ as the example. One typically defines the polarization as the asymmetry between $+1/2$ state and $-1/2$ state:

$$P = \frac{\rho_{+1/2} - \rho_{-1/2}}{\rho_{+1/2} + \rho_{-1/2}} = \rho_{+1/2} - \rho_{-1/2} \quad (2.9)$$

where $\rho_{\pm 1/2}$ is the ensemble population in the $\pm 1/2$ state.

While it might not be true for Rb, we are only treating the time evolution of polarization of Rb electrons the same as ${}^3\text{He}$ for our purpose with the following the equation:

$$\frac{dP}{dt} = \gamma(1 - P) - \Gamma \cdot P \quad (2.10)$$

where γ is the polarization rate and Γ is the depolarization rate due to all other

processes. The solution of this differential equation has the simple form of:

$$P(t) = Ce^{-(\gamma+\Gamma)t} + \frac{\gamma}{\gamma+\Gamma} \quad (2.11)$$

The saturated polarization is defined as the value of P in the limit $t \rightarrow \infty$:

$$P_\infty = \frac{\gamma}{\gamma+\Gamma} \quad (2.12)$$

The initial polarization is defined as the value of P at $t = 0$:

$$P_0 = C + \frac{\gamma}{\gamma+\Gamma} = C + P_\infty \quad (2.13)$$

Thus, $P(t)$ can be expressed as:

$$P(t) = (P_0 - P_\infty)e^{-(\gamma+\Gamma)t} + P_\infty \quad (2.14)$$

In the case of polarizing Rb with a pump laser, γ is the pumping rate R and Γ is the Rb spin relaxation rate Γ_{Rb} . There is typically a small angle θ between the pump laser and the holding field even though great effort has been made to minimize the angle. Thus $P(t)$ can be rewritten as:

$$P(t) = P_0 e^{-(R+\Gamma_{Rb})t} + P_{laser} \cos \theta \frac{R}{R + \Gamma_{Rb}} (1 - e^{-(R+\Gamma_{Rb})t}) \quad (2.15)$$

where θ is called the skew angle, P_{laser} is the circular polarization of the pump laser which is normally above 99.5%. Rb close to the front side of the cell can reach above 97% (depends on the laser power and other factors) on the order of 100's of microseconds. As the laser propagates through the cell, power is attenuated by Rb vapor. Therefore Rb polarization at the back side of the cell is typically lower than

that at the front side. One way to minimize this problem is to shine pump laser light from both sides of the cell to achieve higher overall Rb polarization and ^3He polarization.

Spins are thermally polarized in the presence of a magnetic field even without being actively polarized. The probability for a spin to be in state s is:

$$\text{Prob.} = \frac{e^{-E_s/k_B T}}{\sum_{si} e^{-E_{si}/k_B T}} \quad (2.16)$$

where E_s is the energy of the state, k_B is the Boltzmann constant and T is the temperature. Using the thermal distribution, under typical operating conditions, ^3He polarization is 10^{-9} and Rb polarization is 10^{-5} . Both are negligible without active pumping.

2.2.7 Rb Spin Destruction Rate

There are two main mechanisms of Rb depolarization: the binary collisions with Rb, ^3He and N_2 , and the formation and breakup of van der Waals molecules, the second mechanism is negligible for ^3He cells [1]. The Rb spin destruction rate can then be expressed as

$$\Gamma_{\text{Rb}} = k_{\text{Rb-Rb}}[\text{Rb}] + k_{\text{Rb-}^3\text{He}}[^3\text{He}] + k_{\text{Rb-}N_2}[N_2] \quad (2.17)$$

where k_{Rb-X} is the spin destruction rate constant and [X] is the density of X. The constants are listed as follows [34, 35]:

$$k_{Rb-^3He}(T) = 55.9(9) \left(\frac{T}{473.15K} \right)^{3.31(12)} \text{Hz/amg} \quad (2.18a)$$

$$k_{Rb-N_2}(T) = 290(30) \left(\frac{T}{473.15K} \right)^{2.0(25)} \text{Hz/amg} \quad (2.18b)$$

$$k_{Rb-Rb} = 4.813(48) \times 10^{-13} \text{Hz} \cdot \text{cm}^3 \quad (2.18c)$$

For a pure Rb cell at 170°C with the following densities in the pumping chamber:

$$[^3He] \approx 8.0 \text{amg} \quad (2.19a)$$

$$[N_2] \approx 0.08 \text{amg} \quad (2.19b)$$

$$[Rb] \approx 6.0 \times 10^{14} \text{cm}^{-3} \quad (2.19c)$$

The approximate spin destruction rates due to various gases are:

$$\Gamma_{Rb-^3He} \approx 360 \text{Hz} \quad (2.20a)$$

$$\Gamma_{Rb-N_2} \approx 20 \text{Hz} \quad (2.20b)$$

$$\Gamma_{Rb-Rb} \approx 289 \text{Hz} \quad (2.20c)$$

The total spin destruction rate is 669 Hz. By contrast, the average optical pumping rate at the front of the cell with 20 W and 1.5 cm beam radius narrowband laser light is often of 100s kHz.

2.3 Spin Exchange

Following equation 2.15, the time evolution of ${}^3\text{He}$ polarization can be expressed as:

$$P_{{}^3\text{He}}(t) = P_0 e^{-(\gamma_{se} + \Gamma)t} + P_{\text{Rb}} \frac{\gamma_{se}}{\gamma_{se} + \Gamma} (1 - e^{-(\gamma_{se} + \Gamma)t}) \quad (2.21)$$

The saturation polarization is

$$P_\infty = P_{\text{Rb}} \frac{\gamma_{se}}{\gamma_{se} + \Gamma} \quad (2.22)$$

where γ_{se} is the spin exchange rate between ${}^3\text{He}$ and Rb, and Γ is the spin relaxation rate.

2.3.1 Spin-Dependent Interactions

The key process in spin-exchange optical pumping is collisional transfer of polarization between optically pumped alkali-metal atoms and the nuclei of the noble gas atoms. As in Fig. 2.6, the transfer of angular momentum occurs either while the atoms are bound in van der Waals molecules or in simple binary collisions. The first mechanism is only important for heavy noble gas nuclei such as X3, while binary collisions is the dominating mechanism for ${}^3\text{He}$. The time scale for binary collisions is on the order of 10^{-12} sec, the collision can induce both $\Delta F = \pm 1$ and $\Delta F = 0$ transitions between hyperfine sublevels. For heavier noble gases like ${}^{129}\text{Xe}$ at pressure of a few tens of Torr, the contributions of van der Waals molecules can greatly exceed that of binary collisions. At several atm which is the typical operating pressure for SEOP, the time scale of van der Waals molecules is greatly limited by collision so that the binary collisions dominate [1].

Spin-dependent interactions produce the spin transfer and relaxation. For SEOP,

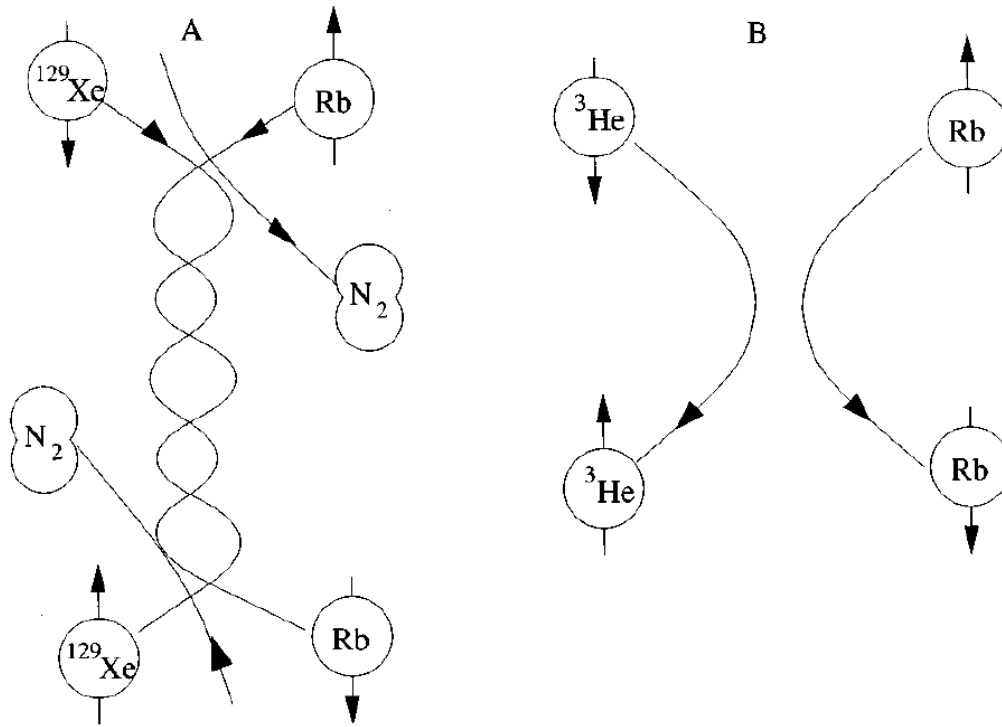


Figure 2.6: A. Formation and breakup of alkali-metal/noble-gas van der Waals molecule. B. Binary collision between an alkali-metal atom and a noble-gas atom. (from Ref. [1])

spin-rotation interaction between \vec{S} and the rotational angular momentum \vec{N} of the atom pair formed by Rb and noble gas atom, and the isotropic hyperfine interaction between \vec{S} and the noble-gas nuclear spin \vec{I}_b dominate the spin-exchange process:

$$V_1(\vec{R}) = \gamma(R)\vec{N} \cdot \vec{S} + A(R)\vec{I}_b \cdot \vec{S} \quad (2.23)$$

The spin-rotation interaction is caused by the magnetic fields from relative motion of the charges of the colliding atoms, and the isotropic hyperfine interaction originates from the Fermi-contact magnetic fields produced by two nuclei. The spin-rotation interaction produces relaxation of the alkali-metal electron-spins, while the isotropic

hyperfine interaction transfers angular momentum back and forth between the alkali-metal electron spins and the noble-gas nuclear spins.

An alkali-metal atom and a noble-gas atom interact via both a large spin-independent interaction $V_0(R)$ and a small spin-dependent interaction $V_1(R)$. At the high operating temperatures, V_0 determines classical collision trajectories, while V_1 acts as a small perturbation. We'll focus on V_1 below since it is responsible for spin exchange.

Including a few more terms that were neglected in Eq. 2.23, the spin-dependent interaction $V_1(R)$ can be expressed as [1]:

$$\begin{aligned} V_1(\vec{R}) = & \gamma(R) \vec{N} \cdot \vec{S} + \sum_k A_k(R) \vec{I}_k \cdot \vec{S} \\ & + \sum_k B_k(R) \vec{I}_k \cdot (3\vec{R}\vec{R} - 1) \cdot \vec{S} \\ & + \sum_k C_k(R) \vec{I}_k \cdot (3\vec{R}\vec{R} - 1) \cdot \vec{I}_k \end{aligned} \quad (2.24)$$

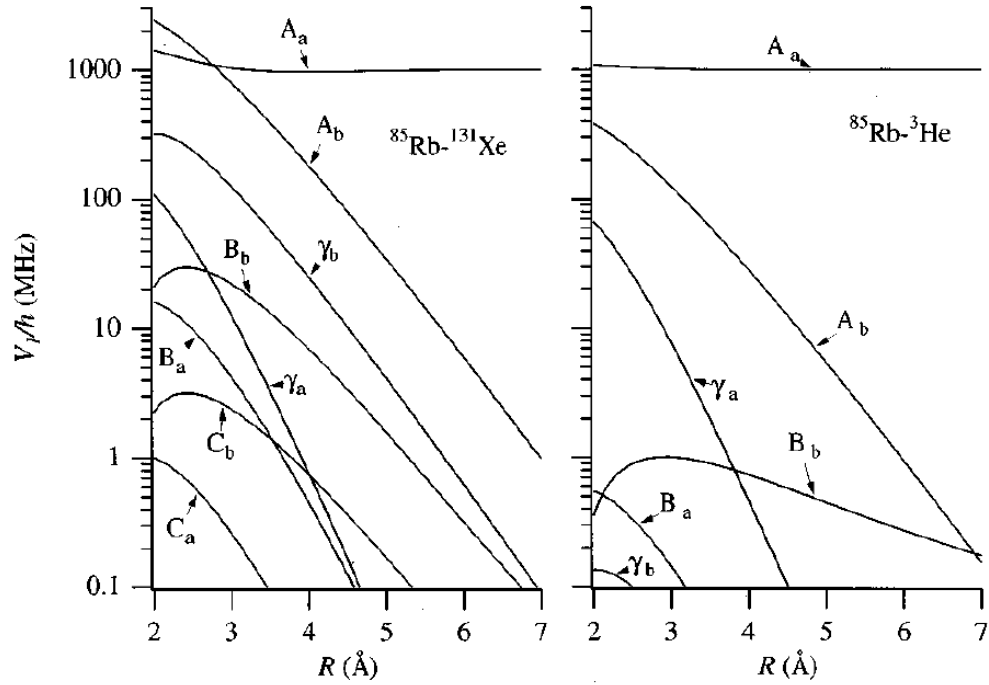


Figure 2.7: Strengths of various spin-dependent interactions as functions of separation (from Ref. [1])

where \vec{I}_a and \vec{I}_b are the nuclear spins of the atomic pair, where a stands for alkali metal atom and b stands for noble gas atom. γ is the coefficient of the spin-rotation interaction, while A_k , B_k , C_k are the coefficients for isotropic magnetic-dipole hyperfine interactions, anisotropic magnetic-dipole hyperfine interactions, and electric quadrupole interactions, respectively. A_a greatly exceed other coefficients as the separations between atoms increase.

The isotropic hyperfine interactions come from the Fermi-contact magnetic fields of the two nuclei. A_b is the term responsible for spin exchange:

$$A_b(R) = \frac{8\pi g_s \mu_B \mu_b}{3I_b} |\eta \phi_0(R)|^2 \quad (2.25)$$

where η is the enhancement factor which equals to the ratio of the perturbed wave

function at the noble gas nucleus to that without the noble gas atom. The isotropic hyperfine interaction also introduces a frequency shift of the magnetic resonance lines for alkali-metal and noble gas atoms. The frequency shift is characterized by another enhancement factor κ which is the ratio of the actual shift of the alkali metal electron lines due to the presence of polarized noble gas nuclei to what would be produced by the bulk magnetization of polarized noble gas. The shift is used in the technique Electron Paramagnetic Resonance (EPR) to calculate the polarization of noble gas nuclei.

The full dipole field of the noble-gas nucleus at a displacement \mathbf{r}_b from the nucleus is [36]

$$\mathbf{H}_b(\mathbf{r}_b) = \frac{8\pi\mu_b}{3I_b} \mathbf{I}_b \delta(\mathbf{r}_b) + \frac{\mu_b}{I_b} \mathbf{I}_b \cdot \frac{3\mathbf{r}_b \mathbf{r}_b - 3r_b^2 \mathbf{1}}{r_b^5} \quad (2.26)$$

where \mathbf{I}_b is the spin of noble gas nucleus. The first term of Eq. 2.26 is the origin of the spin-conserving isotropic magnetic-dipole hyperfine interaction, while the second term is where the anisotropic interaction comes from. The well-understood isotropic magnetic-dipole hyperfine interaction aligns the noble gas spins parallel to the electron spin polarization, bu the anisotropic magnetic-dipole hyperfine interaction polarizes nuclear spins antiparallel to electron spins. Even though the anisotropic magnetic-dipole coupling is relatively weak compared with the isotropic interaction, thus large nuclear polarization can be obtained. For nearly all alkali-metal-noble-gas pairs in which helium is not the noble gas, the ratio of the exchange rate due to anisotropic interaction to the rate due to isotropic interaction is less than 2.5% [36]. However, this ratio is somewhat larger for alkali-metal-helium pairs.

2.3.2 Spin Exchange Rate

The spin exchange rate due to binary collisions is:

$$\gamma_{se} = \langle \sigma_{se} v \rangle [Rb] = k_{se} [Rb] \quad (2.27)$$

where $k_{se} = \langle \sigma_{se} v \rangle$ is the velocity-averaged spin exchange rate constant. k_{se} for spin exchange between ^3He and Rb is [37]:

$$k_{se}^{^3\text{He}-\text{Rb}} = (6.7 \pm 0.7) \times 10^{-20} \text{ cm}^3/\text{s} \quad (2.28)$$

At 170°C which is a typical temperature that we run tests with,

$$[Rb] = 2.60 \times 10^{14} \text{ cm}^{-3} \quad (2.29)$$

Thus for a simple spherical cell with pure Rb,

$$\frac{1}{\gamma_{se}} \approx 15.9 \text{ hrs} \quad (2.30)$$

2.4 ^3He Spinup and Relaxation

Similar to the optical pumping process of Rb, ^3He polarization can be described by

$$P_{^3\text{He}}(t) = P_0^{^3\text{He}} e^{-(\gamma_{se} + \Gamma)t} + P_\infty^{^3\text{He}} (1 - e^{-(\gamma_{se} + \Gamma)t}) \quad (2.31)$$

where the saturation polarization is

$$P_\infty^{^3\text{He}} = P_\infty^{\text{Rb}} \frac{\gamma_{se}}{\gamma_{se} + \Gamma} \quad (2.32)$$

And Γ is the total relaxation rate of ${}^3\text{He}$ nucleus spin polarization due to all processes except for spin exchange,

$$\Gamma = \Gamma_{dipolar} + \Gamma_{inhomogeneity} + \Gamma_{wall} \quad (2.33)$$

When a target cell are used in electron scattering experiments where an electron beam goes through part of the cell, an additional relaxation rate due to the beam Γ_{beam} should also be included.

The coupling of nuclear spin to orbital angular momentum creates an intrinsic ${}^3\text{He}$ relaxation rate that depends on density. At room temperature (23°C), the dipolar relaxation rate is [26]

$$\Gamma_{dipolar} = \frac{[{}^3\text{He}]}{744} \text{ hr}^{-1} \quad (2.34)$$

where $[{}^3\text{He}]$ is the ${}^3\text{He}$ density in amagats. Assuming the cell density is 8 amg, the relaxation rate is $1/93 \text{ hr}^{-1}$. In addition, there is an additional intrinsic relaxation due to the spin-rotation interaction. This mechanism dominates the relaxation for ${}^{129}\text{Xe}$ but is small for ${}^3\text{He}$.

The relaxation rate due to field inhomogeneities is [38–40]

$$\Gamma_{inhomogeneity} = D \frac{|\nabla B_x|^2 + |\nabla B_y|^2}{B_0^2} \quad (2.35)$$

where D is the ${}^3\text{He}$ diffusion constant, ∇B_x and ∇B_y are the transverse magnetic field inhomogeneities, B_0 is the holding field along z-axis. Under operating conditions, assuming the pressure is around 12 atm and field is 12.6 G, $D \approx 0.16 \text{ cm}^2/\text{s}$ and the field inhomogeneities are 10 mG/cm , the relaxation rate is $1/1400 \text{ hr}^{-1}$.

Wall relaxation is typically the dominant relaxation mechanism for cells in our

lab. This mechanism depends on the properties of the inner surface of glass. Most of the target cells are constructed with reblown General Electric Type 180 (GE-180) glass. This aluminosilicate glass is highly impermeable to ${}^3\text{He}$. The wall relaxation is believed to be associated to several different mechanisms, such as paramagnetic impurities in the glass and microfissures in the surface that could trap ${}^3\text{He}$ atoms. It has been found reblowing the glass can help lower the wall relaxation rate because it reduces the number of microfissures. The wall relaxation is not well understood, but it is believed to scale with the surface-to-volume ratio:

$$\Gamma_{wall} = \rho S/V \quad (2.36)$$

where ρ is called relaxivity.

2.5 X Factor

In 2006, Babcock *et al.* [17] reported evidence of a previously unrecognized spin relaxation mechanism, and named it X factor. This mechanism appears to be temperature dependent and roughly proportional to alkali density. The X factor limits the maximally achievable ${}^3\text{He}$ polarization even with infinite laser power. The saturation polarization is

$$P_{\infty}^{{}^3\text{He}} = P_{\infty}^{Rb} \frac{\gamma_{se}}{\gamma_{se}(1 + X) + \Gamma} \quad (2.37)$$

In the presence of infinite laser power where $\gamma_{se} \gg \Gamma$, the saturation polarization becomes

$$P_{\infty}^{{}^3\text{He}} = P_{\infty}^{Rb} \frac{1}{1 + X} \quad (2.38)$$

The X factor will be discussed in greater detail in chapter 4.

Chapter 3

^3He Polarimetry

3.1 Overview

Historically, pure-glass target cells used in electron scattering experiments have been studied mainly using Adiabatic Fast Passage (AFP) [41] Nuclear Magnetic Resonance (NMR) and Electron Paramagnetic Resonance (EPR) [42]. AFP is a technique that allows us to monitor a signal that is directly proportional to the ^3He polarization, which serves as a means to gain knowledge of properties of cell including the time it takes to polarize it and the relaxation rates of its polarization. The EPR technique utilizes the fact that polarized ^3He produces frequency shift of the magnetic resonance lines of alkali metal to measure the ^3He polarization. When AFP and EPR are combined, we can calculate the calibration constant between an AFP signal and the corresponding ^3He polarization.

A significant focus of my studies was on exploring cells that incorporated metal. Unfortunately, AFP is not suitable for studying such cells as it requires exposing the entirety of the cell to a Radio Frequency (RF) magnetic field in an attempt to flip all spins in the cell more-or-less simultaneously. The RF field would induce Eddy

currents in the metal portions of the cell that would significantly affect the resulting signal. For glass and metal cells, Pulsed Nuclear Magnetic Resonance (PNMR) has proven to be very useful. Using PNMR, it is possible to apply the RF field to a small selected part of the cell which makes it relatively easy to prevent metal from distorting the signal.

This chapter introduces the three techniques mentioned above and how they're used for our studies.

3.2 Adiabatic Fast Passage

3.2.1 Nuclear Magnetic Resonance

The energy of a magnetic moment in an external field is

$$E = -\vec{\mu} \cdot \vec{B}_0 = -\mu_z B_0 \quad (3.1)$$

where $\vec{\mu}$ is the magnetic moment. For a spin-1/2 nucleus, the energy is

$$E = -\gamma B_0 \hbar / 2 \quad (3.2)$$

where γ is the gyromagnetic ratio, and $\gamma/2\pi \approx 3.2434 \text{ kHz/Gauss}$ for ^3He . When a nucleus is placed in an external magnetic field that is not aligned with its magnetic moment, it will precess at the Larmor frequency. The Larmor frequency is defined as $\omega = \gamma B_0$.

3.2.2 The Rotating Coordinate System

3.2.2.1 Classical Formulation

For a nucleus in an external field \vec{B} with $\gamma\hbar\vec{I}$ as its nuclear angular momentum, the equation of motion in a stationary coordinate system is [43]

$$\hbar \frac{d\vec{I}}{dt} = \gamma\hbar\vec{I} \times \vec{B}. \quad (3.3)$$

Let $\frac{\partial}{\partial t}$ represent the derivative with respect to a coordinate system that rotates with angular velocity $\vec{\omega}$, then

$$\frac{d\vec{I}}{dt} = \frac{\partial\vec{I}}{\partial t} + \vec{\omega} \times \vec{I}. \quad (3.4)$$

Substitute Eq. 3.4 into Eq. 3.3, \vec{I} in the rotating frame satisfies the equation of motion

$$\hbar \frac{\partial\vec{I}}{\partial t} = \gamma\hbar\vec{I} \times (\vec{B} + \vec{\omega}/\gamma) = \gamma\hbar\vec{I} \times \vec{B}_{eff} \quad (3.5)$$

where \vec{B}_{eff} is the effective field in the rotating frame

$$\vec{B}_{eff} = \vec{B} + \vec{\omega}/\gamma \quad (3.6)$$

Thus, the effective field experienced by an observer in the rotating frame is simply the external field \vec{B} plus an additional field $\vec{\omega}/\gamma$.

If we apply this result to rotating magnetic fields, we will get the core idea of performing an Adiabatic Fast Passage (AFP) measurement. Assuming a constant field \vec{B} and another field \vec{B}_1 perpendicular to \vec{B} that is rotating with angular velocity $-\omega$. In the rotating frame that rotates with \vec{B}_1 , both aforementioned fields are just

constant and the effective field in the rotating frame is

$$B_{eff}\vec{z} = (B - \omega/\gamma)\vec{z} + B_1\vec{x}' \quad (3.7)$$

where \vec{x}' is the direction that \vec{B}_1 is in. When on resonance ($B = \omega/\gamma$), the effective field is perpendicular to the constant field \vec{B} .

3.2.2.2 Quantum Mechanical Formulation

The above conclusion can be easily reached with quantum mechanics [43]. The Shrödinger equation for a magnetic moment in an external field is

$$i\hbar\dot{\psi} = \mathcal{H}\psi = -\gamma\hbar\vec{I}\cdot\vec{B}\psi. \quad (3.8)$$

Let ψ and \vec{B} be the wave function and magnetic field respectively in a stationary frame and ψ_r and \vec{B}_r be the same quantities in a rotating frame with angular velocity $\vec{\omega}$. Using the rotation operator in quantum mechanics,

$$\psi = e^{-i\vec{\omega}\cdot\vec{I}t}\psi_r \quad (3.9a)$$

$$\vec{I}\cdot\vec{B}_r = e^{i\vec{\omega}\cdot\vec{I}t}\vec{I}\cdot\vec{B}e^{-i\vec{\omega}\cdot\vec{I}t} \quad (3.9b)$$

Substituting 3.9 into Eq.3.8, the Shrödinger equation in the rotating frame is obtained

$$i\hbar\dot{\psi}_r = -\gamma\hbar\vec{I}\cdot(\vec{B}_r + \vec{\omega}/\gamma)\psi_r = -\gamma\hbar\vec{I}\cdot\vec{B}_{eff}\psi_r \quad (3.10)$$

The same effective field in the rotating frame is reached as that from the classical derivation.

3.2.3 Adiabatic Fast Passage

The NMR technique of Adiabatic Fast Passage (AFP) is used to measure the ^3He polarization. In an AFP measurement, with the assistance of an oscillating radiofrequency (RF) field, the spins follow the effective field in a rotating frame (as discussed in more detail below) and are flipped 180 degrees to the opposite direction and then flipped back, producing two peaks in signal when they're perpendicular to the holding field and the pick up coils.

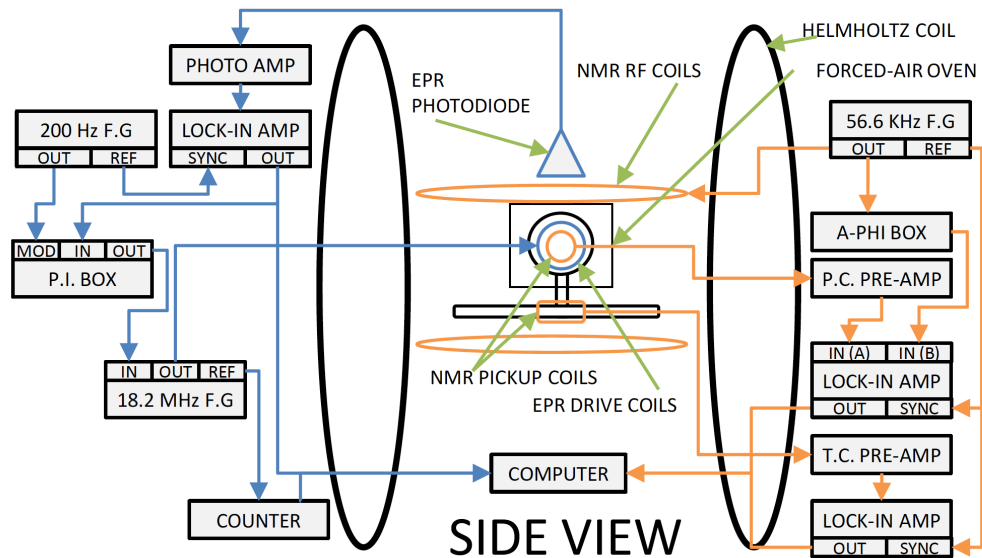


Figure 3.1: EPR (left) and AFP (right) setup. Adapted from Dolph's PhD thesis.

The flipping process can be achieved by either sweeping the main holding field or sweeping the RF frequency so that the longitudinal component of effective field in the rotating frame goes through zero. AFP measurements in our lab were typically done by sweeping the holding field while keeping the RF frequency constant. The RF coils produced an RF field of magnitude $2B_1$ perpendicular to the main holding field B . The oscillating field has a frequency of ω and can be decomposed into two counter-

rotating components with the same amplitude B_1 . Only the component rotating in the direction able to produce a resonance in Eq. 3.7 has an important effect. In this frame, the effective field is

$$\vec{B}_{eff} = (B - \omega/\gamma)\vec{z} + B_1\vec{x}' \quad (3.11)$$

as discussed above. The other rotating component that rotates in the opposite direction does not affect the spins. In an AFP measurement, the holding field starts from a value lower than ω/γ ($\omega/\gamma - B \gg B_1$), so that, initially, the effective field is almost aligned with the holding field and the spins. The holding field is then swept at a constant rate through resonance to a value greater than ω/γ . The sweeping rate is of great importance. The sweep needs to be slow enough so that the nuclear spins can follow the effective field

$$\frac{\dot{B}}{B_1} \ll \omega \quad (3.12)$$

Sweep rates that satisfy this condition are considered to be adiabatic.

Sweep rates cannot be too slow either, because the relaxation rate of the spins are faster near the resonance especially with a small effective field B_1 . The relaxation rate of ^3He in the rotating frame due to magnetic field inhomogeneities at resonance is [44]

$$\frac{1}{T_{1r}} = D \frac{|\nabla B_z|^2}{B_1^2} \quad (3.13)$$

where D is the ^3He self-diffusion constant. In order to keep the AFP loss low, it's important for the time scale during which the spins are close to resonance to be much

shorter than T_{1r} , so we want:

$$D \frac{|\nabla B_z|^2}{B_1^2} \ll \frac{\dot{B}}{B_1} \quad (3.14)$$

In the work presented here, the field was typically swept from 12.6 Gauss to 20.4 Gauss in 6s, thus

$$\dot{B} = 1.3G/s \quad (3.15a)$$

$$B_1 \approx 100mG \quad (3.15b)$$

$$f = 56.6kHz \quad (3.15c)$$

$$D \approx 0.16cm^2/s \quad (3.15d)$$

$$|\nabla B_z| \approx 10mG/cm \quad (3.15e)$$

$$(3.15f)$$

With these operating conditions,

$$D \frac{|\nabla B_z|^2}{B_1^2} \approx 1.6mHz \quad (3.16a)$$

$$\frac{\dot{B}}{B_1} \approx 13Hz \quad (3.16b)$$

$$\omega \approx 356kHz \quad (3.16c)$$

The AFP conditions were clearly well satisfied for our parameters. Fig.3.2 shows the evolution of effective field in the rotating frame during an AFP measurement.

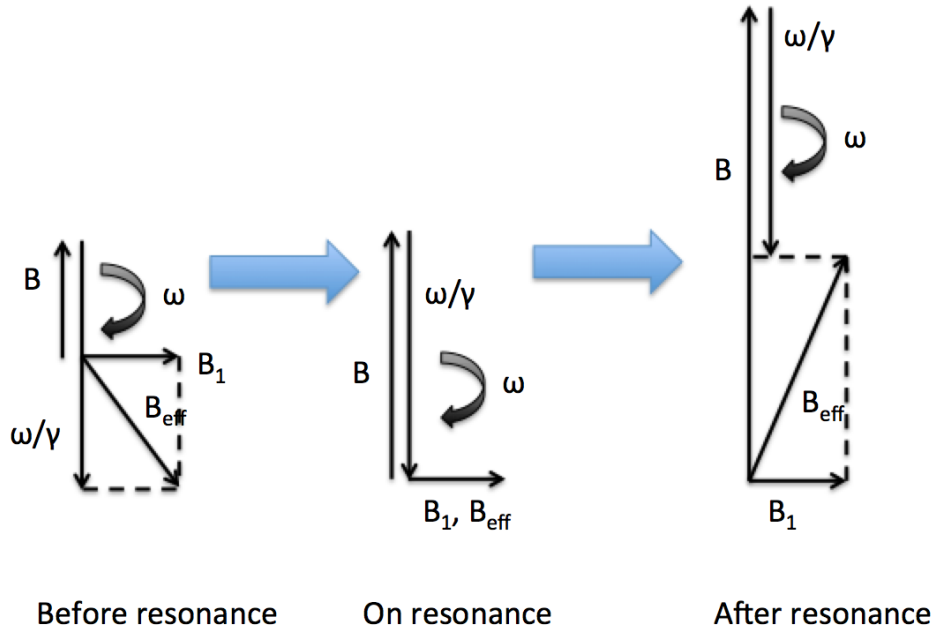


Figure 3.2: Effective field in the rotating frame during an Adiabatic Fast Passage measurement. The ^3He spins follow the direction of the effective field. B_1 is exaggerated to show different components of effective field clearly.

During our AFP measurements, the pick up coils were placed close to the cell, with their axis perpendicular to both the holding field and RF field. Under these conditions, as the ^3He spins precess along the holding field, the transverse component of the spins induces an electromotive force (EMF) that is directly proportional to the amplitude of the component in the pick up coils. The resulting signal can be written as:

$$S = A\omega \sin \alpha(t) = A\omega \frac{B_1}{\sqrt{B_1^2 + (B(t) - \omega/\gamma)^2}} \quad (3.17)$$

where A is a constant that accounts for the cell and coils geometry, the cell magnetization and the electronics factors that affect the size of signal; ω is the RF frequency;

α is the angle between the effective field and the holding field in the rotating frame; $B(t)$ is the holding field as a function of time. The signal reaches peak value when $B(t) = \omega/\gamma$. Fig.3.3 shows the result of a typical AFP measurement.

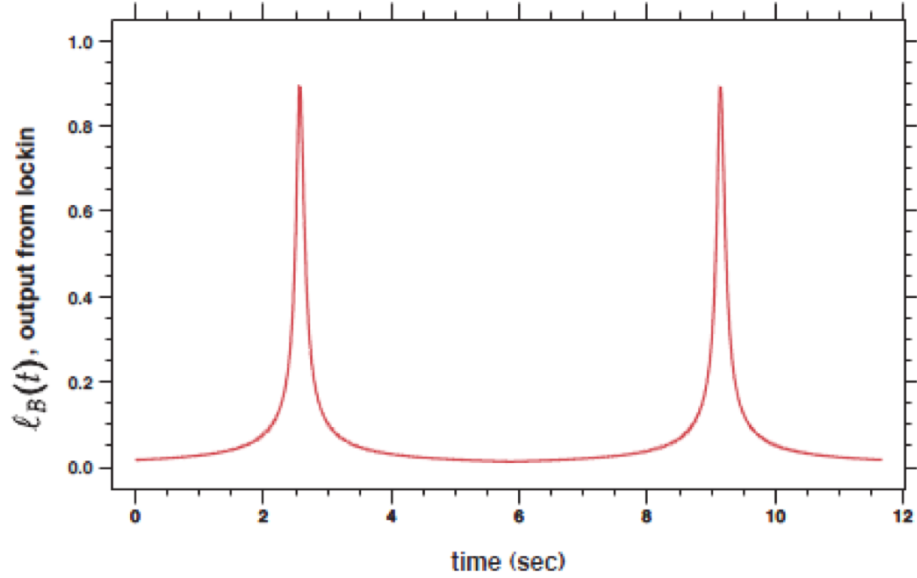


Figure 3.3: A typical AFP signal. y axis is in arbitrary unit.

3.2.4 AFP Loss

The longitudinal spin relaxation rate due to static field inhomogeneities is [38–40]

$$\frac{1}{T_1} = D \frac{|\nabla B_x|^2 + |\nabla B_y|^2}{B_0^2} \quad (3.18)$$

where D is the diffusion constant for the polarized spins, and is inversely proportional to the gas pressure. B_0 is the mean magnetic field along z axis. B_x and B_y are the x and y components of the magnetic field. However, when performing AFP measurement, the spins are exposed to a small oscillating RF field, the spin relaxation

can be greatly accelerated under magnetic resonance conditions [44],

$$\frac{1}{T_{r1}} = \frac{8R^4}{175D} |\nabla\Omega_z|^2 \sum_n \frac{175}{4(\chi_{1n}^2 - 2)(\chi_{1n}^4 + r^2 + r^2s^2)(1 + s^2)} \quad (3.19)$$

where R is the cell radius, D is the diffusion constant, Ω_z is the Larmor frequency of the holding field, $r = \frac{\omega_r R^2}{D}$, $s = \frac{\Omega_0 - \omega}{\omega_r}$, and the numbers χ_{1n} are the zeros of the derivatives of the spherical Bessel functions

$$\frac{d}{dx} j_1(x_{1n}) = 0 \text{ for } n = 1, 2, 3\dots \quad (3.20)$$

Since $r^2 \gg \chi_{1n}^4$, and $\sum_n \frac{1}{\chi_{1n}^2 - 2} = \frac{1}{2}$ [40],

$$\frac{1}{T_{r1}} = \frac{R^4 |\nabla\Omega_z|^2}{r^2(1 + s^2)^2 D} = \frac{|\nabla B_z|^2 D}{B_1^2(1 + s^2)^2} \quad (3.21)$$

If P_0 is the polarization before AFP, the polarization P after a single AFP flip is given by

$$P = P_0 e^{-\int \Gamma_{r1} dt} = P_0 e^{-\int \frac{1}{T_{r1}} dt} \quad (3.22)$$

Thus fraction loss L_{AFP} due to a single AFP flip is:

$$L_{AFP} = 1 - e^{\int \frac{1}{T_{r1}} dt} \approx \int \frac{1}{T_{r1}} dt \quad (3.23)$$

For our conditions, the integration limits can be extended to $\pm\infty$, making it possible to calculate the integral as:

$$\int_{-\infty}^{\infty} \frac{1}{T_{r1}} dt = \frac{\pi D |\nabla B_z|^2}{2B_1 \partial B_1 / \partial t} \quad (3.24)$$

which is the fractional loss due to a single AFP flip.

To better understand AFP loss, we performed a study where we took AFP measurements at various different field gradients to study the relation between AFP loss and inhomogeneities. The gradients were produced by Maxwell-style transverse gradient coils and increased from 0 to a little under 160 mG/cm. At each set gradient, we take one AFP to look at the difference between the two peaks to determine the loss due to a single flip. Fig 3.4 shows AFP losses collected from experiments and theoretical predictions. They agree within the error bar.

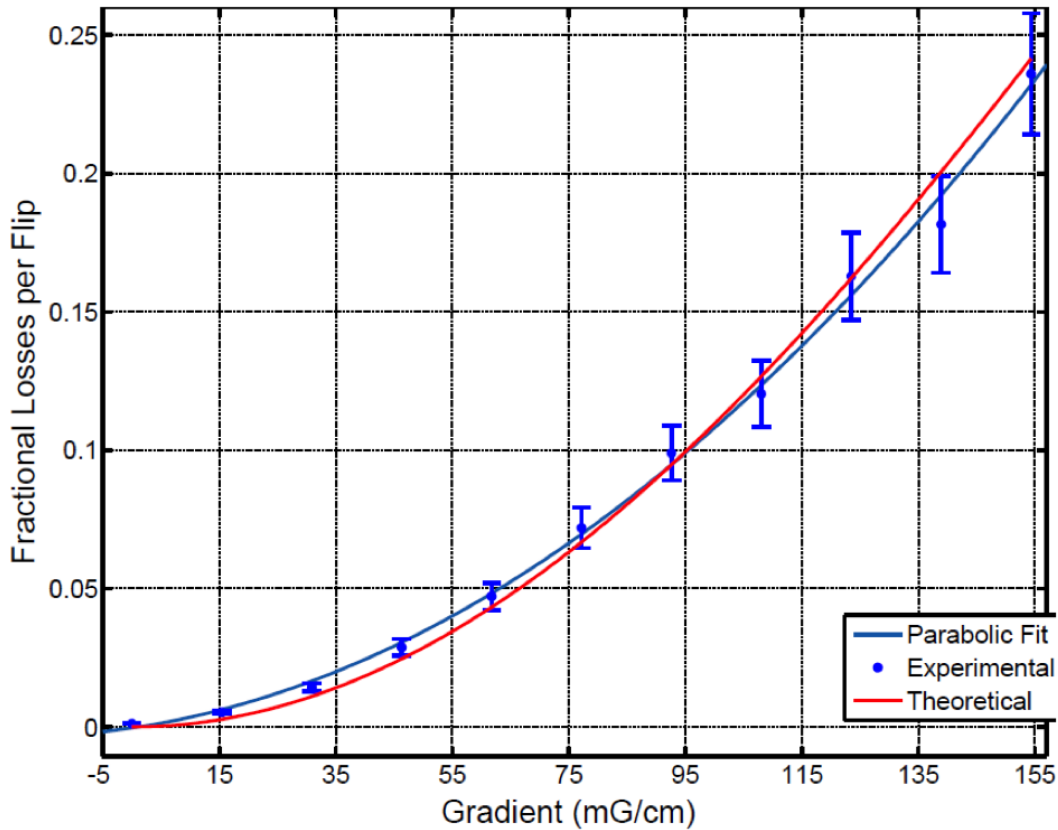


Figure 3.4: Fractional AFP loss (single flip) as a function of field gradient.

3.3 Electron Paramagnetic Resonance

3.3.1 Overview

Electron Paramagnetic Resonance (EPR) provides an important technique for measuring the frequency shift of alkali metal Zeeman resonances due to the effective magnetic field produced by polarized ^3He gas. During spin-exchange collisions, the alkali valence electron is essentially located within the ^3He nucleus thus facilitating a Fermi contact interaction between their spins. The EPR shift is largely caused by this Fermi-contact interaction $\alpha \mathbf{K} \cdot \mathbf{S}$ between the nuclear spin \mathbf{K} of the noble gas nucleus of magnetic moment μ_K and the electron spin \mathbf{S} of the alkali metal atom [45]. The magnetic field created by the bulk magnetization of the ^3He gas also contributes directly to a relatively small part of the shift (roughly 1/6 for K). Because the spin-exchange effective field is difficult to calculate accurately from theory, the total measured shift is usually written as the expected Zeeman interaction with the field produced by the polarized ^3He multiplied by an atomic parameter κ_0 . The value of κ_0 can be thought of as an enhancement due to attraction of the alkali electron wave function to the ^3He nucleus [42], which is different for each alkali metal species and slightly temperature dependent.

During the process of optical pumping, the Rb atoms are excited to the $5\text{P}_{\frac{1}{2}}$ state by the pump laser. The majority of these atoms are quenched non-radiatively to the ground state by N_2 . While in the $5\text{P}_{\frac{1}{2}}$ state, Rb atoms can also be excited to the $5\text{P}_{\frac{3}{2}}$ state through collisions with other Rb atoms. A small fraction of the excited atoms ($5\text{P}_{\frac{1}{2}}$ and $5\text{P}_{\frac{3}{2}}$) decay by emitting either a D_1 photon or D_2 photon. The intensity of fluorescence is proportional to the population of excited Rb atoms, and is thus higher when the Rb polarization is low so more Rb atoms can absorb laser and jump to the excited state. We typically induce Zeeman transitions with an RF coil to lower

alkali polarization and detect D₂ photons with a photodiode behind a D₂ filter. The highest amount of D₂ photons is detected when the RF frequency is exactly equal to the Zeeman transition frequency.

3.3.2 The Breit-Rabi Equation

The Zeeman energy levels of ground state (L = 0) can be described with the Breit-Rabi equation[46]

$$E_{F=I\pm 1/2, m_F} = -\frac{h\Delta\nu_{hfs}}{2(2I+1)} - \mu_N g_I B m_F \pm \frac{h\Delta\nu_{hfs}}{2} \sqrt{1 + \frac{4m_F x}{2I+1} + x^2} \quad (3.25)$$

where

$$x = (g_I \mu_N - g_s \mu_B) \frac{B}{h \Delta\nu_{hfs}} \quad (3.26)$$

B is the magnetic field, $\Delta\nu_{hfs}$ is the hyperfine splitting frequency, I is the nuclear spin, g_I and g_s are the g factors of nuclear and electron spin, μ_N and μ_B are the nuclear and Bohr magneton, respectively.

The Zeeman transition frequency of $m_F \rightarrow m_F - 1$ is

$$\begin{aligned} \nu_{m_F \rightarrow m_F - 1} &= \frac{E_{F,m_F} - E_{F,m_F-1}}{\hbar} \\ &= -\frac{g_I \mu_N B}{\hbar} \pm \frac{\Delta\nu_{hfs}}{2} \left(\sqrt{1 + \frac{4m_F}{2I+1} x + x^2} - \sqrt{1 + \frac{4m_F - 1}{2I+1} x + x^2} \right) \end{aligned} \quad (3.27)$$

The second term is much greater than the first term under our operating conditions, so the sign of the frequency $\nu_{m_F \rightarrow m_F - 1}$ depends on the second term only. If we

focus on the $F = I + \frac{1}{2}$ hyperfine manifold, the transition frequency is

$$\nu_{m_F \rightarrow m_{F-1}} = -\frac{g_I \mu_N B}{h} + \frac{\Delta \nu_{hfs}}{2} \left(\sqrt{1 + \frac{4m_F}{2I+1}x + x^2} - \sqrt{1 + \frac{4m_F-1}{2I+1}x + x^2} \right) \quad (3.28)$$

3.3.3 Shift of Zeeman Frequency

Under our operating condition, the size of Zeeman splitting is much less than hyperfine splitting, which makes x a small number. The Taylor expansion of Eq. 3.28 is

$$\begin{aligned} \nu_{m_F \rightarrow m_{F-1}} = & -\frac{g_I \mu_N B}{h} \\ & + \frac{\Delta \nu_{hfs}}{2} \left(\frac{2x}{2I+1} - \frac{2(2m_F-1)x^2}{(2I+1)^2} + \frac{(-(2I+1)^2 + 4 - 12m_F + 12m_F^2)x^3}{(2I+1)^3} + \dots \right) \end{aligned} \quad (3.29)$$

with the approximation

$$g_s \mu_B \gg g_I \mu_N \quad (3.30a)$$

$$x \approx -\frac{g_s \mu_B B}{h \Delta \nu_{hfs}} \quad (3.30b)$$

then to the lowest order approximation, the shift of $\nu_{m_F \rightarrow m_{F-1}}$ due to a small effective field ΔB ($\Delta B \ll B$) from polarized ^3He is

$$\begin{aligned} \Delta \nu_{m_F \rightarrow m_{F-1}} = & -\frac{g_s \mu_B}{h(2I+1)} \Delta B \left[1 + 2(2m-1) \frac{g_s \mu_B B}{h \Delta \nu_{hfs} (2I+1)} \right. \\ & \left. + 6 \left(-\frac{(2I+1)^2}{4} + 1 - 3m + 3m^2 \right) \left(\frac{g_s \mu_B B}{h \Delta \nu_{hfs} (2I+1)} \right)^2 + \dots \right] \end{aligned} \quad (3.31)$$

Usually the pumping chamber is spherical, the magnetic field produced inside a uniformly magnetized sphere is [47]

$$\Delta \mathbf{B} = \frac{2}{3} \mu_0 \mathbf{M} \quad (3.32)$$

where μ_0 is the vacuum permeability, \mathbf{M} is the magnetization of ${}^3\text{He}$,

$$\mathbf{M} = \boldsymbol{\mu}_K [\text{He}] P, \quad (3.33)$$

$\boldsymbol{\mu}_K$ is the magnetic moment of ${}^3\text{He}$, $[\text{He}]$ is its density, and P is its polarization. As we mentioned before, as a result of the Fermi-contact interaction $\alpha \mathbf{K} \cdot \mathbf{S}$ between the nuclear spin \mathbf{K} of the noble gas nucleus and the electron spin \mathbf{S} of the alkali metal atom, the effective magnetic field felt by alkali metal due to the polarized ${}^3\text{He}$ nuclei is κ_0 [42]:

$$\Delta \mathbf{B} = \frac{2}{3} \kappa_0 \mu_0 \boldsymbol{\mu}_K [\text{He}] P \quad (3.34)$$

The enhancement factor κ_0 was measured by Romalis and Cates in 1998 with an error of 1.5% [42]

$$\kappa_0^{Rb-{}^3He} = 4.52 + 0.00934[T(\text{ }^\circ\text{C})] \quad (3.35)$$

then it was measured by Babcock *et al.* in 2005 [45]

$$\kappa_0^{Rb} = 6.39 + 0.00914[T - 200(\text{ }^\circ\text{C})] \quad (3.36a)$$

$$\kappa_0^K = 5.99 + 0.0086[T - 200(\text{ }^\circ\text{C})] \quad (3.36b)$$

$$\kappa_0^{Na} = 4.84 + 0.00914[T - 200(\text{ }^\circ\text{C})] \quad (3.36c)$$

The two results agree within the error. Thus we can calculate ^3He polarization with the EPR frequency shift.

3.3.4 Experimental Methods

3.3.4.1 Overview

Under operating conditions typical when using a polarized ^3He target, hybrid cells with mixture of Rb and K are used. The vapor density of K is around 6 times as that of Rb, we typically induce the ^{39}K transition corresponding to $m_F = 2 \rightarrow m_F = 1$ (assuming the angular momentum of laser photons is +1), which lowers the K polarization. The Rb-K spin-exchange rate is fast enough that the Rb is depolarized almost instantly. This allows more Rb atoms to absorb laser and be excited to the $5\text{P}_{\frac{1}{2}}$ state which in turn produces more D_2 fluorescence. The D_2 fluorescence is at maximum intensity when the RF frequency is on resonance for the Zeeman transition.

We first locate the frequency with a frequency-modulated (FM) sweep, and set the RF frequency to the found value. The RF is locked to the frequency that induces maximum D_2 light using a proportional-integral feedback circuit (P.I. box). This frequency is referred to as the EPR frequency and is measured with a frequency counter. To separate the frequency-shifting effect of polarized ^3He from other sources that may affect the transition frequency, we flip the ^3He magnetization by performing AFP using an RF frequency sweep. A frequency sweep is chosen rather than a holding field sweep to keep external magnetic field constant, thus reducing factors that affect Zeeman splitting size. No signal is recorded during these sweeps, as the varying frequency would affect the amplitude of AFP signals. By comparing the frequency measured before and after the flip, together with the real temperature inside the pumping chamber, we can calculate the ^3He polarization. We typically take AFP

measurements (in our usual way using a magnetic field sweep) right before and after the relatively quick EPR measurement, so that a calibration constant that translates AFP signal size to ^3He polarization can be calculated.

3.3.4.2 Locating Zeeman Transition Frequency

The P.I. box only works well in locking the EPR frequency to the $m_F = 2 \rightarrow m_F = 1$ K transition when the EPR frequency is close to the transition. Thus, the first step in EPR measurements is to locate the Zeeman transition. A frequency-modulated (FM) sweep is performed through a range that covers the Zeeman transition, the range is known from experience or calculation and the P.I. box remains off during the sweep.

The RF frequency is generated by a voltage-controlled oscillator (VCO). The D_2 fluorescence is detected with the photodiode and recorded during the sweep. The RF is frequency-modulated by a 200Hz signal, and the VCO output at any moment during the sweep can be described as:

$$V_{FM}(t) = V_{C0} \sin(2\pi[f_c + D_f \sin(2\pi f_m t + \phi_m)]t + \phi_c) \quad (3.37)$$

where V_{C0} is the amplitude of the sweeping RF frequency (carrier), f_c is the RF frequency that is being swept through a set range, D_f is the peak frequency deviation, f_m is the modulating frequency (200Hz in our case), and ϕ_m and ϕ_c are the phase of the modulation frequency and carrier frequency, respectively. Thus, the RF frequency is

$$f_{FM}(t) = f_c(t) + D_f \sin(2\pi f_m t + \phi_m) \quad (3.38)$$

where $f_c(t)$ emphasizes the RF frequency is sweeping over time.

The D_2 light intensity can be described with a Lorentzian function:

$$I(f(t)) = \frac{I_0}{(f_{FM}(t) - f_0)^2 + \Gamma^2} \quad (3.39)$$

where f_0 is the Zeeman transition frequency, Γ is the line width. Keeping the first order term of the Taylor expansion of Eq. 3.39, the D_2 light intensity is

$$I(f(t)) = I(f_c(t)) + \frac{\partial I}{\partial f} \Big|_{f=f_c(t)} D_f \sin(2\pi f_m t + \phi_m) \quad (3.40)$$

A lock-in amplifier is used to select only the f_m term to reduce the noise, which is proportional to the derivative of the Lorentzian function multiplied by a sine function. The FM sweep line crosses zero when the RF frequency is equal to the Zeeman transition frequency (peak of the Lorentzian function), which produces the maximum D_2 light intensity. The region between the lowest and highest points of the derivative line is fitted to a line, and the zero-crossing point of the line is used as the Zeeman transition frequency. Fig. 3.5 shows an FM sweep.

3.3.4.3 EPR Spin Flip Process

After the transition frequency is located, the VCO frequency is first set to it and then locked with a proportional-integral feedback circuit (P.I. box). The circuit is shown in Fig. 3.6.

The output of the lock-in amplifier serves as an error signal and the input to the P.I. box. The output of the P.I. box is thus forced to a condition that minimizes the error signal and keeps the VCO centered on the resonant frequency.

Because the EPR frequency is also affected by sources other than the polarized ^3He such as the holding field and earth field, we flip the ^3He spins by sweeping the frequency while keeping the holding field unchanged. The contribution from

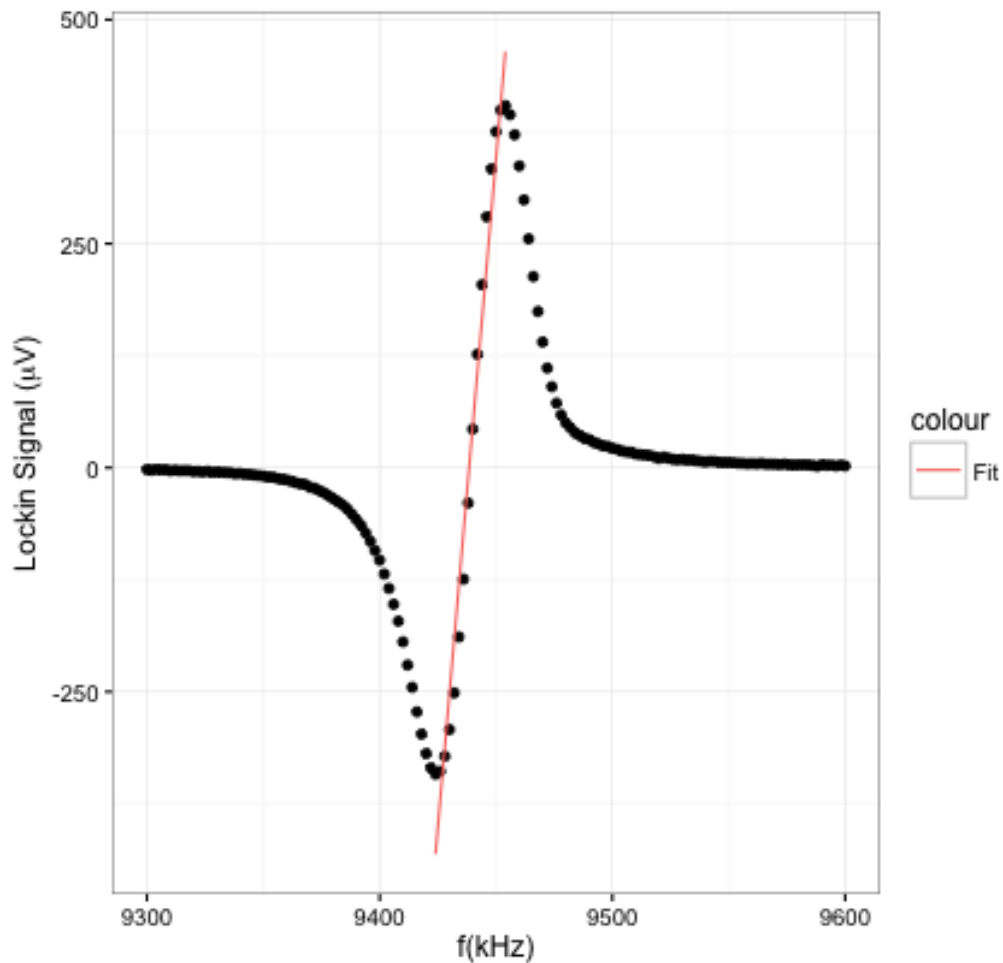


Figure 3.5: A typical FM sweep on a hybrid cell. The central region between the minimum and maximum is fitted to a line. The zero crossing point corresponds to the Zeeman transition frequency.

the flipped spins has the opposite sign while other factors still contribute in the same way, which allows us to extract the change of Zeeman transition frequency due to polarized ^3He , and consequently, calculate the polarization. We typically let the cell polarization reach saturation before performing EPR measurements. AFP measurements are taken right before and after the EPR measurements for calculating the calibration constant (the ratio between polarization and AFP signal size). Fig. 3.7 shows a typical EPR spin flip process.

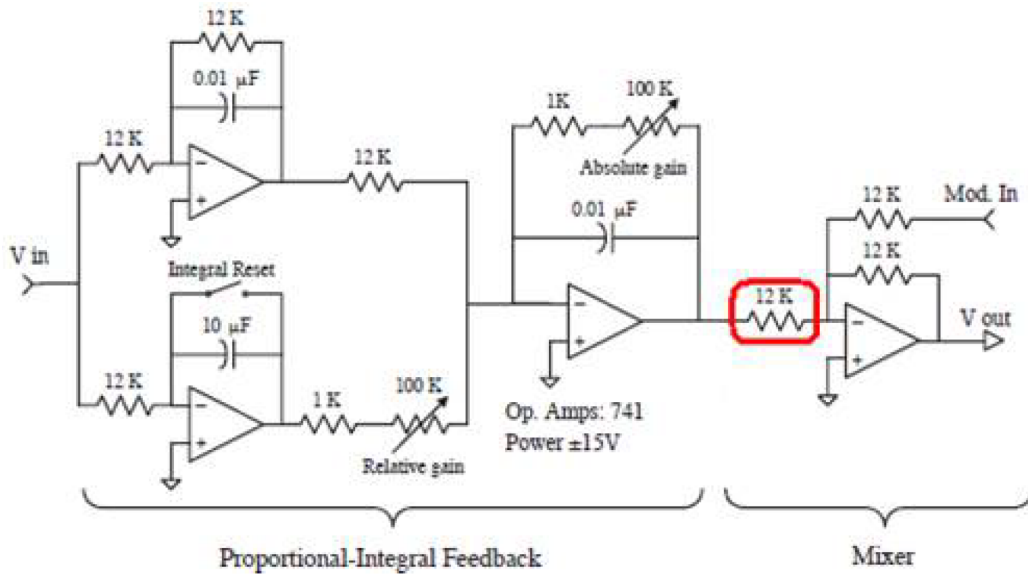


Figure 3.6: The same P.I. circuit that was first used by Romalis in our lab. The drawing was then corrected by Peter Dolph.[3]

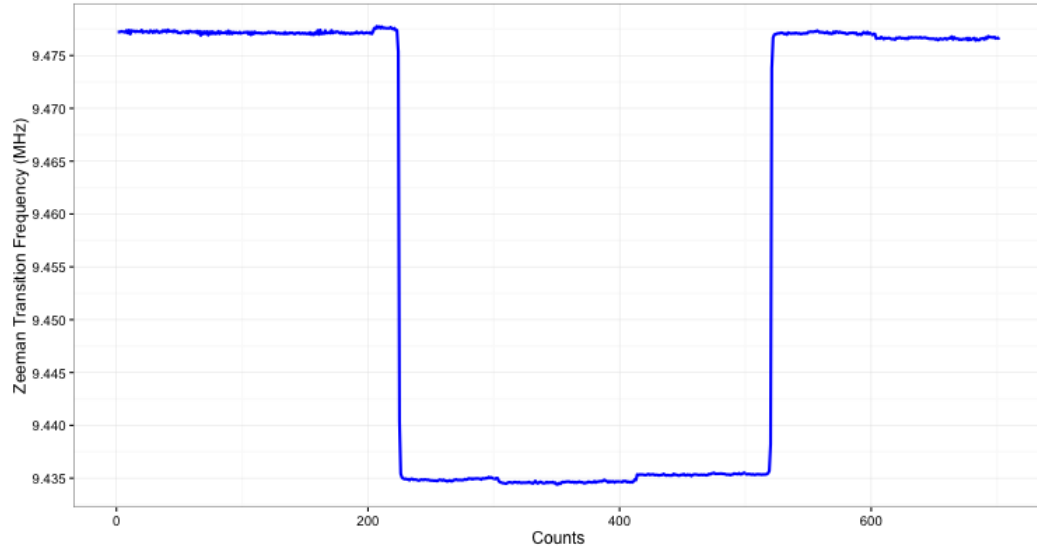


Figure 3.7: An EPR measurement for a hybrid cell at 235°C. The spins are flipped around 200 mark, and flipped back around 500 mark.

Under normal operating conditions for a double-chambered cell, the pumping chamber is heated to around 170°C or 235°C depending on if the cell is hybrid, while the target chamber and transfer tube remain at room temperature. The temperature

difference causes differences in gas densities and affects the AFP signal size. The temperature controller of the oven only maintains the surface temperature of the pumping chamber at a set temperature, but the gas inside the pumping chamber is always hotter due to absorption of laser energy. The enhancement factor κ_0 is also slightly temperature dependent which may be underestimated by $\sim 4\%$ when using the surface temperature as the gas temperature. Dolph described a method we referred to as a “temperature test” to extract gas temperature inside the pumping chamber in detail in his thesis [3]. In a temperature test, we take AFP measurements when the laser is blocked and unblocked multiple times. With the assumptions that the change of gas densities due to absorption of laser and AFP losses are the only reasons for the difference in signal size, and the temperature measured by RTDs on the exterior of the pumping chamber truly reflects the gas temperature when laser is blocked, one can calculate the inside temperature when laser is unblocked.

3.4 Pulsed Nuclear Magnetic Resonance

Adiabatic Fast Passage has been the main technique used in our lab for monitoring relative ^3He polarization during various studies. In an AFP measurement, all ^3He spins are flipped by sweeping the holding field while applying an RF field. As discussed by Chapter 5, we have been exploring the possibility of replacing conventional glass windows with metal end windows for future experiments planned during the 12 GeV era. Because of the lack of studies on spin relaxation of polarized ^3He on metal surfaces, various test cells made with large metal parts as well as glass parts are being studied in our lab. The inclusion of metal parts immediately renders AFP almost useless because of effects such as Eddy currents. Thus, we have been using Pulsed Nuclear Magnetic Resonance (PNMR) for monitoring polarization when studying

cells that include metal parts.

3.4.1 The Rotating Coordinate System

In a PNMR measurement, a short pulse of RF frequency is applied to a small localized portion of ^3He gas. The RF frequency is tuned to be on resonance at the Larmor frequency of the holding field. As discussed before with AFP, in the rotating coordinate system, there will be an effective field due to rotation that exactly cancels the holding field which we assume to be in the z direction. Thus the z component of the effective field is zero and there is a non-zero constant transverse component which we will call B_1 . The nuclear spins will precess along B_1 and end up at an angle away from z axis:

$$\alpha = \gamma B_1 \Delta t \quad (3.41)$$

where α is the angle (tip angle), γ is the gyromagnetic ratio, and Δt is the RF pulse duration.

3.4.2 Free Induction Decay

At the end of the RF pulse, the tipped spins will have a transverse component equal to the magnetization multiplied by $\sin \alpha$. The spins continue to precess along the holding field and the transverse component will induce a signal in the pickup coils (wrapped around the transfer tube as shown in Fig. 5.10) whose axis is perpendicular to the holding field.

In addition to precession, the spins are affected by two types of relaxation processes. The first type is called the spin-lattice relaxation, it describes the rate at which the longitudinal component of magnetization approaches the thermodynamic

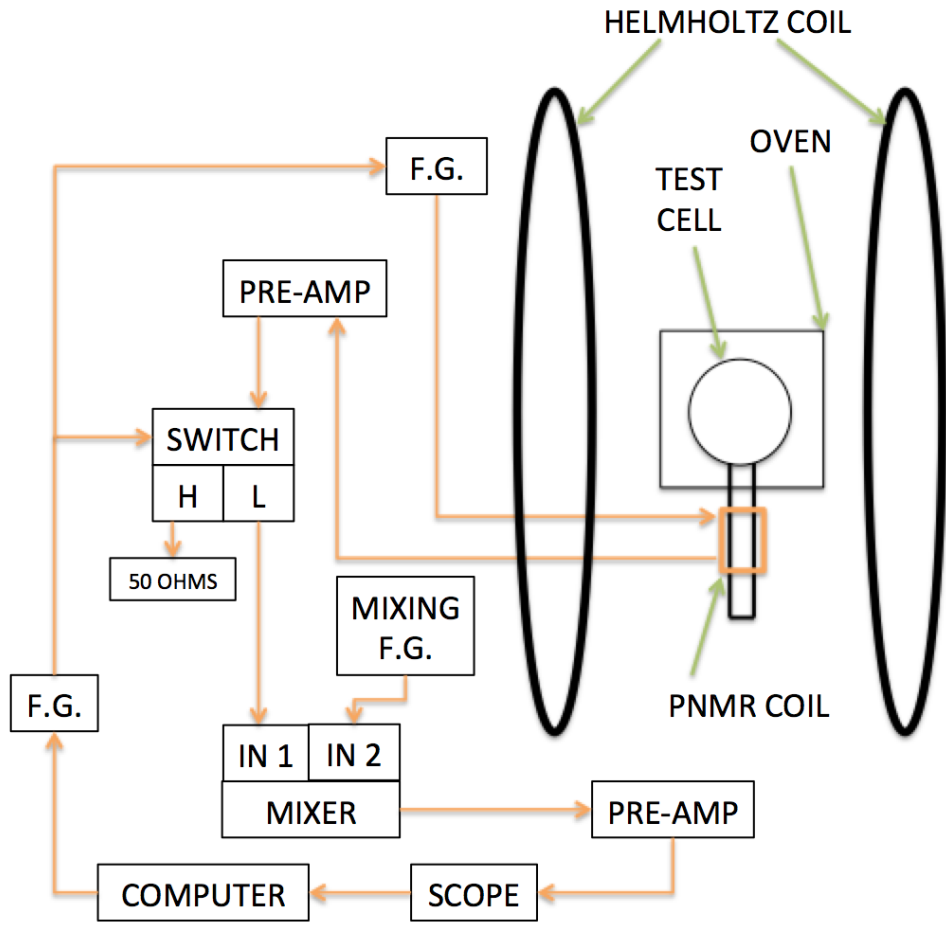


Figure 3.8: PNMR setup.

equilibrium value. It is characterized by the spin-lattice relaxation time constant T_1 .

The rate of change of the longitudinal component is

$$\dot{M}_z = -(M_z - M_0)/T_1 \quad (3.42)$$

where M_0 is the thermodynamic equilibrium magnetization. Solving the differential equation gives

$$M_z(t) = M_0 - [M_0 - M_z(0)] e^{-t/T_1} \quad (3.43)$$

The name spin-lattice relaxation refers to the process in which the spins transfer energy to surrounding, thereby restoring their equilibrium state.

The second relaxation process is relaxation in the transverse plane, which is also referred to as the T_2 relaxation and was historically called “spin-spin relaxation”. The transverse component of magnetization decays because random fluctuations of the holding field cause different moments to precess at different rates. This is the T_2 process. Normally, the dominating relaxation effect however, is another dephasing process due to holding field inhomogeneities over the volume of the cell.

The measured transverse relaxation rate of the tipped spins is the result of all these effects combined:

$$\frac{1}{T_2^*} = \frac{1}{T_2} + \gamma \Delta B_0 \quad (3.44)$$

where ΔB_0 is the variation in the holding field. $\gamma \Delta B_0$, the dominant term, is a spread in Larmor frequencies $\Delta\omega_0$, which causes spin-spin dephasing in a characteristic time of $1/\Delta\omega_0$.

The time evolution of the nuclear magnetization \mathbf{M} can be described by the Bloch equations [48]:

$$\frac{\partial M_x(t)}{\partial t} = \gamma (\mathbf{M}(t) \times \mathbf{B}(t))_x - \frac{M_x(t)}{T_2^*} \quad (3.45a)$$

$$\frac{\partial M_y(t)}{\partial t} = \gamma (\mathbf{M}(t) \times \mathbf{B}(t))_y - \frac{M_y(t)}{T_2^*} \quad (3.45b)$$

$$\frac{\partial M_z(t)}{\partial t} = \gamma (\mathbf{M}(t) \times \mathbf{B}(t))_z - \frac{M_z(t)}{T_1} \quad (3.45c)$$

where γ is the gyromagnetic ratio and the cross products are the precession terms, the last terms in each equation represent the decaying and dephasing of each component. The precessing spin magnetization generates a signal in the pickup coils that decays

with time. This is called free induction decay, the induced signal is typically described by

$$V(t) = A\omega_0 \sin \alpha \sin(\omega_0 t + \phi) e^{-t/T_2^*} \quad (3.46)$$

where A is just a constant, ω_0 is the Larmor frequency for the holding field, α is the tip angle, T_2^* is the measured decay time constant. For our metal test cells, depending on the location of the pickup coils and the field setup, T_2^* varies between several milliseconds to more than 300 milliseconds.

3.4.3 Experimental Methods

Our PNMR setup is shown in Fig. 5.10. The Labview program on the computer controlled the timing of a gate signal that was fired from the first function generator (F.G.). The gate signal was fed to the back of the second function generator and triggered it to produce a short pulse. The second function generator sent out RF pulse with pre-set amplitude, duration and frequency only when the gate signal was of voltage higher than the threshold. The frequency of the RF pulse was carefully tuned to be at the Larmor frequency of the holding field.

The pulse was sent from the function generator to a coil wrapped directly on a small portion of the cell. The spins in the proximity of the coil were exposed to the pulse and tipped by an angle which depended on the amplitude and the duration of the pulse. In the rotating frame, the effective field B_1 caused the spins to precess around it (as discussed before), the precession frequency was γB_1 so the angle the spins rotate by (tip angle) can be calculated by:

$$\alpha = \gamma B_1 \Delta t \quad (3.47)$$

where γ is the gyromagnetic ratio, the effective field B_1 is directly proportional to the amplitude of the RF pulse, and Δt is the duration of the pulse. Ideally, a 90° tip angle would result in the maximum signal, but it had not been the case for us most of the time. The coils were normally wrapped on the transfer tube of the cell which was off the center of the holding field and exposed to relatively large holding field inhomogeneities. Different groups of spins contributed to the FID signal also saw different values of B_1 . The details of how we measure the test cells will be discussed in later chapters. As a result, the spins precessed at different rates, and the dephasing became more significant with longer pulse duration and larger tip angle, which led to non-optimal signals. Exact tip angles of specific group of spins depended on location, a typical effective tip angle for the whole region would be between 30° and 45° .

After the spins were tipped away from z axis, they precessed around the holding field and induced a signal in the detection coil. The signal was amplified by a low noise pre-amplifier first and then went through an isolation switch. The switch only let signal pass when the controlling gate voltage was low, thus stopped the RF pulse from coming back through the detection circuit. The signal was at the Larmor frequency, and was mixed with another frequency after the switch. The mixing frequency was only slightly different from the Larmor frequency, the output of the mixer had both the sum of the two frequencies and the difference. A second pre-amplifier was used to select and amplify the lower of the two frequencies while filtering out high frequency noises. The final output was displayed on a oscilloscope and collected by the Labview program on the computer. Fig. 5.11 shows a PNMR measurement with around 150 ms decay time constant.

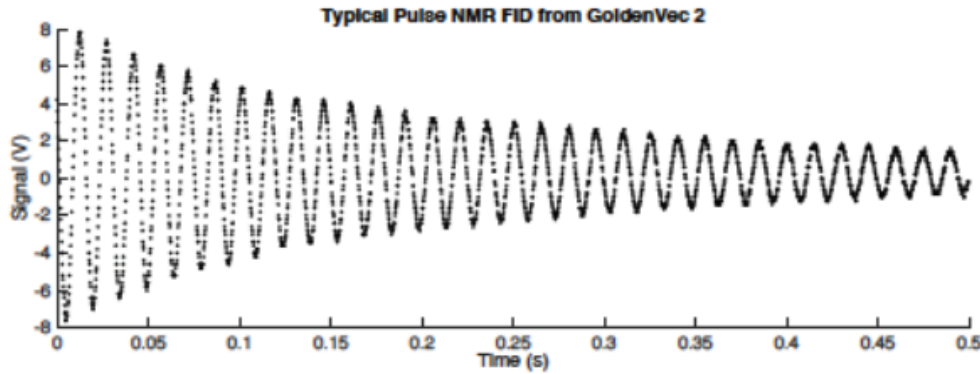


Figure 3.9: A PNMR signal taken with gold coated test cell.

The tip angle was measured with a short sequence of FID signals. Theoretically the tip angle can be calculated with Eq. 3.47. But because of inhomogeneities and other factors, the calculation serves as only an estimate in practice and it was often more accurate and convenient to measure the tip angle directly. We took several PNMR measurements in quick succession with the same RF pulse settings. After every pulse, the transverse component of the spins quickly decayed and dephased, leaving only the longitudinal component which was equal to $\cos \alpha$ times the original magnetization. The intervals between measurements were short enough so that T_1 can be safely ignored. The series of measurements also needed to be performed on the same portion of the gas (i.e. the same group of spins tipped by the first pulse), thus it was important to know that the self-diffusion of ^3He was significantly slower than the sampling rate. The self-diffusion coefficient of ^3He at 300K is [49]

$$D = \frac{1440(80)\text{torr}}{P} \text{cm}^2/\text{s} \quad (3.48)$$

which is roughly $1.89 \text{ cm}^2/\text{s}$ at 760 torr (the test cells normally contained around 1

atm of ^3He). The diffusion length is described by

$$l = 2\sqrt{Dt} \quad (3.49)$$

Thus in one second, the gas moved around 2.75 cm through self-diffusion. For this reason, we only took 2 or 3 PNMR measurements to calculate the tip angle. As additional measurements would have given enough time for the tipped spins from the first PNMR and the surrounding spins to mix.

Since only the longitudinal component of the tipped spins were preserved, the amplitude of the i_{th} PNMR was

$$V_i = V_0 \cos^{i-1} \alpha \quad (3.50)$$

where V_0 is the induced signal in the first PNMR. We could then use this equation to calculate the effective tip angle α .

Chapter 4

Development of Hybrid Targets

4.1 Overview

In this chapter, I present the development of high-performance polarized ${}^3\text{He}$ targets for use in electron scattering experiments that utilize the technique of alkali-hybrid spin-exchange optical pumping [18]. Data from 24 separate target cells are presented, each of these cells was constructed while preparing for one of four experiments at Jefferson Laboratory (JLAB). The results document dramatic improvement in the performance of polarized ${}^3\text{He}$ targets. I focus on the data analysis work in this chapter since most of the data had already been taken by the time I joined the group. Other details are described by Jaideep Singh [18]. With the wide range of data, we successfully determined the so-called X-factors that quantify an as-yet poorly understood spin-relaxation mechanism that limits the maximum achievable ${}^3\text{He}$ polarization to well under 100%. The data collected also served as a measurement of the K- ${}^3\text{He}$ spin-exchange rate coefficient $k_{se}^K = (7.46 \pm 0.62) \times 10^{-20} \text{ cm}^3/\text{s}$ over the temperature range 503 K to 563 K.

4.2 Development of Hybrid Targets

Spin-exchange optical pumping (SEOP) is a two step process in which an alkali-metal vapor is polarized with optical pumping which subsequently polarizes noble-gas nuclei via spin-exchange collisions[1]. A pure Rb vapor was used to polarize ${}^3\text{He}$ prior to the development of hybrid cells. However, it was found that K is far more efficient than Rb at transferring its polarization to ${}^3\text{He}$ nuclei [37]. Hybrid mixtures of Rb and K have subsequently been used to improve the efficiency of the polarization process [37, 50, 51]. In alkali-hybrid spin-exchange optical pumping (AHSEOP), the Rb vapor is polarized by circularly polarized laser light, but the polarization of Rb valence electrons is then rapidly shared with the K [29]. The rate at which Rb and K exchange polarization is so fast, for our purposes here, that their polarizations can be thought of as being equal. If the alkali-hybrid mixture contains significantly more K than Rb with an appropriate ratio, the spin-exchange efficiency is greatly improved so that the rate at which ${}^3\text{He}$ is polarized is increased significantly for a given amount of laser power.

The second factor that proved to have improved target cells performance greatly was the use of spectrally-narrowed diode lasers [52]. We were able to achieve higher alkali polarization with the aid of these lasers, which in turn reduced the required laser power. The origins of the improved cell performance are twofold. Firstly, these narrowband lasers have spectral profiles more closely matched to the Rb D₁ absorption line shapes, which results in higher optical pumping rates and hence higher alkali polarizations. Secondly, they contribute to allowing us to use higher alkali densities (which increases spin-exchange rates) without sacrificing alkali polarization.

The data collected over the years include ${}^3\text{He}$ polarization achieved under different operating conditions, the time constants of polarization process, the geometric

properties of the target cells, and cell fill information such as pressure and ratio of K to Rb in hybrid mixtures and the time constants of the spin-relaxation process. In roughly half the cells, the alkali polarization and alkali density were also measured with Faraday rotation techniques. The results contain several thousand hours worth of data and provide valuable information for future cell development.

Two figures of merit (FOMs) are plotted in Fig. 4.1, both of which are relevant in evaluating the performance of a polarized ${}^3\text{He}$ target. The one on the left axis is the effective luminosity $\mathcal{L}^{eff} = \mathcal{L}P_{He}^2$, where \mathcal{L} is the luminosity for a fixed-target experiment (the product of beam current, target density, and interaction length) and P_{He} is the ${}^3\text{He}$ polarization. The luminosity \mathcal{L} represents the number of scattering opportunities per unit time per unit area, while P_{He}^2 accounts for the reduction in effective statistics when measuring a polarization-dependant asymmetry. The FOM on the right axis is used to quantify the potential effective luminosity of a target. The definition is $\mathcal{L}^N = \mathcal{N}\Gamma_s P_{He}^2$, where \mathcal{N} is the total number of ${}^3\text{He}$ atoms in the target and Γ_s is the rate at which polarization builds up. The target cell Antoinette was the first one with such a high value of \mathcal{L}^N , which indicated the cell could tolerate higher luminosities than previously achieved. The high potential further demonstrates the importance of the development of the new convection style target cell [19]. With even higher luminosities in electron scattering experiments, significantly faster gas transfer becomes quite necessary to reduce the “polarization gradient” between the pumping chamber of target chamber.

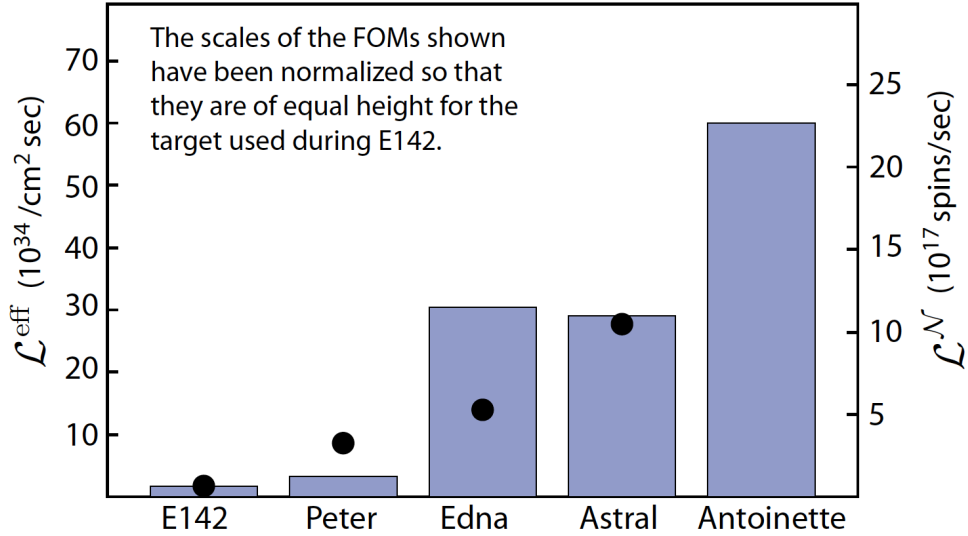


Figure 4.1: Shown are two figures of merit (FOM) for targets built for the indicated experiments. The circles (left axis) indicate the luminosity weighted by the square of polarization. The bars (right axis) represent the total number of spins being polarized per second weighted by the square of polarization. While the right FOM is an indication of the potential of the polarization technique, the left FOM indicates performance achieved during an experiment. The scales have been normalized so that the two FOMs have the same height for the cell marked E142

4.2.1 Experimental Methods

4.2.1.1 The ${}^3\text{He}$ Targets

Chapter 2 has already described single-chambered cell polarization dynamics to some extent as it is a simpler model for introducing spin-exchange optical pumping. The ${}^3\text{He}$ target cells JLab uses for electron scattering experiments usually include two chambers, a pumping chamber (PC), which is placed in an oven and pumped by circularly polarized laser light, and a target chamber (TC) that the electron beam passes through. Fig.4.2 shows a schematic representation of a typical cell.

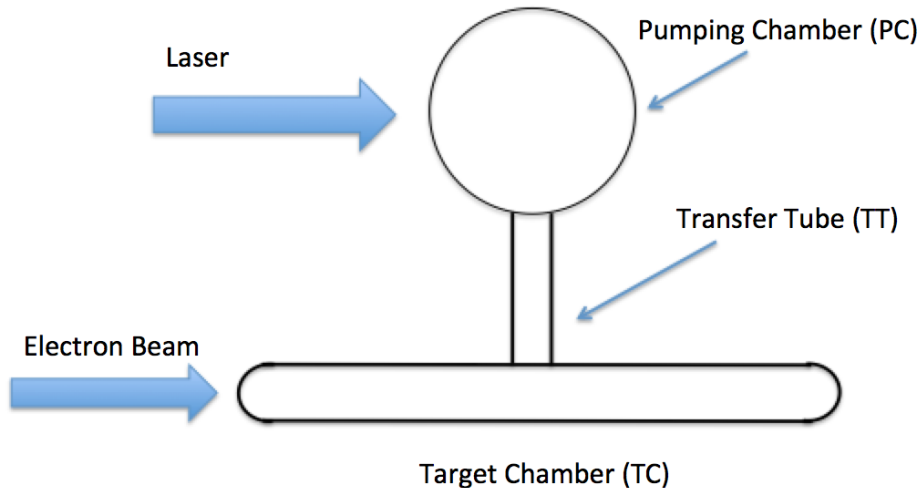


Figure 4.2: A target cell. The dimensions of different parts of the cell are not to scale.

After baking the cell to remove moisture and other contaminants, mixtures of Rb and K are “chased” into the cell with a hand torch. Once the cell has been pumped with a diffusion pump for about a week, we can fill the cell with N₂ and ³He.

The ³He density is of great importance for characterizing the target cells. One way to determine the ³He density is through measurements during the cell-filling process. A carefully calibrated volume, together with pressure and temperature measurements gives the volume of different spaces in the gas system (the system that is used to pump the cell and fill it with N₂ and ³He) and the cell itself. By comparing the amount of ³He left in the system, the amount that went into the cell is obtained. The volume of the cell can be measured by determining its buoyancy force in water. The ³He density is determined to within about 1% with the method.

Another method that can be used for determining the ³He density is through measurements of the pressure broadening of the D₁ and D₂ absorption lines with a

EXP	Cell	Total Volume(cc)	PC Volume(cc)	Fill Density(amg)	TC length(cm)
saGDH	Proteus	235.9	90.8	6.88	34.3
	Peter	208.6	111.3	8.80	39.4
	Penelope	204.3	102.2	8.93	39.7
	Powell	213.3	111.6	8.95	40.5
	Prasch	257.7	114.5	6.94	35.3
GEN	Al	168.4	90.2	8.91	38.4
	Barbara	386.2	306.8	7.60	38.7
	Gloria	378.2	298.8	7.40	38.4
	Anna	386.8	303.7	8.09	38.7
	Dexter	181.4	99.3	9.95	38.7
	Edna	378.3	290.3	7.47	38.7
	Dolly	378.3	293.5	7.42	38.7
	Simone	219.5	118.6	8.17	37.9
	Sosa	388.8	304.7	7.96	38.7
Transversity and d_2^n	Boris	246.1	166.1	8.08	38.4
	Samantha	259.0	176.9	7.97	38.4
	Alex	278.3	193.9	7.73	39.1
	Moss	269.8	184.7	7.92	38.7
	Tigger	271.7	186.9	7.81	38.7
	Astral	251.4	164.9	8.18	38.4
	Stephanie	244.3	164.9	8.10	38.5
	Brady	249.9	169.3	7.88	38.4
	Maureen	268.5	177.4	7.63	39.8
	Antoinette	437.8	351.8	6.57	40.3

Table 4.1: The table contains the names, total and pumping chamber volumes, fill densities and target chamber lengths of the 24 target cells. The fill densities are the average of the results from gas system measurements and pressure broadening measurements.

scannable single-frequency laser [2]. This measurement also provides the value of D, which we defined as the ratio of K vapor density to Rb vapor density. Although the value of D is for the temperature at which the measurement is performed, its value for operating conditions can be inferred with alkali-metal vapor pressure curves. D can also be measured with the Faraday rotation technique in many cases, and the two methods agree with each other quite well. The fill densities and geometric properties of the aforementioned 24 cells are shown in Table 4.1.

4.2.1.2 Target Cell Polarization Dynamics

As previously mentioned, AFP is used to monitor the polarization of ${}^3\text{He}$ [41]. An absolute value of polarization remains to be calibrated with EPR, but the signal size is

directly proportional to the polarization, thus is an indication of how the polarization changes relatively. Two processes that are monitored with AFP are spinups and spindowns. The details of the dynamics has been discussed in detail by Dolph *et al.* [19].

The study of the build up of ^3He polarization by spin-exchange optical pumping is something referred to here as spinup. A typical example of a spinup is shown in Fig. 4.3.

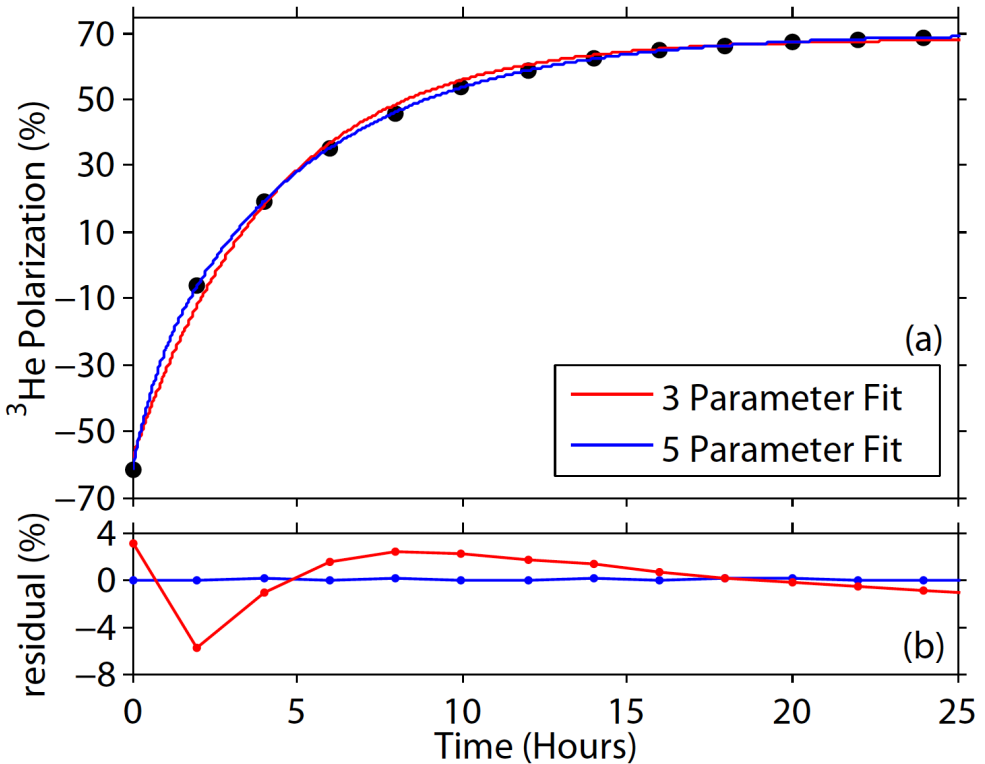


Figure 4.3: (a) Shown is a spinup of the target Brady. The spinup data has been fit with a 3-parameter and a 5-parameter formalism. (b) The residuals of the two fits. The error for 3-parameter fit is larger because it does not account for diffusion between two chambers.

The equation that describes spinups of a single-chambered cell is:

$$P(t) = (P^0 - P^\infty)e^{-\Gamma_{sc}t} + P^\infty \quad (4.1)$$

where P^∞ is the saturation polarization, P^0 is the initial polarization, $\Gamma_{sc} = \gamma_{se}(1 + X) + \Gamma$ is the spin-up rate of the buildup of polarization. The subscript “sc” here stands for “single chamber” to differ from the spinup rate of double-chambered cell. γ_{se} is the spin-exchange rate, X is a parameter used to characterize a source of spin relaxation that limits the maximal achievable polarization, which will be discussed in more detail later in the chapter. Γ is the spin relaxation rate due to mechanisms other than spin-exchange and that is characterized by the parameter X . Often Γ is dominated by relaxation at the cell walls. When using this equation to fit spinup, there are only three parameters, hence the name 3-parameter fit. The saturation polarization is given by:

$$P^\infty = \frac{\langle P_A \rangle \gamma_{se}}{\Gamma_{sc}} = \frac{\langle P_A \rangle \gamma_{se}}{\gamma_{se}(1 + X) + \Gamma} \quad (4.2)$$

where $\langle P_A \rangle$ is the polarization of the alkali vapor averaged over the cell.

The following derivation will only focus on double-chambered cell. The polarization accumulation rate can be described by

$$\frac{dP_{pc}}{dt} = \Gamma_{se}(P_A - P_{pc}) - \Gamma_{pc}P_{pc} - d_{pc}(P_{pc} - P_{tc}) \quad (4.3a)$$

$$\frac{dP_{tc}}{dt} = -\Gamma_{tc}P_{tc} + d_{tc}(P_{pc} - P_{tc}) \quad (4.3b)$$

where $P_{pc}(P_{tc})$ is the ${}^3\text{He}$ polarization in the PC (TC); γ_{se} is the spin-exchange rate in the PC; $\Gamma_{pc}(\Gamma_{tc})$ is the relaxation rate of ${}^3\text{He}$ polarization in PC (TC) that corresponds to Γ is a single-chambered cell, and $d_{pc}(d_{tc})$ is the probability for a nucleus to leave

the PC (TC) and enter the TC (PC). The transfer rates d_{pc} and d_{tc} are related by:

$$f_{pc}d_{pc} = f_{tc}d_{tc} \quad (4.4)$$

where $f_{pc}(f_{tc})$ is the fraction of atoms in the PC (TC). The solutions to Eq.4.3 are

$$P_{pc}(t) = C_{pc}e^{-\Gamma_f t} + (P_{pc}^0 - P_{pc}^\infty - C_{pc})e^{-\Gamma_s t} + P_{pc}^\infty \quad (4.5a)$$

$$P_{tc}(t) = C_{tc}e^{-\Gamma_f t} + (P_{tc}^0 - P_{tc}^\infty - C_{tc})e^{-\Gamma_s t} + P_{tc}^\infty \quad (4.5b)$$

where $P_{pc}^0(P_{tc}^0)$ is the initial polarization in the pumping (target) chamber and $P_{pc}^\infty(P_{tc}^\infty)$ is the saturation polarization in the pumping (target) chamber. The “slow” time constant Γ_s is mostly determined by the volume averaged spin-relaxation rate, which is given by

$$\Gamma_s = \langle \gamma_{se} \rangle (1 + X) + \langle \Gamma \rangle - \delta\Gamma \quad (4.6)$$

where $\langle \gamma_{se} \rangle = f_{pc}\gamma_{se}$ is the cell averaged spin-exchange rate, and $\langle \Gamma \rangle$ is the cell averaged spin relaxation rate due to mechanisms other than those parameterized by γ_{se} and X and is given by $\langle \Gamma \rangle = f_{pc}\Gamma_{pc} + f_{tc}\Gamma_{tc}$. The time independent quantities $\delta\Gamma$, Γ_f , C_{pc} and C_{tc} are functions of geometry, the various rates and initial conditions, which were discussed in Ref. [19]. The quantity $\delta\Gamma$ contains corrections due to the finite speed at which polarization moves between the two chambers. The size of $\delta\Gamma$ is usually no more than 10% of the size of Γ_s in our studies, and never more than 15%.

Again, the name 5-parameter fit comes from the fact that there are 5 parameters in each of the two equations. It’s interesting to note the time evolution of ${}^3\text{He}$ polarization for double-chambered cells has a new time constant: the ”fast” time constant Γ_f that is dominated by the diffusion rates d_{pc} and d_{tc} when diffusion is relatively fast.

In the fast-transfer limit, double-chambered solution reduces to single-chambered solution.

The other interesting point is the relation between the saturation polarization in PC and TC

$$P_{tc}^{\infty} = \frac{P_{pc}^{\infty}}{1 + \frac{\Gamma_{tc}}{d_{tc}}} \quad (4.7)$$

In the fast-transfer limit where $d_{tc} \gg \Gamma_{tc}$, $P_{tc}^{\infty} = P_{pc}^{\infty}$. With a convection style target cell where we can increase the parameter d_{tc} significantly, we can greatly reduce the polarization gradient.

4.2.1.3 Initial Spinup

As shown in Fig.4.4, the early-time behaviors of a spinup starting with zero polarization are quite different for the pumping chamber and the target chamber. The initial behavior in the pumping chamber is almost linear whereas the behavior in the target chamber is initially curved. By performing a Taylor expansion on Eq. 4.5 we obtain the early-time behaviors for both chambers [19]:

$$P_{pc}(t) = \gamma_{se}P_A t - \frac{1}{2}\gamma_{se}P_A(\gamma_{se} + \Gamma_{pc} + d_{pc})t^2 \quad (4.8a)$$

$$P_{tc}(t) = \frac{1}{2}\gamma_{se}P_A d_{tc}t^2 \quad (4.8b)$$

where γ_{se} is the spin-exchange rate in the pumping chamber and P_A is the alkali polarization. The dominant term in $P_{pc}(t)$ is the linear term while the shape of $P_{tc}(t)$ is quadratic.

The slope of the linear shape of initial spinup of the pumping chamber gives access to the product $P_A\gamma_{se}$ and fitting the initial spinup of the target chamber to a quadratic

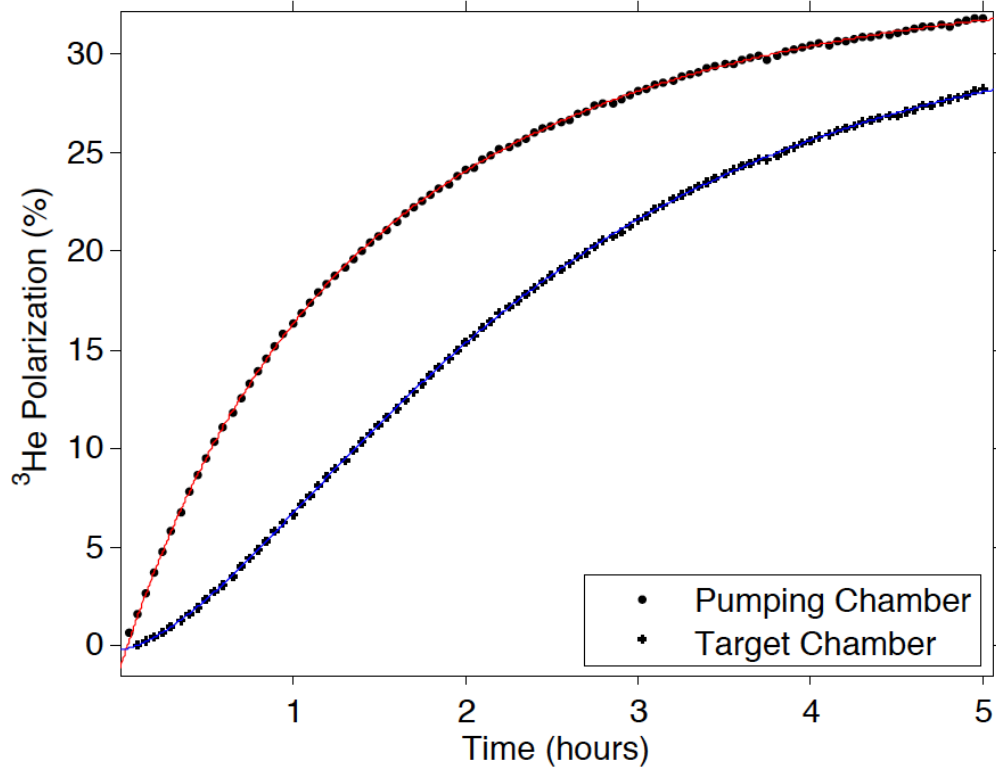


Figure 4.4: ${}^3\text{He}$ polarization as a function of time for both the pumping chamber and the target chamber. The top curve is the pumping chamber and the bottom curve is the target chamber. Data was taken at a fast pace so there would be enough points to demonstrate the initial behavior.

function provides the product $\gamma_{se} P_A d_{tc}$. The alkali polarization P_A can be measured with a technique we refer to here as Faraday rotation, we then gain knowledge of the spin-exchange rate γ_{se} and the diffusion rate d_{tc} . The slope of the polarization buildup in the pumping chamber is often written as $m_{pc} = P_A \gamma_{se}$.

The spin relaxation rate is also of great importance for characterizing target cells. The relaxation rates in the pumping chamber and the target chamber are different due to geometric and other properties. The cell-average relaxation rate can then be

written as

$$\langle \Gamma \rangle = f_{pc}\Gamma_{pc} + f_{tc}\Gamma_{tc} \quad (4.9)$$

where f_{pc} (f_{tc}) is the fraction of atoms in PC (TC); Γ_{pc} (Γ_{tc}) is the average relaxation rate in PC (TC). When the cell is being optically pumped, the pumping chamber is heated with hot air to create alkali vapor while the target chamber remains at the room temperature. Difference in temperature further complicates differences in relaxation rates between the two chambers. However, when trying to measure the life time (the inverse of the relaxation rate) of the cell, we typically keep the entire cell at room temperature and perform a “spindown” measurement.

During a spindown, the cell starts with some polarization (normally as high as possible so we can obtain a more complete curve), and relaxes on its own while we take AFP measurements at a certain rate. Typically, the interval between measurements is anywhere between 30 mins and 2 hrs, depending on the lifetime of the cell. The rule of thumb is to take AFP frequently enough so the spindown curve has sufficient data points while not too often so the polarization relaxes too fast due to AFP losses. Ideally, the ${}^3\text{He}$ polarization relaxation can be described by

$$P(t) = P_0 e^{-t/\tau_{true}} \quad (4.10)$$

The true lifetime τ_{true} of the cell without relaxation due to AFP loss can be measured with two methods: the first is to take 5 AFP measurements consecutively with very short interval (normally around 3 minutes), the second is to perform several spindown measurements, each with a different interval.

In the first method, because the lifetime of the cell is much longer than 3 minutes, we can safely attribute all losses to AFP measurements and extract the loss due to a

single AFP $loss_{afp}$. The data values can then be corrected with the equation

$$S_i^{corrected} = S_i^{raw} / (1 - loss_{afp})^{i-1} \quad (4.11)$$

where $S_i^{corrected}$ is the corrected signal, S_i^{raw} is the raw signal, i represents it is the i th measurement in the spindown, $loss_{afp}$ is the loss due to a single measurement. Fitting the corrected values to Eq. 4.10 gives the true lifetime τ_{true} .

A simple example for the second method would be to perform one spindown with one-hour interval and another spindown with two-hour interval, the relaxation rates in these two spindowns are

$$\frac{1}{\tau_{1hr}} = \frac{1}{\tau_{true}} + \Gamma_{AFP_1hr} \quad (4.12a)$$

$$\frac{1}{\tau_{2hr}} = \frac{1}{\tau_{true}} + \Gamma_{AFP_2hr} \quad (4.12b)$$

$$\Gamma_{AFP_1hr} = 2 \times \Gamma_{AFP_2hr} \quad (4.12c)$$

where τ_{1hr} and τ_{2hr} are the lifetimes measured with taking AFP every 1 hour and every 2 hours, τ_{true} is the true lifetime of the cell without interference from measurements, Γ_{AFP_1hr} (Γ_{AFP_2hr}) is the relaxation rate due to taking measurements every 1hr (2hr). We can then solve for τ_{true} .

4.3 The K- 3 He Spin-Exchange Rate Constant

As mentioned in the initial spinup section, the polarization in the pumping chamber at the beginning of the accumulation process, if started in the completely unpolarized

state, can be described by

$$P_{pc} = \gamma_{se}\langle P_A \rangle(t - t_0) + b(t - t_0)^2 = m_{pc}t + bt^2 + c \quad (4.13)$$

where m_{pc} is the slope of the linear term. Typically, in the first 20 to 30 minutes, the spinup behaves so linearly that the effect of quadratic term is negligible.

During these initial spinups, an AFP measurement was taken every 3 minutes, and the AFP losses were carefully accounted for when calculating m_{pc} . The ${}^3\text{He}$ spins were flipped to the opposite direction during every AFP measurement for a short period of time while still receiving polarization in the original direction. Care was taken to account for the time during which spins were “anti-aligned”. We refer to the the slope collected from initial spinups as m_{pc}^s , to differentiate it from the same quantity measured with the Faraday rotation technique. I will briefly introduce Faraday rotation, the details of which were described thoroughly by Dolph. [3].

The Faraday rotation technique, as the name implies, is the observation of Faraday rotation using a linearly polarized probe laser. Faraday rotation refers to the change in the orientation of the polarization axis when linearly polarized light passes through a polarized alkali vapor. It is sufficient to consider only the alkali-metal atom’s D₁ and D₂ lines for our cases. The Faraday rotation angle ϕ_r is given by:

$$\phi_r = - \left(\frac{e^2}{12mc\epsilon_0} \right) P[K]l\omega([f_1^{Rb} - f_2^{Rb}]/D + [f_1^K - f_2^K]) \quad (4.14)$$

where r_e is the classical electron radius, c is the speed of light in vacuum, l is the path length through the vapor, D is the ratio of the K to Rb vapor number densities and

f_1, f_2 are given by

$$f_1 = \frac{1}{\omega_{D2}} \frac{\Delta_{D2}}{\Delta_{D2}^2 + \frac{\gamma_{D2}^2}{4}} \quad (4.15a)$$

$$f_2 = \frac{1}{\omega_{D1}} \frac{\Delta_{D1}}{\Delta_{D1}^2 + \frac{\gamma_{D1}^2}{4}} \quad (4.15b)$$

During a Faraday rotation measurement, ϕ_r was measured at several probe wavelengths and fit to the Eq. 4.14. We were able to obtain the quantities $P_A[Rb]l$ and D from the fit. However, in order to extract [Rb], it is necessary to measure the path length l and P_A . Alkali polarization was measured by measuring the Faraday rotation angle while inducing Zeeman transitions. It is worth noting this only gave line-averaged polarization as only information on the path of the probe laser was collected. The volume-averaged alkali polarization can be obtained by applying small corrections from our simulation.

With knowledge of alkali densities, the spin-exchange rate is:

$$\gamma_{se} = k_{se}^{Rb}[Rb] + k_{se}^K[K] \quad (4.16)$$

where $k_{se}^{Rb}(k_{se}^K)$ is the spin-exchange rate constant between ${}^3\text{He}$ and Rb (K). The m_{pc} calculated with this manner is referred to as “ m_{pc}^F ”, since this quantity was computed with Faraday rotation data.

The values of m_{pc}^F and m_{pc}^s are expected to be the same if they are measured in the same cell under identical conditions. The spin-exchange rate constants k_{se}^{Rb} and k_{se}^K are required to calculate m_{pc}^F . k_{se}^{Rb} has been measured and reported in literature multiple times. k_{se}^K on the other hand, is not as well-known. The value of k_{se}^{Rb} we used was the combined result from Baranga *et al.* [37] and from Chann *et al.* [53]:

$$k_{se}^{Rb} = (6.79 \pm 0.14) \times 10^{-20} \text{cm}^3/\text{s} \quad (4.17)$$

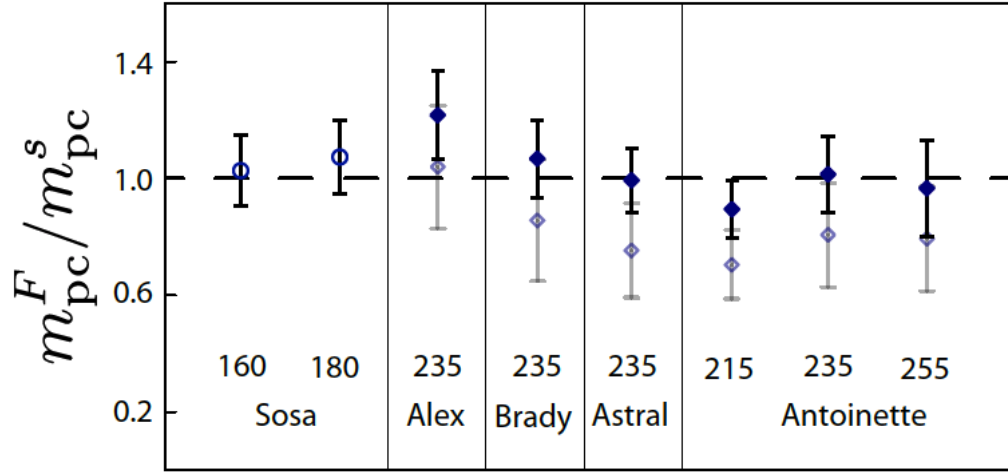


Figure 4.5: Plotted is the ratio m_{pc}^F/m_{pc}^s for eight separate measurements. The numbers above the cell names are the oven set temperatures at which the measurements were made. Difference between open and closed points is discussed in the text.

The ratio of m_{pc}^F/m_{pc}^s is plotted in Fig. 4.5. The two measurements with the Rb only cell Sosa are shown with solid circles. To calculate the ratio for the rest of the measurements, a value for k_{se}^K is needed. Babcock reported this number to be $(5.5 \pm 0.4) \times 10^{-20} \text{ cm}^3/\text{s}$ in his thesis [54]. However, the resulting ratio was significantly lower than unity in all but one of the 6 measurements, as shown with open diamonds in the figure. We fit our data so the ratio m_{pc}^F/m_{pc}^s is equal to one while treating k_{se}^K as a free parameter. The results are shown with solid diamonds. Our fitted k_{se}^K value is

$$k_{se}^K = (7.46 \pm 0.62) \times 10^{-20} \text{ cm}^3/\text{s} \quad (4.18)$$

The reason why our result is significantly higher than Babcock's is unclear. One possibility may be temperature dependence as the temperatures under which our measurements were made were higher than that of Babcock's. We decided to use our own result of k_{se}^K to measure the X factor because it was measured under similar

operating conditions to our other measurements, and our own result improves the internal consistency of our data.

4.4 The X Factor

Prior to the introduction of the X factor, it was not understood why ${}^3\text{He}$ polarization would not approach unity with sufficiently high alkali-vapor densities and laser power such that P_A was nearly 100% and $\gamma_{se} \gg \langle \Gamma \rangle$. However, the ${}^3\text{He}$ polarization during our studies had shown differently as also shown by Babcock *et al.*. The fact that it was never close to 100% even with high laser power and alkali densities could be explained by the X factor.

As mentioned earlier, Babcock *et al.* reported a previously unrecognized spin relaxation mechanism in his paper [17]. This mechanism appears to be roughly proportional to the spin-exchange rate γ_{se} , so it cannot be overcome by increasing the alkali density or laser power. The maximal achievable ${}^3\text{He}$ polarization can be expressed as

$$\lim_{\gamma_{se} \rightarrow \infty} = \lim_{\gamma_{se} \rightarrow \infty} \frac{\langle P_A \rangle \langle \gamma_{se} \rangle}{\langle \gamma_{se} \rangle (1 + X) + \langle \Gamma \rangle} = \frac{P_A}{1 + X} \quad (4.19)$$

The combination of alkali-hybrid and narrowband laser has made it much easier to achieve higher spin-exchange rates γ_{se} . Thus the X factor is playing an increasingly significant role in limiting the equilibrium ${}^3\text{He}$ polarization, which makes it an important subject for study.

Unlike many other properties of the cell that can be measured directly, the X factor is a derived quantity. While characterizing our target cells, we collected enough data to determine the X factor in several different ways. We were able to compare

EXP	Cell	Lasers	I_0 W/cm ²	T_{pc}^{set} °C	P_{He}^{∞}	Γ_s^{-1} hrs	$\langle \Gamma \rangle^{-1}$ hrs	$\langle P_A \rangle$	P_A^A	D_{fr}	D_{pb}	[Rb] _{fr} 10 ¹⁴ /cm ³	ΔT_{Rb} °C	ΔT_{He} °C	X
saGDH	Proteus	3B	3.8	180	0.46	27	74	-	-	0	0	-	-	-	-
	Priapus	3B	3.8	180	0.44	21	56	-	-	0	0	-	-	-	-
	Penelope	3B	3.8	180	0.39	18	46	-	-	0	0	-	-	-	-
	Powell	3B	3.8	180	0.38	13	25	-	-	0	0	-	-	-	-
	Frasch	3B	3.8	180	0.33	13	33	-	-	0	0	-	-	-	-
GEN	Al	2.5B	3.2	235	0.53(03)	7.86(05)	27.42(1.37)	-	-	-	4.53(25)	-	-	-	-
		5B	6.1	235	0.54(03)	6.73(18)	27.42(1.37)	-	-	-	4.53(25)	-	-	-	-
	Barbara	2.5B	1.6	235	0.37(02)	5.5(08)	42.95(2.15)	-	-	-	4.80(25)	-	-	-	-
		5B	3.1	235	0.57(03)	4.76(63)	42.95(2.15)	-	-	-	4.80(25)	-	-	-	-
	Gloria	3B	1.7	235	0.60(03)	6.13(04)	38.29(1.91)	-	-	-	7.20(40)	-	-	-	-
	Anna	1B	0.6	235	0.33(02)	5.60(34)	11.38(57)	-	-	-	9.64(57)	-	-	-	-
		1.5B	1.0	235	0.39(02)	5.37(08)	11.38(57)	-	-	-	9.64(57)	-	-	-	-
	Dexter	1.5B	1.5	235	0.47(02)	7.58(17)	18.45(92)	-	-	-	-	-	-	-	-
		5B	6.1	235	0.49(02)	6.63(12)	18.45(92)	-	-	-	-	-	-	-	-
	Edna	3B	2.4	235	0.56(03)	5.71(02)	27.42(1.37)	-	-	-	3.63(20)	-	-	-	-
		3B	1.0	235	0.43(02)	6.16(03)	35.24(1.76)	-	-	-	20(1.3)	-	-	-	-
	Dolly	1N1B	1.4	235	0.62(03)	5.79(07)	35.24(1.76)	-	-	-	20(1.3)	-	17(10)	-	-
	Simone	2N1B	3.8	215	0.31(01)	14.08(06)	22.87(1.14)	0.947(020)	0.91(05)	10.66(54)	8.89(45)	0.20(02)	-7(3)	-	-0.04(12)*
		2N1B	3.8	240	0.48(02)	6.89(20)	22.87(1.14)	-	-	-	9.76(49)	-	-	-	-
		2N1B	3.8	255	0.58(02)	6.45(10)	22.98(1.14)	0.929(023)	0.92(05)	12.48(83)	10.3(52)	0.90(09)	-4(5)	-	0.11(06)*
Transversity	Sosa	2N1B	1.9	160	0.57(02)	16.69(09)	73.68(3.68)	0.966(020)	1.00(03)	0	0	1.97(13)	4(1)	30(7)	0.24(06)†
		2N1B	1.9	170	0.61(03)	11.67(04)	73.68(3.68)	0.964(020)	0.98(03)	0	0	3.00(33)	3(3)	38(14)	0.27(06)*
		2N1B	1.9	180	0.55(02)	8.79(09)	73.68(3.68)	0.954(022)	0.97(03)	0	0	4.30(27)	1(2)	47(7)	0.43(06)†
		2N1B	1.9	190	0.40(02)	6.39(22)	73.68(3.68)	0.854(075)	0.82(03)	0	0	5.69(63)	-2(3)	48(20)	0.58(12)*
		2N1B	1.9	200	0.26(01)	5.04(17)	73.68(3.68)	-	-	0	0	-	43(18)	-	-
	Boris	3B	1.8	235	0.42(02)	6.25(04)	23.74(1.19)	0.871(050)	0.79(07)	1.96(18)	2.45(23)	2.19(34)	-8(7)	-	0.26(10)*
	Samantha	3B	1.8	235	0.50(02)	6.30(13)	36.51(1.83)	-	-	-	4.34(23)	-	-	-	-
d ₂ ⁿ		3N	2.6	235	0.68(03)	4.62(03)	22.13(1.11)	0.956(020)	0.99(03)	4.37(10)	4.34(23)	1.80(10)	7(2)	21(10)	0.12(05)*
	Alex	2N1B	2.6	235	0.59(03)	4.81(02)	32.96(1.65)	0.942(042)	0.99(03)	1.37(08)	1.19(07)	4.08(36)	0(4)	42(10)	0.34(06)†
	Moss	1N1B	1.8	235	0.62(03)	5.35(04)	33.00(1.65)	-	0.95(09)	-	2.40(13)	-	-	29(8)	-
	Tigger	1N1B	1.8	235	0.51(02)	4.89(05)	12.62(63)	-	0.95(09)	-	-	-	-	23(9)	-
	Astral	2N1B	2.6	235	0.69(03)	6.57(12)	48.90(2.45)	0.954(020)	0.99(03)	7.09(55)	6.21(56)	0.97(09)	3(5)	25(4)	0.17(05)†
	Stephanie	3N	2.6	235	0.63(03)	4.55(09)	48.35(2.42)	0.929(114)	0.99(03)	1.39(11)	1.50(10)	5.08(58)	7(5)	54(6)	0.31(08)*
	Brady	1N	0.9	235	0.62(03)	4.82(1.08)	33.50(1.68)	-	0.95(03)	-	2.36(24)	-	-	14(9)	-
		2N	1.8	235	0.68(03)	5.52(70)	33.50(1.68)	-	0.99(03)	-	2.36(24)	-	-	25(8)	-
		3N	2.6	235	0.70(03)	5.30(01)	33.50(1.68)	0.956(021)	0.99(03)	2.60(20)	2.36(24)	2.86(30)	6(5)	39(9)	0.14(05)†
	Maureen	3N	2.6	235	0.66(03)	5.42(12)	29.21(1.46)	-	0.97(09)	-	4.42(55)	-	-	32(12)	-
Antoinette	3N	1.7	215	0.49(02)	6.63(37)	20.93(1.05)	0.958(020)	0.99(03)	2.85(13)	-	0.96(07)	0(3)	16(8)	0.28(08)†	
		3N	1.7	235	0.61(03)	4.18(10)	20.93(1.05)	0.936(043)	0.99(03)	3.32(27)	-	1.83(20)	0(5)	20(10)	0.24(07)†
		3N	1.7	255	0.41(02)	2.66(11)	20.93(1.05)	0.776(099)	0.93(10)	3.57(23)	-	2.88(39)	-5(6)	33(9)	0.55(13)†

Table 4.2: Cell Performance for three sets of experiments: saGDH (top), GEN (middle), and Transversity & d_2^n (bottom). Within each experiment grouping, data is grouped by type of laser used (B = Broadband, N = Narrowband). I_0 is the nominal incident laser intensity at the center of the pumping chamber. T_{pc}^{set} is the oven set temperature. P_{pc}^{∞} is the equilibrium polarization in the pumping chamber and Γ_s is the slow time constant extracted from the five parameter fit to the polarization build up curve. Γ_c is the cell-averaged room temperature spin relaxation rate. $\langle P_A \rangle / P_A^l$ is the volume averaged to line averaged alkali polarizaiton ratio determined from the optical pumping simulation. P_A^l is the measured line averaged alkali polarization. D_{fr} & D_{pb} are the K to Rb density ratios determined from Faraday rotation and pressure broadening measurements. [Rb]_{fr} is the Rb number density measured from Faraday rotation. ΔT_{He} is the temperature of Rb inferred from the number density relative to the oven set temperature. ΔT_{He} is the temperature of ^3He inferred from temperature tests relative to the oven set temperature. X is the best combined value for the X-factor. * indicates X was measured using only spinup, alkali polarization, and Faraday rotation data. † indicates X was also measured using the early-time behavior of the spinup.

these values and combine them into weighted averages. We also looked at possible temperature dependence using X values obtained at different temperatures. The data used are presented in Table 4.2.

We calculated the X factors in several different ways, all of which required knowledge of the cell-averaged spin relaxation rate $\langle \Gamma \rangle$ at operating temperatures. However, the spindown measurements we performed only gave us the spin relaxation rate $\langle \Gamma \rangle_c$ at room temperature. We made the assumption that the difference between $\langle \Gamma \rangle$ and $\langle \Gamma \rangle_c$ is purely due to the change of cell-averaged ^3He - ^3He dipolar spin relaxation rate,

and the relaxation rate due to collisions with the walls is the same for the two chambers and does not change at different temperature. The correction to the relaxation rate is given by

$$\langle \Gamma \rangle = \langle \Gamma \rangle_c - [n_0 - f_{pc}n_{pc}/f^d(t_{pc}) - f_{tc}n_{tc}/f^d(t_{tc})]/\tau^d \quad (4.20)$$

where n_0 is the ${}^3\text{He}$ fill density, $n_{pc(tc)}$ is the ${}^3\text{He}$ density in the pumping (target) chamber, $f_{pc(tc)}$ is the fraction of ${}^3\text{He}$ atoms in the pumping (target) chamber, $t_{pc} = T_{pc}/(296.15K)$, $t_{tc} = (313.15K)/(296.15K)$, $\tau^d = 744\text{hrs}\cdot\text{amg}$ [55], $f^d(t)$ is a function that parameterizes the temperature dependence of the dipolar relaxation [56]. $\langle \Gamma \rangle$ is typically only a few percent less than $\langle \Gamma \rangle_c$ for us. In addition, whenever the quantity $(\Gamma_s - \langle \Gamma \rangle)$ is used, a small correction to account for the AFP losses is added.

Our methods of extracting X require using some form of the equation

$$\langle \gamma_{se} \rangle = \frac{\Gamma_s - \langle \Gamma \rangle + \delta\Gamma}{1 + X} \quad (4.21)$$

One method Babcock used and we applied on a small number of cells is called “hot relaxation method” [17]. We plot $\langle \gamma_{se} \rangle$ as a function of $\Gamma_s - \langle \Gamma \rangle + \delta\Gamma$, the slope of a linear fit to the data is expected to be $1/(1+X)$. Three such fits are shown in Fig. 4.6, all of which were constrained to go through the origin. Two of the three X values were significantly different than zero. The X factor of Simone is too close to zero when the error is taken into account for us to make a strong statement.

The small correction $\delta\Gamma$ came into play because of the double-chambered design. It can be approximated by

$$\delta\Gamma \approx f_{pc}f_{tc}(d_{pc} + d_{tc})u^2 + \text{higher order terms} \quad (4.22)$$

where $d_{pc(tc)}$ is the probability per unit time that a ${}^3\text{He}$ atom will exit the pumping (target) chamber. The quantity u is

$$u = \frac{\gamma_{se}(1 + X) + \Gamma_{pc} - \Gamma_{tc}}{d_{pc} + d_{tc}} \quad (4.23)$$

where $\Gamma_{pc(tc)}$ is the spin relaxation rate in the pumping (target) chamber. What makes the determination of X tricky is that we need to know its value before we can calculate u which is a prerequisite for X . However, because $\delta\Gamma$ is such a small correction typically being 10% or less of the size of Γ_s , we solve this problem in an iterative manner. X is initially assumed to be 0 and plugged into Eq. 4.23, which in the end lead to a different value of X that is closer to its real value. After iterating this process a few times, X quickly converges to a stable value.

However, the hot relaxation method assumes the temperature dependence of the X factor is identical to the temperature dependence of γ_{se} by combining data taken at different temperature into one value of X . It is also time consuming to perform the measurements shown in Fig. 4.6. For these two reasons, the hot relaxation method was only applied to a small number of cells.

In order to measure the X factor at a single temperature and explore its possible temperature dependence, we used 4 four other methods to determine the value of X factor. All but the second method described below are based on the “polarization method” from Ref. [17]. And the second method is basically a single point measurement of the hot relaxation method described above.

We label the results from the four single-temperature methods as X_1 , X_2 , X_3 and X_4 respectively. The most straightforward method requires measurements of $\langle P_A \rangle$,

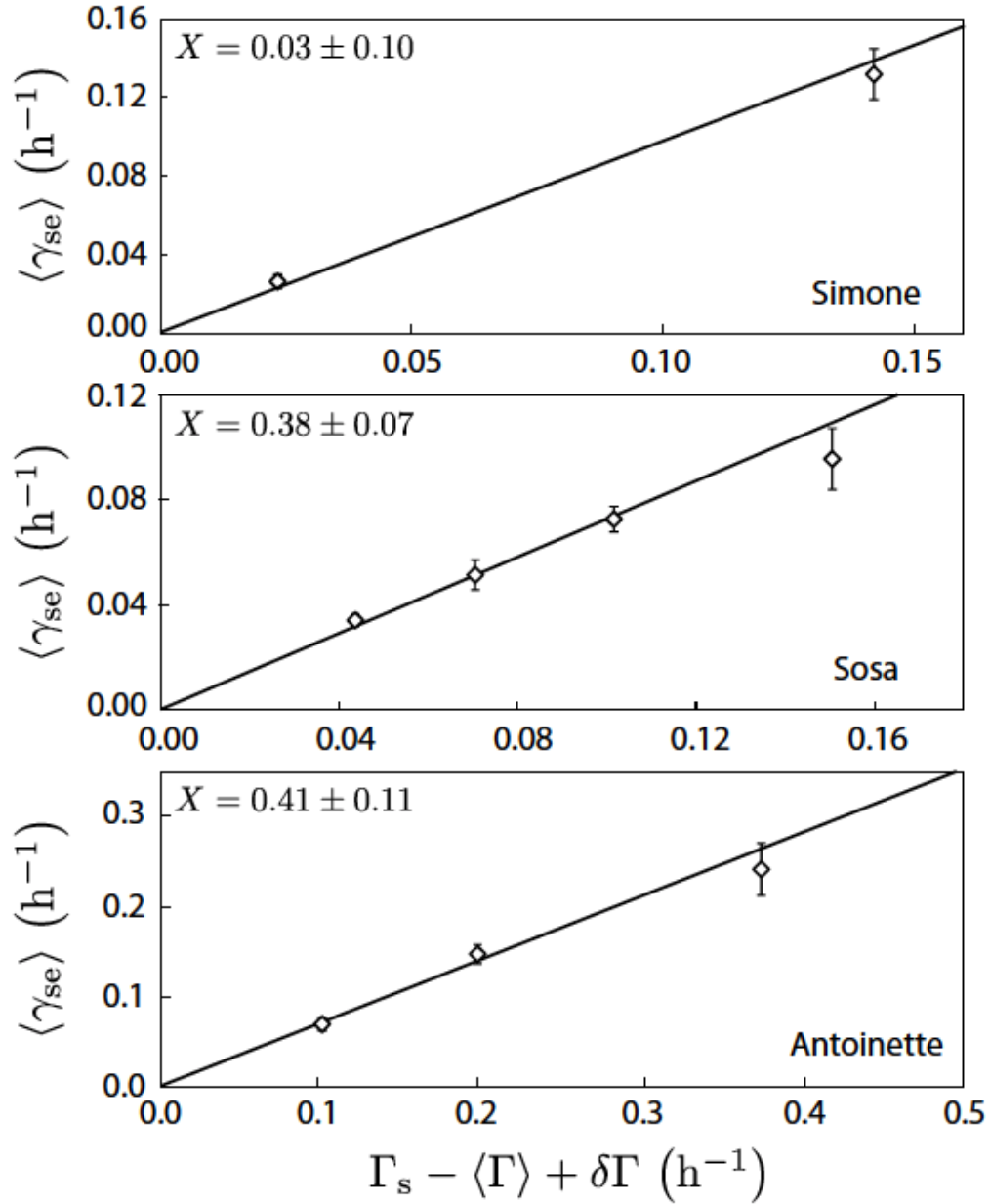


Figure 4.6: The cell-averaged spin-exchange rate $\langle \gamma_{se} \rangle$ is calculated using data from Faraday rotation and the spin-exchange constants k_{se}^{Rb} and k_{se}^K . The three linear fits shown here are constrained to go through zero. The errors quoted in values of X factor include the uncertainty in our determination of k_{se}^K .

P_{pc}^∞ and Γ_s . The equilibrium ${}^3\text{He}$ polarization can be rewritten as

$$P_{pc}^\infty = \frac{\langle P_A \rangle \langle \gamma_{se} \rangle}{\Gamma_s + \delta\Gamma - \delta\Gamma'} \quad (4.24)$$

where $\delta\Gamma' = f_{tc}\Gamma_{tc}^2/(\Gamma_{tc} + d_{tc})$. Substituting Eq. 4.21 into Eq. 4.24, we find

$$X_1 = \frac{\langle P_A \rangle}{P_{pc}^\infty} \left(\frac{\Gamma_s - \langle \Gamma \rangle + \delta\Gamma}{\Gamma_s + \delta\Gamma - \delta\Gamma'} \right) - 1 \quad (4.25)$$

Just as what we did for the hot relaxation method, here $\delta\Gamma$ is calculated in the same iterative manner. X is first taken as 0 and the iteration continued until X converged to a stable value.

For the second method, we first solve Eq. 4.21 for X :

$$X = \frac{\Gamma_s - \langle \Gamma \rangle + \delta\Gamma}{\langle \gamma_{se} \rangle} - 1 \quad (4.26)$$

then we substitute Eq. 4.16 into the equation above:

$$X_2 = \frac{\Gamma_s - \langle \Gamma \rangle + \delta\Gamma}{f_{pc}k_{se}^{Rb}[Rb](1 + D')} - 1 \quad (4.27)$$

where

$$D' = Dk_{se}^K/k_{se}^{Rb} \quad (4.28)$$

Again $\delta\Gamma$ is calculated iteratively. We chose to use our value of k_{se}^K for better consistency with the rest of our data.

The third method is very similar to the second, but we determine $\langle \gamma_{se} \rangle$ with data from initial spinups:

$$\langle \gamma_{se} \rangle = f_{pc}m_{pc}^s/\langle P_A \rangle \quad (4.29)$$

Substitute the above equation into Eq. 4.26, we get

$$X_3 = \langle P_A \rangle \frac{\Gamma_s - \langle \Gamma \rangle + \delta\Gamma}{f_{pc}m_{pc}^s} - 1 \quad (4.30)$$

Cell	T(°C)	X_1	X_2	X_3	X_4	X_{12}/X_{1234}
Simone	215	-0.02(12)	-0.10(14)	-	-	-0.04(12)
	255	0.13(08)	0.08(09)	-	-	0.11(06)
Sosa	160	0.22(07)	0.28(09)	0.32(15)	0.18(09)	0.24(06)†
	170	0.24(07)	0.37(15)	-	-	0.27(06)
	180	0.45(08)	0.40(09)	0.50(17)	0.45(09)	0.43(06)†
	190	0.59(16)	0.57(17)	-	-	0.58(12)
Boris	235	0.21(14)	0.31(14)	-	-	0.26(10)
Sam.	235	0.08(06)	0.22(09)	-	-	0.12(05)
Alex	235	0.34(09)	0.35(09)	0.63(20)	0.29(10)	0.34(06)†
Astral	235	0.15(07)	0.22(10)	0.20(14)	0.14(07)	0.17(05)†
Steph.	235	0.31(17)	0.31(10)	-	-	0.31(08)
Brady	235	0.13(07)	0.15(09)	0.23(14)	0.11(07)	0.14(05)†
Antoinette	215	0.27(09)	0.44(17)	0.30(19)	0.25(11)	0.28(08)†
	235	0.20(09)	0.34(12)	0.36(17)	0.15(09)	0.24(07)†
	255	0.55(26)	0.54(16)	0.50(30)	0.56(26)	0.55(13)†

Table 4.3: Shown are the values of the X factor at the indicated over set temperatures. The last column is a weighted average of results from either the first two methods or all four methods. A † indicates combined values computed with all 4 methods.

Note the quantity k_{se}^K used for X_2 was obtained by fitting the ratio m_{pc}^F/m_{pc}^s to 1, thus for any hybrid cell, X_2 and X_3 are highly correlated. However, for pure Rb cell such as Sosa, these two methods are independent.

The difference between the fourth method and the first is that the fourth method treats $\langle \gamma_{se} \rangle$ as a known quantity and expresses Γ_s with it using Eq. 4.21, while the first method did it in the opposite way. The cell-averaged spin-exchange rate is evaluated with

$$\langle \gamma_{se} \rangle = f_{pc} m_{pc}^s / \langle P_A \rangle \quad (4.31)$$

Thus X_4 is

$$X_4 = \frac{P_A}{P_{pc}^\infty} - \frac{\langle P_A \rangle (\langle \Gamma \rangle - \delta \Gamma')}{f_{pc} m_{pc}^s} - 1 \quad (4.32)$$

The computed X factors are shown in Table 4.3. The different values of X are quite consistent with each other. It is worth noting that even though X_1 is completely independent of m_{pc} and k_{se}^K , it is still quite consistent with the rest of the X values. The last column in the table is a weighted average of either X_1 and X_2 (X_{12}) or all

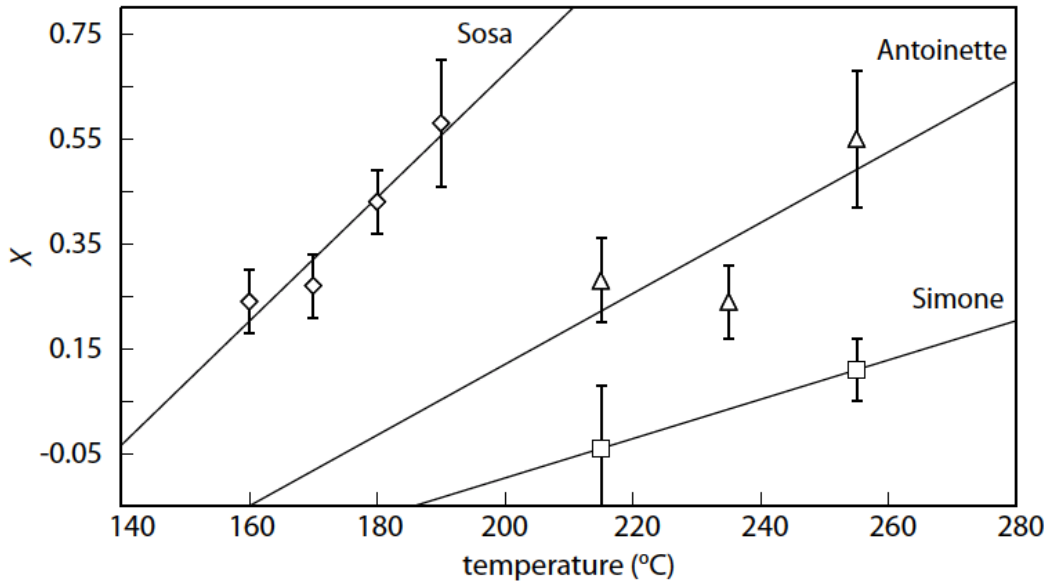


Figure 4.7: Shown are the combined values for X factor (either X_{12} or X_{1234} depending on the availability of data) versus temperature for the cell Sosa, Simone and Antoinette.

four X values (X_{1234}).

To the best of our knowledge, there has not been a dedicated study of the X factors and their temperature dependence, with a large number of cells using measurements of the alkali polarization since the original work of Babcock's *et al.* original work [17]. Our results thus represent independent evidence of the existence of a non-zero X factor. According to our study, the X factor limits ${}^3\text{He}$ polarization to 62-88% for the range of temperature we operate within.

Since we have evaluated X at multiple temperatures for Simone, Sosa and Antoinette, we can explore the temperature dependence of X factor. The combined value of X is plotted against temperature in Fig. 4.7 for the three cells. The figure seems to indicate a systematic variation with temperature.

If we assume a linear dependence of X with temperature, the fitted slope for Sosa with 4 points is $(0.012 \pm 0.002)/{}^\circ\text{C}$, which is six-sigma away from zero. The slope for

the three points of Antoinette is $(0.007 \pm 0.005)/^{\circ}\text{C}$, which is slightly above one sigma from zero. Simone has only two points available to us, the second point seems to be right around the edge of the error bar on the first point. Although we cannot make a strong statement, it seems likely that there is a trend here. We do not consider this result conclusive, but it still suggests the existence of temperature dependence of X.

We considered the possibility that the temperature dependence was introduced by our own value of the spin-exchange constant k_{se}^K . After considering both our value and that from Babcock, we found that the trend exists with both, but our value provides better self consistency. Another possibility is that the temperature dependence of k_{se}^K is the source of temperature dependence of X. However, if that is the case, we should be able to observe different behaviors in what the 4 different methods produced. From what is shown by Table 4.3, the different methods produced similar results within errors, thus k_{se}^K is not likely to be the cause of temperature dependence of X.

Another possibility was the temperature dependent contribution from anisotropic spin exchange [57]. However, even though calculations from Tscherbul *et al.* [58] indicate the anisotropic spin exchange contribution to the X factor has a temperature dependence, the contribution is very small in our operating temperature range.

We also considered whether other systematic effects could result in such temperature dependence. For example, the distribution of the gas between pumping chamber and target chamber changes at different temperatures. We then concluded that the uncertainties in the gas distribution had only negligible effects on the observed temperature dependence of X. After analyzing our data, we were unable to identify a systematic effect as a plausible explanation, our results suggest further study of X and its temperature dependence may be of great importance.

Chapter 5

Development of Cells with Metal End Windows

5.1 Overview

Electron scattering experiments at JLab have traditionally used ${}^3\text{He}$ targets made of glass due to the compatibility with spin-exchange optical pumping, the capability to be shaped into desired geometries through glass blowing, and the excellent nuclear spin relaxation properties.

During 12 GeV running at JLab, polarized ${}^3\text{He}$ experiments are planned that will be run at much higher luminosities than has previously been the case. The maximum current used before the upgrade was $15\mu\text{A}$, while future ${}^3\text{He}$ experiments will be run at up to $60\mu\text{A}$. We believe an all-glass target cell might survive long enough for an experiment with $30\mu\text{A}$, but it is unlikely to survive at $60\mu\text{A}$. A natural solution would be to replace the thin glass window (where electron beam enters and exits the target cell) with a material with higher strength and good spin-relaxation properties.

Deninger *et al.* [59] from the Mainz group showed relaxation time of various metal

surfaces: Mg (6 h), Al (6 h), Zn(12 h) etc. Gold caught our attention in particular, because it has a relatively long relaxation time of 20 h. This relaxation time was measured with the entire glass surface coated with gold, thus the area of gold surface was much larger than what will be needed for target windows. In addition, while the coating process made sure of the chemical purity, it did not make effort in ensuring the microscopic smoothness, which means the surface area was further increased. Therefore one would expect a even longer relaxation time with a smooth and smaller metallic surface. In light of this, our group has tested 19 cells with various geometries and materials, most of which incorporated an OFHC (oxygen-free high thermal conductivity) copper tube with gold coating. Towards the end of my work, we achieved a 15.6 h relaxation time with a Pyrex cell that had a 5" long by 1" gold coated copper tube attached horizontally. By extrapolating the relaxation rate due to gold surface from this result, we believe the relaxation rate introduced by small metal windows in a target cell will be less than $1/93.06 \text{ hr}^{-1}$. To the best of our knowledge, our group was the first to have proved the potential of incorporating metal to target cells in the presence of alkali vapor.

5.2 Wall Relaxation of ^3He

5.2.1 Relaxation on Glass Surfaces

Fitzsimmons and Walters have studied surface-induced spin-lattice relaxation times as a function of temperature for ^3He gas in glass containers [60]. There are mainly two categories of wall relaxation mechanisms: ^3He adsorption onto the glass surface and the permeation of ^3He into glass. The latter mechanism can be greatly reduced by using impermeable aluminosilicate glass such as GE180.

Timsit and Daniels [61] then studied surface relaxation on a great number of common materials and presented a phenomenological model to describe the relaxation processes. For permeable glasses, the relaxation is determined by absorption of gas in the surface layer of the glass and by the paramagnetic-impurity contents of the glass. The surface adsorption of ${}^3\text{He}$ near paramagnetic sites on the walls also contributes to the nuclear relaxation. Relaxation due to absorption for permeable glasses will be discussed first below.

The diffusion coefficient D of a noble gas in a glass can be calculated with the following equation:

$$D = D_0 e^{-E_{diff}/kT} \quad (5.1)$$

where E_{diff} is the activation energy for diffusion and D_0 is a constant. The diffusion coefficient can also be expressed with the mean diffusion jump distance of ${}^3\text{He}$ atom in the glass $\langle \Delta r \rangle$ as:

$$D = \frac{\langle \Delta r \rangle^2}{6\tau} \quad (5.2)$$

with τ being the mean time between diffusion jumps

$$\tau = \tau_0 e^{E_{diff}/kT} \quad (5.3)$$

where $\tau_0 = \langle \Delta r \rangle^2 / 6D_0$.

Let n_g be the number of atoms dissolved in the surface layer of mean thickness $\langle \Delta r \rangle$, the rate at which ${}^3\text{He}$ atoms enter and leave the surface layer of the glass is then $n_g/6\tau$ [61]. n_g should be proportional to the solubility S of ${}^3\text{He}$ in the glass, so for a spherical cell

$$n_g = \frac{6NkT\langle \Delta r \rangle S}{d} \quad (5.4)$$

where d is the diameter of the cell, N is the total number of free ${}^3\text{He}$ atoms.

For most trapping sites in the glass, the intrinsic relaxation time T_i is longer than τ which is the time it takes for ${}^3\text{He}$ to leave the $\langle \Delta r \rangle$ layer. However, T_i for a paramagnetic site is shorter than τ , thus will completely relax the nuclear spin of a ${}^3\text{He}$ atom. The relaxation time of ${}^3\text{He}$ in permeable glass cells is controlled by absorption of the atoms in the surface layer at paramagnetic sites. The average nuclear relaxation time of a ${}^3\text{He}$ trapped in the glass close to a Fe^{3+} ion (one common type of paramagnetic impurity in glass) is [41]:

$$\frac{1}{T_i} \approx \frac{3}{5} \frac{\mu_{He}^2 \mu_B^2 g^2}{\hbar^2 b^6} \frac{T_{Fe}}{1 + \omega_0^2 T_{Fe}^2} \quad (5.5)$$

where μ_{He} is the nuclear dipole moment of ${}^3\text{He}$, μ_B is the Bohr magneton, g is the g factor of the Fe^{3+} (${}^6S_{5/2}$) ion, b is the distance between the spins, and T_{Fe} is the relaxation time of a Fe^{3+} ion in glass. Taking b as 1 \AA and g as 5.9 [62], T_i is $\sim 10^{-11} \text{ s}$, which is 10 times smaller than the shortest τ .

Even a small amount of paramagnetic impurities among the trapping sites in the glass could potentially provide dominating contribution on the ${}^3\text{He}$ spin relaxation. Assuming during the random walk of ${}^3\text{He}$ atom in the glass, there are on average β atoms in its vicinity, and atom fraction of paramagnetic impurities is $N_{impurity}$, the relaxation time due to absorption is if $T_i \ll \tau$:

$$T_{ab} = \frac{6N\tau}{\beta N_{impurity} n_g} \quad (5.6)$$

For impermeable glasses such as GE180, the relaxation rate due to absorption into the glass walls is typically negligible. The dominating relaxation mechanism here is adsorption of ${}^3\text{He}$ on the glass wall in vicinity of a paramagnetic site.

The sticking time τ_s is given by Frenkel's Law [63]:

$$\tau_s = \tau_{s0} e^{E_{ad}/kT} \quad (5.7)$$

where τ_{s0} is on the order of 10^{-13} s for most solid surfaces [63], E_{ad} is the adsorption energy. At room temperature, we have $\tau_s \sim \tau_{s0} \sim 10^{-13}$ s. The number of atoms hitting the wall per unit time and unit area is given by $\frac{1}{4}n\bar{v}$, where n is the number density of ^3He gas and \bar{v} is the mean velocity. For a spherical cell with diameter d , the number of atoms adsorbed on the wall is

$$n'_g = \frac{3N\bar{v}\tau_s}{2d} \quad (5.8)$$

The intrinsic relaxation time T'_i of a ^3He near a paramagnetic site on the wall is much longer than the sticking time τ_s . The average number of collisions required to depolarize ^3He is T'_i/τ_s , thus the relaxation time due to adsorption is

$$T_{ad} = \frac{NT'_i}{N_{impurity}n'_g} \quad (5.9)$$

The total relaxation rate is the sum of that due to adsorption and absorption (for permeable glasses):

$$\frac{1}{T_{wall}} = \frac{1}{T_{ad}} + \frac{1}{T_{ab}} \quad (5.10)$$

Substitute Eq. 5.3, 5.4 into Eq. 5.6 and Eq. 5.7, 5.8 into Eq. 5.9, the wall relaxation rate can be written as

$$\begin{aligned} \frac{1}{T_{wall}} &= \frac{\beta N_{impurity} k T \langle \Delta r \rangle S}{d\tau_0} e^{-E_{diff}/kT} \\ &+ \frac{3N_{impurity} \bar{v} \tau_{s0}}{2dT'_i} e^{E_{ad}/kT} \end{aligned} \quad (5.11)$$

According to the above equation, both the diffusion-induced and the surface-induced relaxation rates are proportional to the surface-volume ratio of the cell, *i.e.* to the inverse of the cell diameter d . Thus it is useful to describe the surface relaxation properties with a physical quantity ρ , which is commonly referred to as the “relaxivity”. The relaxivity is independent of cell geometry and is related to the wall

relaxation rate $1/T_{wall}$, the surface to volume ratio A/V by the following equation:

$$1/T_{wall} = \rho A/V \quad (5.12)$$

Fitzsimmons *et al.* [60] found by using impermeable aluminosilicate glass, the relaxation due to absorption can be greatly reduced thus increasing the total relaxation time. Heil *et al.* reported [64] glass cells that were internally coated with metallic films provided even longer relaxation time. Cs was one of the metals that greatly reduced wall relaxation rate as it blocks ^3He atoms from diffusing into the glass walls and it also has a low adsorption energy which leads to very short sticking time. For SEOP (Spin-Exchange Optical Pumping), we automatically profit from the Rb film which covers the inner surface of the pumping chamber. Similarly, another way to eliminate relaxation due to absorption is to coat the inner surface with sol-gel [65]. It is a mixture of aluminum nitrate nonahydrate $\text{Al}(\text{NO}_3)_3 \cdot 9\text{H}_2\text{O}$, ethanol and deionized water. The sol-gel coating also improves relaxation time by blocking ^3He atoms from diffusing into the glass.

5.2.2 Relaxation on Metal Surfaces

Since ^3He gas does not diffuse into metals [66], the relaxation is purely due to surface effects. However, the surface-induced relaxation on metal surfaces is not yet well understood. There are two additional relaxation mechanisms that need to be considered with metal surfaces compared to those for glass. The first mechanism is the depolarization of ^3He nuclei near the metal surface by oscillating magnetic field from eddy currents induced by the movement of these same nuclear dipoles. Smythe [67] derived the magnetic field generated by eddy current induced in a metal sheet by a moving magnetic dipole using the method of images. Timsit *et al.* [61] estimated the

relaxation due to eddy currents using the same method:

$$\frac{1}{T_m} = \frac{3 \times 10^{-4}}{\pi} \frac{\mu_{He}^4}{\bar{v} r_0^4 \hbar^2} \frac{A_p}{d^3} \quad (5.13)$$

where \bar{v} is the mean velocity of atoms, r_0 is the closest distance of the nucleus to the metal surface, d is the cell diameter, A_p is the area. According to Timsit *et al.* [61], T_m is on the order of 10^{16} s if $r_0 = 1\text{\AA}$ and $A_p = 9.2\text{cm}^2$. Even though the area of the cell is usually much larger in our studies and other parameters may take different values, it should still remain true that the relaxation rate of ^3He due to eddy currents can be safely neglected.

The second additional mechanism that contributes to relaxation of ^3He adsorbed on the metal surfaces is Korringa scattering [68]. Nuclear spins relax when the nuclei interact with conduction electrons in the metal, where the electrons flip spins and the spin states of the nuclei change. The Pauli exclusion principle states that the interaction is only allowed when the final state the electrons jump to are initially unoccupied. Thus according to Fermi statistics, only electrons with energy close (approximately within kT) to the Fermi energy level can participate in such interactions. Slichter [69] has derived the Korringa relaxation rate in metal to be:

$$\frac{1}{T_K} = \frac{(4\pi)^6}{9h^7} (g_s \mu_B \frac{\mu_K}{K})^2 \eta^4 m^3 \epsilon_F kT \quad (5.14)$$

To calculate the total Korringa relaxation rate due to a metal surface, one needs to consider the overlapping of wave functions of the conduction electrons and the nuclei of adsorbed ^3He atoms in the vicinity of the metal surface. Nelson [70] derived the total surface Korringa relaxation as:

$$\frac{1}{T} = \frac{1}{T_K} \frac{S}{V} \int_0^\infty f(l)^2 e^{-U(l)/kT} dl \quad (5.15)$$

where S and V are the surface area of the metal and total volume of the cell, respec-

tively, $U(l)$ is the atom-surface potential with the edge of the metal taken as $l = 0$, $f(l)$ is the fractional density of conduction electrons outside the surface. Nelson further used the work function of the metal to estimate $f(l)$, and assumed a van der Waals form for $U(l)$. His calculations suggest that the Korringa relaxation times for ^3He on various metal surfaces should be thousands of years, including the metal of interest for our studies, gold.

If eddy currents and Korringa relaxation are the only surface relaxation mechanisms, we would have very long lifetime for our test metal cells. Unfortunately, our series of studies have shown relaxation times to be between a few hours and 16 hours most of the time, for which both aforementioned relaxation mechanisms can be safely neglected. Although the dominating relaxation mechanism is still not well understood and significantly faster than those for which we have a better understanding, the results of our studies are still promising, as they suggest that the extra relaxation rate due to the use of metal end windows should still be small enough to allow future experiments to run at $60\mu\text{A}$ electron beam current.

5.3 Test Cell Fabrication

5.3.1 Overview

In order to study the relaxation rate due to metal surfaces, we have created and tested 19 cells, most of which contained metal tubes. The metal tubes were 5" in length and had 1" outer diameter, 3" of glass tubes were attached to both ends via a Houskeeper seal [20]. The resulting glass-to-metal-to-glass assembly is shown in Fig. 5.1. The total area of the metal surface was 101.3 cm^2 , and was far larger than what we anticipated would be used for metal end windows. This large geometry was

chosen to intentionally increase the relaxation rate due to metal. This particular design for the metal tubes was also favored for the convenience of manufacturing, as we were expecting a large number of test cells to be studied and any design that could save time had the potential to lead to a much shorter test time before finding a final design. A finished cell in Fig. 5.1 will be discussed later.

The making of these test cells usually included five steps:

1. Larson Electronic Glass [71] provided us a glass-to-metal-to-glass tube that used Houskeeper seal to bond glass and metal together.
2. The machine shop in the Physics Department of University of Virginia then mechanically polished the inside of the metal tube.
3. Able[72] Electropolishing electropolished the metal tube.
4. Epner[73] Technology Inc. electroplated the metal tube with gold.
5. Mike Souza at Princeton University, our glass blower, resized glass from stock material and made the final cell incorporating both glass and metal components. The resizing was for removing micro-fissures from the glass surface and reducing wall relaxation rates [74].

Each step will be described in what follows.

5.3.2 Glass-Metal Seal

Larson Electronic Glass fabricated our glass-metal-glass tubes as shown in Fig. 5.1. The glass-to-metal seal used by Larson is known as a Houskeeper seal [20]. The outside of the copper tube is machined down to a knife edge and is wetted with glass. The edge of copper is usually heated before covering with glass. The heating process creates a thin layer of crimson-color copper oxide as can be seen in Fig. 5.1. Houskeeper seals were originally used for vacuum, and we checked each seal down to



Figure 5.1: Shown on the left is a glass-to-metal-to-glass seal. The metal tube is 5" long by 1" outer diameter. The glass is wetted onto the knife-edge of copper on both ends. Shown on the right is a finished cell with the glass-to-metal-to-glass tube attached.

the level of $10^{-10}\text{ mbar} \cdot \text{l/s}$. To make sure that these seals would survive the high pressure JLab experiments, we also tested the integrity of them at pressures up to 20 atm for extended period of time.

The copper used in our tests was OFHC (oxygen-free high thermal conductivity)



Figure 5.2: Glass-to-metal seals survived pressure higher than 20 atm.

copper. In the earlier stage of our tests, OFHC copper was attached to Pyrex glass, in which case a direct connection could be made. For the later tests where we were moving closer to the final goal of using metal end windows with the impermeable aluminosilicate glass GE180, a transition glass between OFHC copper and GE180 had to be used. The coefficient of expansion for GE180 glass is not compatible for making a direct seal with OFHC copper, thus Corning 7052 Kovar sealing glass was used as the transition. The two materials connected by a seal should have similar coefficients of expansion, and the 7052 Kovar sealing glass served as an intermediate material to bridge the gap between OFHC copper and GE180. The other type of metal used in our glass–metal seals was titanium, for which only Pyrex was used.

5.3.3 Mechanical Polishing and Electropolishing

The mechanical polishing was done locally by our machine shop in the Physics Department. A wire brush attached to a lathe was placed inside the tube while the lathe spun. This first step of polishing produced a relatively smooth surface in preparation for the electropolishing process.

After the tubes were mechanically polished by the machine shop, they were sent to Able Inc. for electropolishing. The tube served as the cathode, which was im-

mersed in a temperature-controlled bath of electrolyte and connected to the positive terminal of a DC power supply, while the cathode attached to the negative terminal. During electropolishing, the polarized film is subjected to combined effects of gassing (oxygen) that occurs with electrochemical metal removal, saturation of the surface with dissolved metal and the agitation and temperature of the electrolyte. Metal on the surface is oxidized and dissolved in the electrolyte, the microscopic high points on the surface dissolve faster than the rate of attack on the other parts of the surface, which provides a smoothing effect. As a result, the electropolishing process removes a thin layer of metal (about $20 \mu m$ for our tubes), leaving a microscopically smooth and featureless surface. By contrast, even a fine mechanically polished surface will still show smears and other directionally oriented patterns or effects[4]. Fig. 5.3 shows a diagram of the polishing process and its smoothing effect.

5.3.4 Electroplating

As stated earlier, because of the good lifetime reported by Deninger *et al.*[75], gold was plated on the inner surface of the OFHC copper and titanium tubes. Epner Technology Inc. did the electroplating for us. Electroplating is the reverse process of electropolishing. When electric current passes through the electrolyte, the electrolyte splits up and some of the desired metal atoms it contains are deposited in a thin layer on top of the electrodes. Nickel and chromium are two common undercoatings used for electroplating, however, they are both ferromagnetic and cannot be used for us as they would introduce additional spin relaxation. As a result, Epner used a copper strike to improve the durability of gold coating. A $5 \mu m$ layer of gold was subsequently electroplated on the inner surface of the tubes. Fig.5.4 shows a comparison of an OFHC copper tube with and without gold-coating.

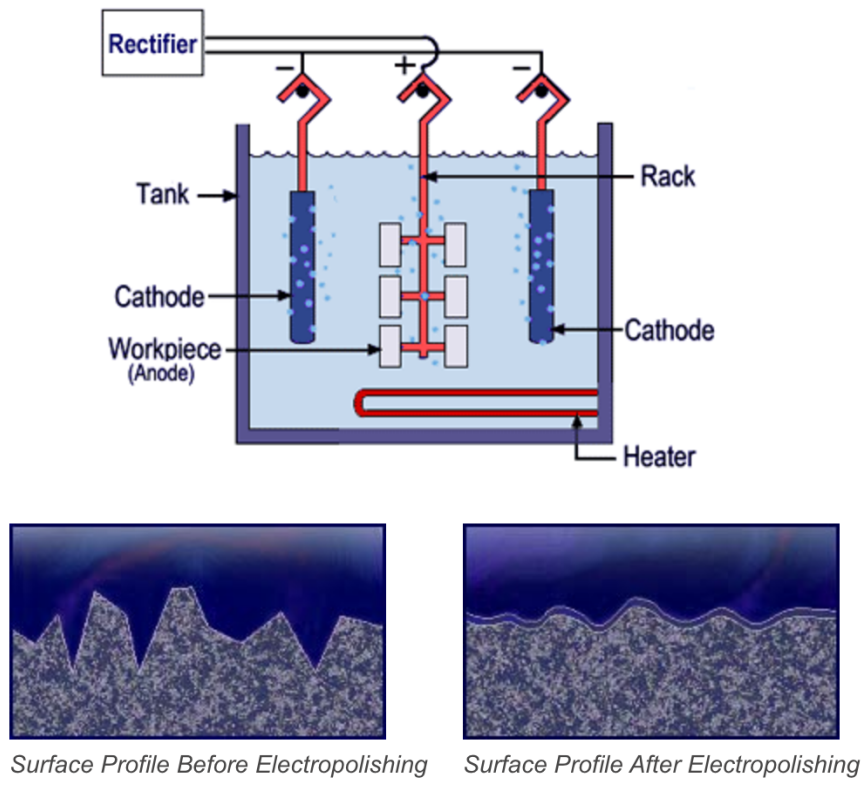


Figure 5.3: Electropolishing [4]

5.3.5 Final Assembly of the Cell

After the tubes were coated, shipped back to us and leak checked one more time, they were cleaned with our ultrasonic cleaner. Fig. 5.5 shows the setup of the cleaning process. We cleaned the impurities on the surfaces of the tubes with ethanol, deionized water and methanol for thirty minutes each. As shown in the figure, a beaker containing the chemical solution and the tubes were placed in water bath inside the ultrasonic cleaner. Because of the dimensions of the cleaner and the beaker, we cleaned one end of the tubes first then flipped them to clean the other end before switching solution.



Figure 5.4: Shown left is the inner surface of a gold coated OFHC copper tube. Shown right is a OFHC copper tube without coating.



Figure 5.5: Ultrasonic cleaner with 3 tubes being cleaned.

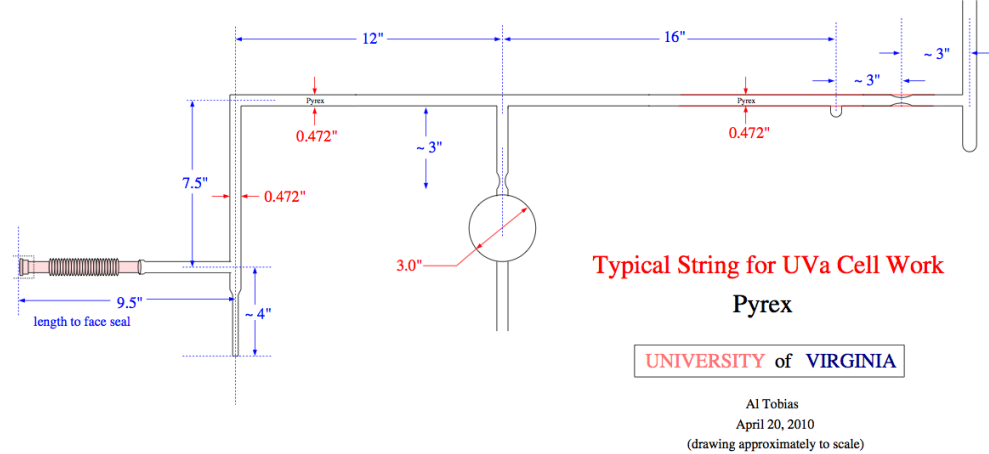


Figure 5.6: Shown is the design of a typical string for our test cells.

The test tubes were then shipped to our glassblower Mike Souza at Princeton University. All glass was reblown to the right size to reduce micro-fissures which would lead to high relaxation rate. The test tube was spliced to transfer tube and pumping chamber as shown in Fig. 5.1. A string (see Fig. 5.6) which would be used for cell filling was also made at Princeton. Traditionally, a pure glass cell would be placed entirely in an oven for annealing. A cell made with GE180 would go through a five-minute ramping time to 780°C , stay at 780°C for five minutes and slowly cool down to room temperature for at least 5 hours [5]. A Pyrex cell would be annealed in the exact same way except the highest temperature is 565°C . However, most of our test cells could not have been annealed in the same way because of the glass-metal seal. Had we expose a seal to high temperature for long period of time, gold atoms might have migrated into the metal substrate and the seal might even break. Thus the metal tubes were attached to the rest of the glass parts after the pure glass parts were annealed.

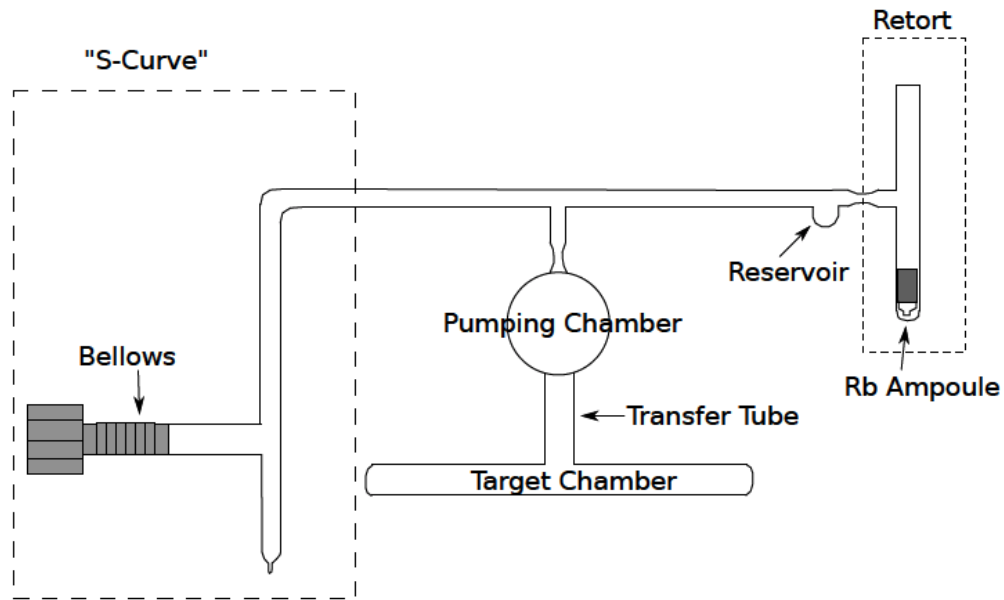


Figure 5.7: A diagram of a Pyrex string with a cell and a retort attached while connected to the gas system through the bellows. Adapted from Matyas [5].

5.4 Cell Fill Procedure

The details of cell fill was described thoroughly by Matyas [5], I will briefly cover the process for the sake of completeness.

5.4.1 Cell Fill Preparation

Although the actual cell fill work took less than a day, the preparation that led to the fill usually took 10-15 days. The glass manifold to which the cell was attached, the cell itself and a “retort” were spliced together and attached to our homemade gas system through a bellows. A pre-scored ampoule of alkali metal was dropped into the top the of the retort. Fig. 5.7 is a diagram of the string, cell and retort all connected together.

The entire system was first rough-pumped with a mechanical pump, and then

pumped by a diffusion pump to even higher vacuum. After the system was pumped for a few days and alkali metal was added in the system, we would keep pumping the system with the diffusion pump for roughly a week. To prevent back streaming of diffusion pump oil from getting into the gas system and the cell, a cold trap above the diffusion pump was filled every day with liquid nitrogen. “Flamebakes” were also performed 2-3 times each day during the one-week pumping period. A methane-oxygen torch was used to gently bake the glass during the flamebakes. The bake started from the retort which was the farthest away from the diffusion pump, and moved slowly towards the bellows, so the impurities chased off the inner surfaces could be “swept” towards the pump leaving as few impurities behind as possible. The alkali metal was typically melted in the retort starting with the second or third flamebake and continuing with each of the remaining flamebakes. On the day before the fill, alkali metal was melted and chased into the pumping chamber.

5.4.2 Cell Fill

The first thing on the fill day was to pump all portions of the gas system to vacuum and selectively back fill some parts with appropriate gases (either N₂ or ³He) to minimize outgassing. The gas filled into the cell should always be cleaned during the path to the cell. Earlier test cells were filled with the noble gas purifier while the later cells were done with a homemade cryogenic trap.

The homemade cryogenic trap consisted of copper tubing placed inside a box-shaped Dewar. The Dewar was filled with liquid nitrogen when filling N₂ and liquid helium when filling ³He, so impurities in the gas were frozen in the copper tubing. Temperature inside the dewar was monitored with two silicon diodes to determine whether the copper tubing was fully submerged in the cold liquid.

The volume of the cell was also determined during the fill process. A Baratron pressure gauge was used to measure a calibrated volume (CV) of 992.9 cc. Roughly 300 Torr of gas was filled into the calibrated volume, then the valve on the CV was closed and any gas outside of CV was pumped away. Next the gas kept in the CV was let out into the fill gap between the CV and the string, then into the cell while monitoring pressure with the Baratron gauge, thus the volume of the cell could be calculated with the ideal gas law.

Around 70 Torr of nitrogen was put into the cell before filling with ^3He . To prevent nitrogen from escaping the cell while filling ^3He , the string valve was kept closed until ^3He pressure in fill gap rose well above 70 Torr. A total gas pressure of just under 760 Torr (1 atm) was reached. The target pressure was chosen for practical reasons. When target cell was pulled off from the rest of the glass tubing, the connection between the cell and the string was melted. If the interior pressure was lower than 1 atm, the atmospheric pressure would essentially push the melted portion inward and seal the cell for us. The alkali metal used in filling all the cells described in this chapter was Rb, with the one exception of Kappa1 that was filled with a 5:1 mixture of K and Rb.

5.5 Experimental Setup and Procedure

All cells containing metal were tested with Pulse NMR in order to minimize depolarization from eddy currents. Kappa1 was a simple spherical and pure GE180 cell, which was built to rule out the possibility that the melt of GE180 used in our cells had quality problems. Because of its lack of metal and lack of convenient places on which to wrap pickup coils, Adiabatic Fast Passage was used to test Kappa1. Both PNMR and AFP were discussed in a general way in chapter 3, I will only add to

the discussions by describing more specific experimental setups used for these studies. Spindown measurements were the main means of studying relaxation properties, I will also discuss how we used spindowns with different sampling rate to extract PNMR losses and lifetime corrected for such losses.

5.5.1 Pickup Coils

In an AFP measurement, pickup coils are placed next to the side windows of the oven. However, the same setup proved to be more difficult for us to receive high-quality PNMR signals. To keep the pickup coils from the heat of the oven and to be physically close to the samples of ^3He , we manually wrapped a solenoid coil on the transfer tube of test cells where it was approximately 2" below the bottom of the oven. These coils were made with 40-50 turns of AWG 20 copper wire. Because of the off-center position of the pickup coils with respect to the magnetic holding field, inhomogeneities were significant enough to affect FID signals, and gradient coils were used to cancel such inhomogeneities.

5.5.2 Gradient Coils

Inhomogeneities were minimized using three sets of gradient coils. Each set of gradients coils consisted of two oppositely wound coils separated by a distance d ; this particular type of coils is referred to as "Maxwell coils". The setup is very similar to that of Helmholtz coils, except the opposite direction of currents and the larger optimum separation $d = \sqrt{3}R$, where R is the radius of the coils. The opposite direction is to cancel out the magnetic field at the center, and the optimum separation makes the nonlinear terms among the first four in the Taylor expansion of the inhomogeneities zero[76]. Fig.5.8 shows the coil orientations. The z axis is defined to be

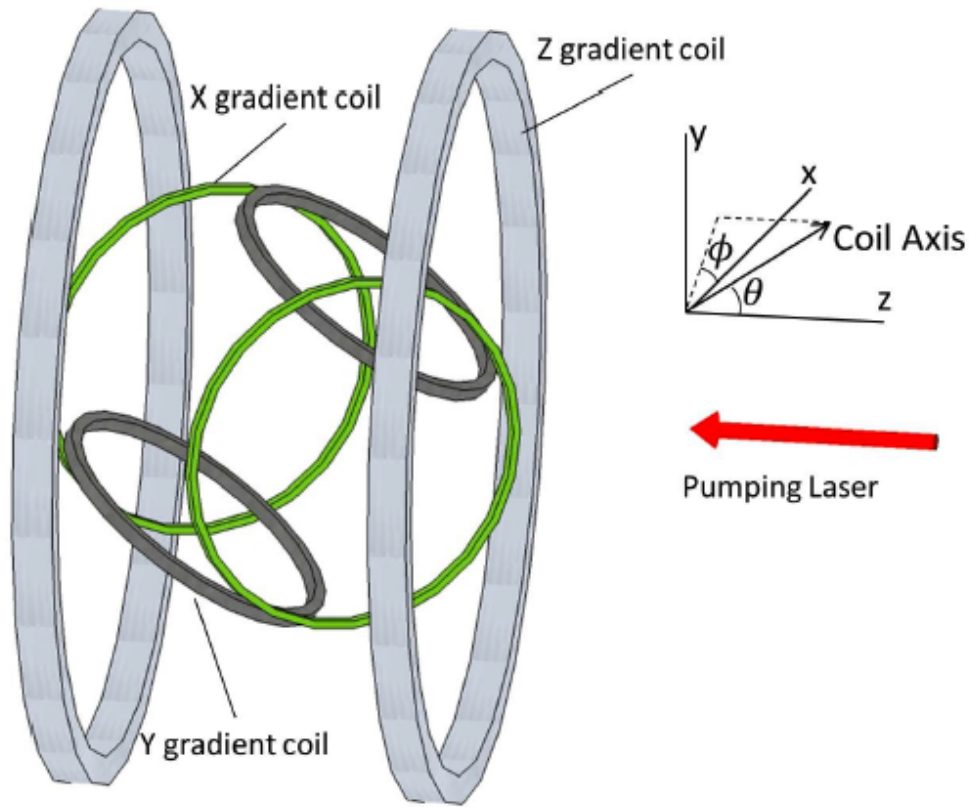


Figure 5.8: Diagram of the coils. Adapted from Zheng [6].

aligned with the direction of the holding field while x and y axes are in the transverse plane. The direction of coil axis is then defined by the angle θ and ϕ , where θ is with respect to the z axis and ϕ is the azimuthal angle in the x-y plane.

The magnetic field gradient at the center is given by[40]

$$\begin{aligned}\nabla \mathbf{B}(\theta, \phi) &= \begin{bmatrix} \partial B_x / \partial x & \partial B_y / \partial x & \partial B_z / \partial x \\ \partial B_x / \partial y & \partial B_y / \partial y & \partial B_z / \partial y \\ \partial B_x / \partial z & \partial B_y / \partial z & \partial B_z / \partial z \end{bmatrix} \\ &= 3\kappa I \begin{bmatrix} \sin^2 \theta \cos^2 \phi - \frac{1}{3} & \sin^2 \theta \sin \phi \cos \phi & \sin \theta \cos \theta \cos \phi \\ \sin^2 \theta \sin \phi \cos \phi & \sin^2 \theta \sin^2 \phi - \frac{1}{3} & \sin \theta \cos \theta \sin \phi \\ \sin \theta \cos \theta \cos \phi & \sin \theta \cos \theta \sin \phi & \cos^2 \theta - \frac{1}{3} \end{bmatrix} \quad (5.16)\end{aligned}$$

where the calibration constant κ is:

$$\kappa = \frac{3\pi n R^2 d / 2}{5(d^2/4 + R^2)^{5/2}} G \text{ cm A}^{-1} \quad (5.17)$$

The most important terms in Eq.5.16 are those related to B_z : $\partial B_z / \partial x$, $\partial B_z / \partial y$ and $\partial B_z / \partial z$. The orientations of the gradient coils can be chosen such that each of the three sets of coils controls only one of the aforementioned terms. Such orientations require a specific value of θ which is referred to as the “magic angle” θ_m :

$$\theta_m = \cos^{-1} 1/\sqrt{3} = 54.7^\circ \quad (5.18)$$

For $\theta = \theta_m$ and $\phi = 0$ the gradient tensor is

$$\nabla \mathbf{B}(\theta_m, 0) = \kappa I \begin{bmatrix} 1 & 0 & \sqrt{2} \\ 0 & -1 & 0 \\ \sqrt{2} & 0 & 0 \end{bmatrix} \quad (5.19)$$

For $\theta = \theta_m$ and $\phi = \pi/2$ we have

$$\nabla \mathbf{B}(\theta_m, \pi/2) = \kappa I \begin{bmatrix} -1 & 0 & 0 \\ 0 & 1 & \sqrt{2} \\ 0 & \sqrt{2} & 0 \end{bmatrix} \quad (5.20)$$

Finally, for the z gradient coil we have

$$\nabla \mathbf{B}(0, 0) = \kappa I \begin{bmatrix} -1 & 0 & 0 \\ 0 & -1 & 0 \\ 0 & 0 & 2 \end{bmatrix} \quad (5.21)$$

Our gradient coils were built by Zheng [6]. The separations do not follow the optimum condition $d = \sqrt{3}R$ due to spatial limitations. The dimensions of the gradient coils are shown in Table 5.5.2.

	turns	radius	separation
x	42	33 cm	64 cm
y	100	28 cm	56 cm
z	8	66 cm	66 cm

5.5.3 Laser Setup

In an earlier stage of the study, narrow-band Comet lasers from Newport was used. Each Comet laser provided roughly 20 W power, the optical fibers were combined through a “combiner” which required water cooling if multiple lasers were used at the same time. In later studies, a single Raytum laser was used instead as it could provide much higher power. Both the Comet laser and Raytum laser had around 0.2 nm FWHM (full width at half maximum).

Fig. 5.9 shows a diagram of the optics used for SEOP (spin-exchange optical pumping). After coming out of the fiber head, laser was focused by two lenses L1 and L2 such that the power spread enough to not damage the polarizing cube and was focused to an appropriate size at the cell position. The polarizing cube separated the beam into two beams with orthogonal linear polarizations. The beam with polarization parallel to the plane of the figure went through the cube, and the other beam with polarization perpendicular to the plane was reflected. The reflected beam went through a QWP (quarter wave plate), reflected at a mirror, went through the QWP one more time. Its polarization was changed to be parallel to this plane at this point and went through the cube. This beam is referred to as the “main beam” as it is ideally aligned with the holding field. The beam that went through the cube the first time was sent towards the oven by a mirror. Because of the small angle relative to the main beam, this is called the “skew beam”. Both the main beam and the skew beam went through QWP before arriving at the oven window and were turned to circular polarization in the same direction.

5.5.4 PNMR Losses and Corrected Lifetime

As described in chapter 3, there are generally two methods for us to determine polarization losses due to measurements: one is to take several measurements quickly enough that all depolarization can be attributed to measurement losses, the second method is to take multiple spindown measurements each with a different sampling rate. PNMR measurements cause a fraction of longitudinal polarization to be lost, two adjacent measurements require a long enough separation so the depolarization effect can be fully dispersed. For this reason, the first method mentioned above is not an option for PNMR. We have applied the second method to most of the 19 test

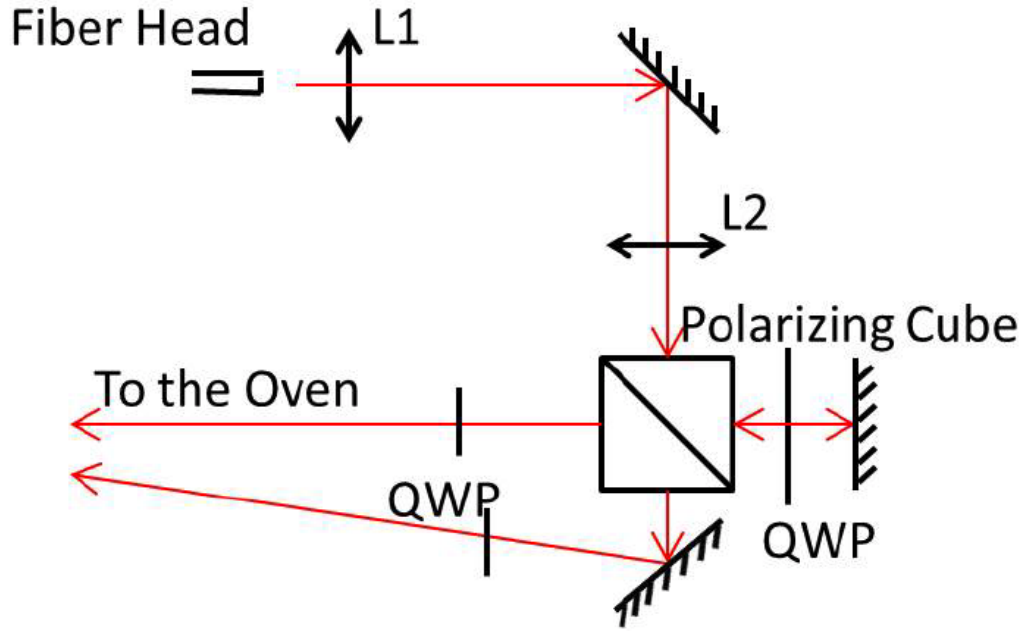


Figure 5.9: Optics for spin-exchange optical pumping. Adapted from Zheng [6].

cells that had lifetime of at least a few hours.

A spindown typically comprises a series of measurements of FID (Free Induction Decay) signals. Obtaining a good FID signal generally requires tuning the holding magnetic field and the gradient settings to reduce inhomogeneities.

In a PNMR measurement, it is important that the RF frequency is the correct Larmor frequency of the holding field. The RF frequency was set to be at 56.6 kHz, it was often the case the holding field would start being off-resonance at the beginning. As Fig. 5.10 shows, the signal collected by the pickup coil was mixed with a mixing frequency before being recorded. The output of the mixing process gave us a signal whose frequency was the absolute value of the difference between the signal frequency and the mixing frequency. By lowering the frequency from 56.6 kHz to below 100 Hz, we were able to use the band pass on the preamplifier to improve the signal to noise ratio. However, this lower frequency does not provide information about whether the

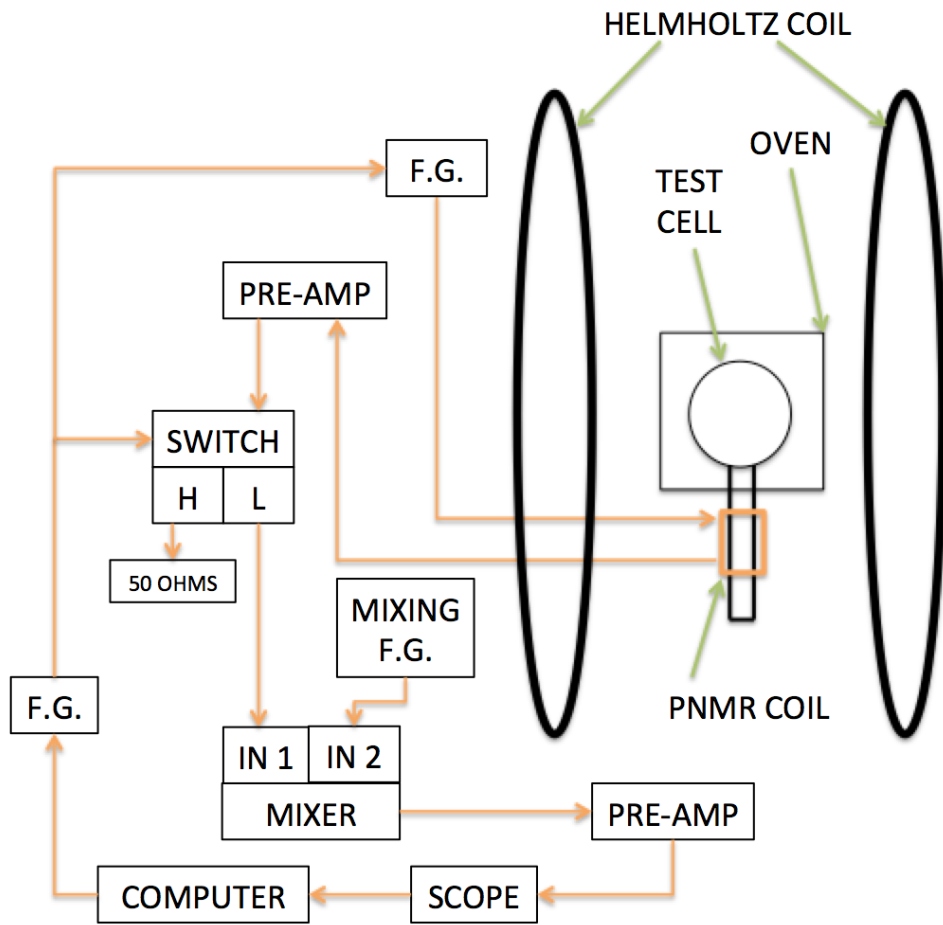


Figure 5.10: PNMR setup.

frequency of the signal (which was proportional to the holding field) was above (or below) the mixing frequency. By intentionally changing the mixing frequency by an appropriate amount and observing if the recorded frequency increased or decreased, we were able to tell whether the recorded frequency should be added to or subtracted from the mixing frequency to give us the true signal frequency. The holding field was proportional to the current which was monitored with a shunt resistor, thus the next step was to use the proportionality to calculate the corresponding shunt resistor value for the correct field for the RF pulse. This was further complicated by non-zero fields produced by gradient coils as the pickup coil location was not at the center of

the coils. However, the calculation of shunt resistor value typically brought us closer to the resonance field.

The settings of the gradient coils also required tweaking in most cases. In order to reach longer transverse relaxation time T_2^* , the inhomogeneities needed to be low. Because the pickup coils were often at least 3-4 inches below the center of the fields, gradient coils were very useful for decreasing the inhomogeneities. The center of the pickup coils was in the same x-y plane (x, y and z axes were defined the same way as in Fig. 5.8) with the center of the fields, so it was expected either $\partial B_z / \partial x$ or $\partial B_z / \partial y$ was initially the dominant term in field inhomogeneities. So x or y gradient coils should provide the most significant improvements at the beginning, while it also produced non-zero partial derivatives in other directions that needed to be canceled with other gradient coils later and non-zero field that required further field tuning. The adjusting of the holding field and the gradients settings were an iterative process for achieving long T_2^* and high-quality FID signals. Fig. 5.11 shows an FID signal with approximately 150 ms T_2^* . FID signal was typically fitted to the equation:

$$s(t) = a \sin(\omega t + \phi) e^{-t/T_2^*} + b \quad (5.22)$$

where a is the amplitude of the signal, b is the offset, ω is the RF frequency, ϕ is an offset of the phase and T_2^* is the measured transverse relaxation time. The amplitude a was used to represent the points in spindowns.

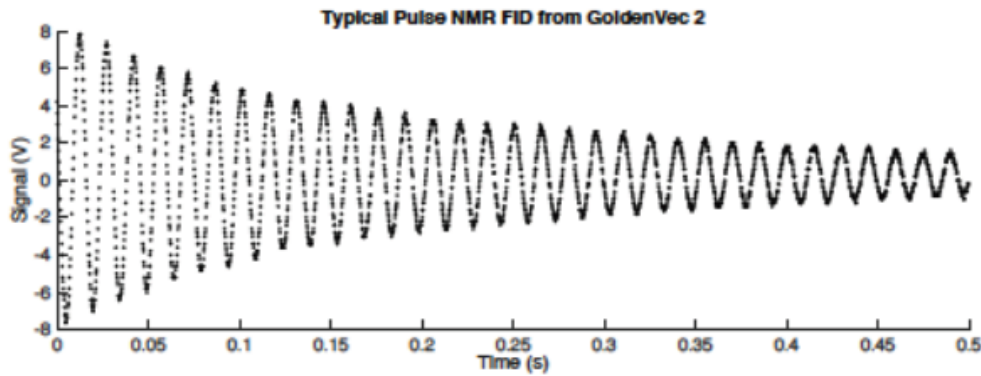


Figure 5.11: A PNMR signal taken with gold coated test cell.

Once the optimal settings were found, multiple spindowns were taken. Each spindown was a series of PNMR measurements set apart with a fixed time interval. Multiple values of intervals were used for different spindown measurements, each of the intervals was typically repeated at least twice. Fig. 5.12 shows 3 spindowns for the test cell GoldenVec1 which had a horizontal metal tube and similar configuration to that of a convection style cell. The time interval used for the 3 spindowns were 20 min, 30 min and 60 min, respectively. Using the additional relaxation rate due to taking PNMR once every hour as the base rate Γ_{PNMR} , the measured relaxation rate for taking n PNMR every hour can be related to the true lifetime (without relaxation from PNMR) by:

$$\frac{1}{T_{measured}} = \frac{1}{T_{true}} + n \cdot \Gamma_{PNMR} \quad (5.23)$$

in the relation of $\frac{1}{T_{measured}}$ versus n, $\frac{1}{T_{true}}$ is the intercept, and the Γ_{PNMR} is the slope.

Fig. 5.13 shows the linear fit between the sampling rates (n) as x and the inverse of measured lifetimes as y. The intercept is $0.0676\ hr^{-1}$, thus the true lifetime without any loss due to taking PNMR measurements is $1/0.0676 = 14.8\ hr$. The slope is

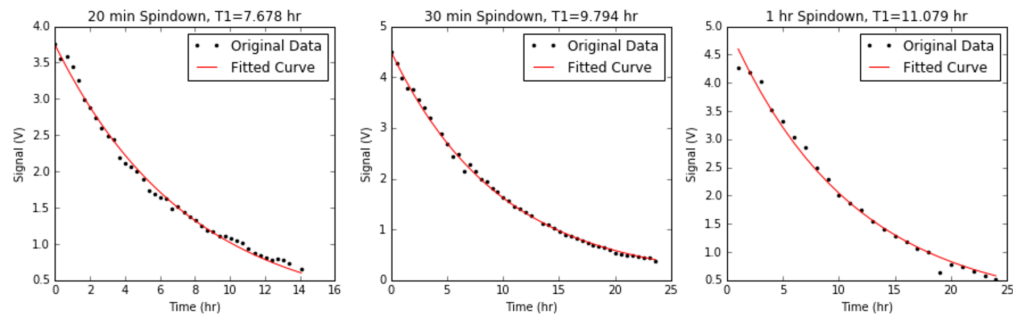


Figure 5.12: 3 spindowns of the cell GoldenVec1 each with a different sampling rate.

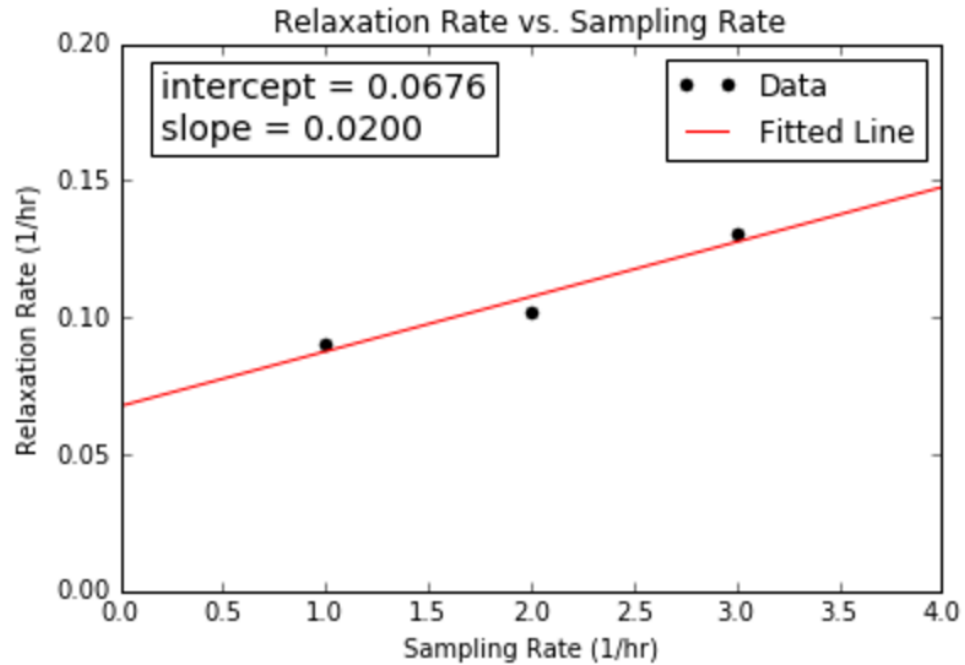


Figure 5.13: A linear fit to extract lifetime corrected for relaxation due to PNMR losses.

0.02 hr^{-1} , which means the relaxation rate due to taking one PNMR per hour is $1/50 \text{ hr}^{-1}$. The percentage loss of polarization due to a single PNMR measurement can be calculated as:

$$1 - e^{-t \cdot \Gamma_{PNMR}} = 1 - e^{-1 \times \frac{1}{50}} = 0.0198 = 2\% \quad (5.24)$$



Figure 5.14: A diagram of target cell with metal end windows.

5.6 Relaxation Measurement Results and Discussion

The end goal of this series of studies was to replace the traditional glass end windows on our target chamber with metal end windows as Fig. 5.14 shows. Although no metal end windows have been produced yet, 19 test cells with various configurations and compositions were studied to explore the feasibility of incorporating metallic components into glass cells. We have gone through different stages of studies, and from each we made new discoveries and stepped closer to the end goal. At this point, we have demonstrated that gold coated OFHC copper is strong enough to survive the high gas pressure of electron scattering experiments, only brings a relatively small amount of relaxation rates to a convection style target cell made with GE180 under SEOP conditions. The following discussion will be separated into different stages that each revealed parts of the mystery and generally follow chronological order (except cells made with titanium will be covered at the end). The cell preparation information and results of measurements are listed in Table 5.1.

Cell Name	Fill Type	Geometry	Glass	Metal	Max Lifetime (hr)	Fill Date
Tyrion	NGP	Sphere	GE180	Gold on glass	1.21	6/18/09
Gold Maiden1	NGP	Flange	Pyrex	Gold on Copper	2.14	6/18/10
Gold Maiden2	NGP	Flange	Pyrex	Gold on Copper	None	8/14/10
Gold Maiden3	NGP	Flange	Pyrex	Gold on Copper	6.49	11/11/10
Goldfinger	NGP	Vertical	Pyrex	Gold on Copper	3.59	4/28/13
Cupid	NGP	Vertical	Pyrex	Bare Copper	3.13	6/15/13
Goldeneye	NGP	Vertical with Valve	Pyrex	Gold on Copper	13.94	10/2/13
GoldRush	NGP	Vertical	Pyrex	Gold on Copper	14.81 [†]	11/8/13
Pyrah	NGP	Vertical	Pyrex	None	26.52 [†]	2/1/14
GoldenVec	NGP	Horizontal	Pyrex	Gold on Copper	10.6	10/18/14
TitanVec	NGP	Horizontal	Pyrex	Gold on Titanium	0.52	12/15/14
GoldenVec2	Cryogenic	Horizontal	Pyrex	Gold on Copper	15.6	2/14/15
Titan	NGP	Vertical	Pyrex	Bare Titanium	None	3/11/15
GoldenVec180	Cryogenic	Horizontal	GE180	Gold on Copper	4.43	6/17/15
GolderVec360	Cryogenic	Horizontal	GE180	Gold on Copper	3.01	7/11/15
Tweety	Cryogenic	Vertical	Pyrex	Canary Glass	22.7	9/22/15
Sylvester	Cryogenic	Horizontal	GE180	Canary Glass	6.39	11/20/15
Kappa1	Cryogenic	Sphere	GE180	None	72.17	2/6/16
Goldfinger180	Cryogenic	Vertical	GE180	Gold on Copper	12.4 †	5/19/16

Table 5.1: Shown are the fill information, design and maximum measured lifetime of the test cells. Fill type is the method used to clean the gas. [†] indicates the maximum lifetime was obtained at an elevated position. Although canary glass is not metal, it is listed in the column of metal for Tweety and Sylvester for the sake of keeping the structure of the table simple.

5.6.1 Gold Coated Spherical Cell

Our very first attempt at incorporating metal was a spherical GE180 glass cell with gold coated on the interior surface. Although this attempt was made before I joined the group as were the spool pieces that will be mentioned below, they are still included for the sake of completeness of this study.

The measured lifetime of the first test cell was only 1.21 hr, which was attributed to impurities in the cell. Several attempts were made to identify better coating techniques, but it was decided that developing a better technique would not be easy. Since these early attempts involved gold on glass, not gold not metal, it was decided to move directly to studying gold-coated metal components where it was established that commercial services were available.

5.6.2 Gold Coated Spool Pieces

The first cell with a gold coated (by Epner) OFHC copper tube was named “Gold Maiden” and made in 2010. Fig. 5.15 is a picture of the cell which was referred to



Figure 5.15: A picture of Gold Maiden, generally referred to as the “spool piece”.

as the “spool piece”. The bottom end of the cell was capped off, while the other end was attached to a glass flange. The flange was then connected to the transfer tube of the cell. The seal was made with o-rings.

The tests of Gold Maiden was divided into three stages. Initially it had a lifetime of 2.14 hr before discoloration of Rb was observed. Discoloration is typically a sign of Rb reacting with air, which indicated either a leak or significant amount of outgassing from the o-rings. To separate Rb from possible outgassing, the pumping chamber was pulled off via glassblowing. Measurements of the separated pumping chamber showed a lifetime of 109.2 hr after correcting for AFP losses. The rest of the cell was attached to a different pumping chamber in each of the two series of measurements that followed. The second series of measurements did yield any meaningful result due to a leak. The third series of measurements produced a lifetime of 6.49 hr. The spool piece encouraged further investigation into gold coated OFHC copper that could be attached to glass without o-rings.

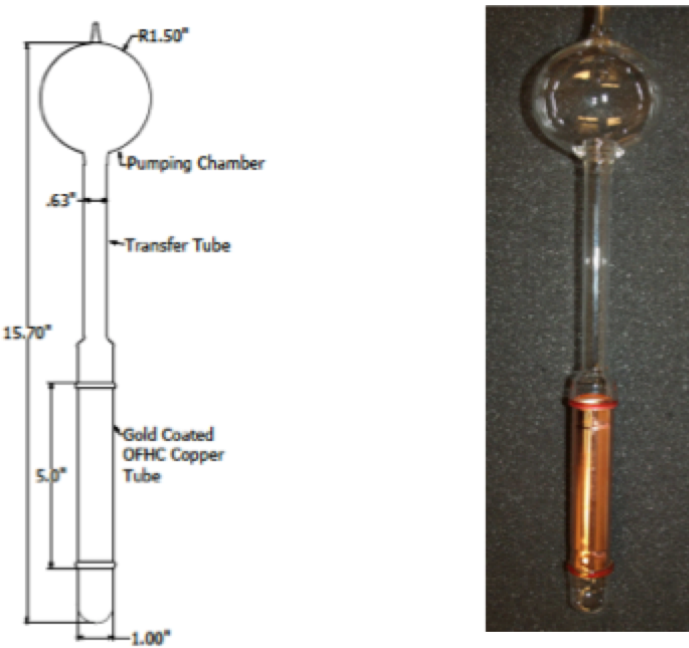


Figure 5.16: Design and picture of Goldfinger.

5.6.3 Vertical Cells

Since o-rings were the primary suspects of the short lifetime for the spool piece, a method to seal copper directly to the glass was highly desirable. We started using the Houskeeper seal, and five cells were made at this stage: Goldfinger, Cupid, Goldrush, Goldeneye and Pyrah. All 5 cells were designed to have the same dimensions. Fig. 5.16 shows the design drawing and a picture of the cell Goldfinger. Goldrush was of the same design. The only difference for Cupid was that the OFHC copper was not coated. Pyrah was a pure Pyrex control cell.

The first cell tested, Goldfinger, had a maximum lifetime of 3.59 hr at the beginning of the test. However, subsequent tests showed noticeable degradation. Towards the end of testing Goldfinger, the lifetime was at a minimum of 2.36 hr. Cupid had a similar maximum lifetime of 3.13 hr initially. However, a rapid degradation of lifetime was observed. The last measurement we were able to perform displayed a lifetime of

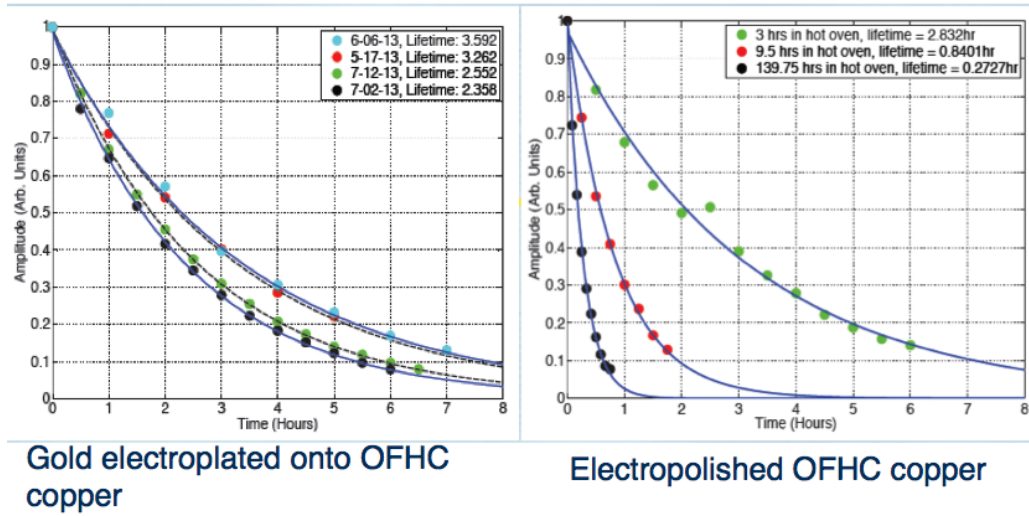


Figure 5.17: The observed degradation of lifetime for Goldfinger (left) and Cupid (right). Shown in each of the two plots were several spindowns at different stage during the tests. The initial amplitude of the spindowns were scaled to 1 for better comparison of lifetime.

only 0.27 hr. It is worth noting a leak on Goldfinger was discovered during the filling process. Although the leak was fixed with Celvaseal Leak Sealant, either the sealant or the leak itself might have contributed to the short lifetime of Goldfinger and its degradation. The degradation could also be attributed to possible reaction between Rb and copper. Fig. 5.17 displays the lifetime degradation during our tests.

During the tests of Goldfinger and Cupid, it was suspected that Rb reacted with metal surfaces and produced detrimental effects to lifetime. A gold coated OFHC cell with a valve, GoldenEye, was designed and produced to isolate Rb vapor from the metal tube, as shown in Fig. 5.18. GoldenEye was only polarized with the valve closed, thus isolating the metal tube from most of the Rb vapor. Spindown measurements were taken at room temperature both with the valve closed and open. The lifetime was measured to be 13.94 hr with the valve closed, and it was only 4.09 hr with the valve open. The large difference of lifetime indicated the part of the cell below the valve introduced very significant relaxation rate. It is also worth noting



Figure 5.18: A picture of GoldenEye, the only test cell made with a valve.

the inclusion of the valve increased the total length of the cell substantially, which exposed the bottom part of the cell to high field inhomogeneities that could lead to high relaxation rate.

Due to the leak found in Goldfinger, it was necessary to produce another test cell with the same design, which was named as “Goldrush”. Fig. 5.19 displays four spindowns taken before tests in which the cell was elevated (will be discussed later). All four measurements have similar results with the maximum lifetime being 12.1 hr. This was the first metal cell we produced that had more than 10 hr lifetime.

A calculation of the magnetic field inhomogeneities was also done around the time. As seen in Fig. 5.20, the relaxation time due to inhomogeneities at the center of the pumping chamber was about 300-700 hr. However, the bottom of cell was exposed to surprisingly large inhomogeneities which would result in a relaxation time of 1-5 hr. This provided incentive for measurements of lifetime while raising the cell to more homogeneous region. Due to spatial constraints, the cell was only lifted by 10 cm,

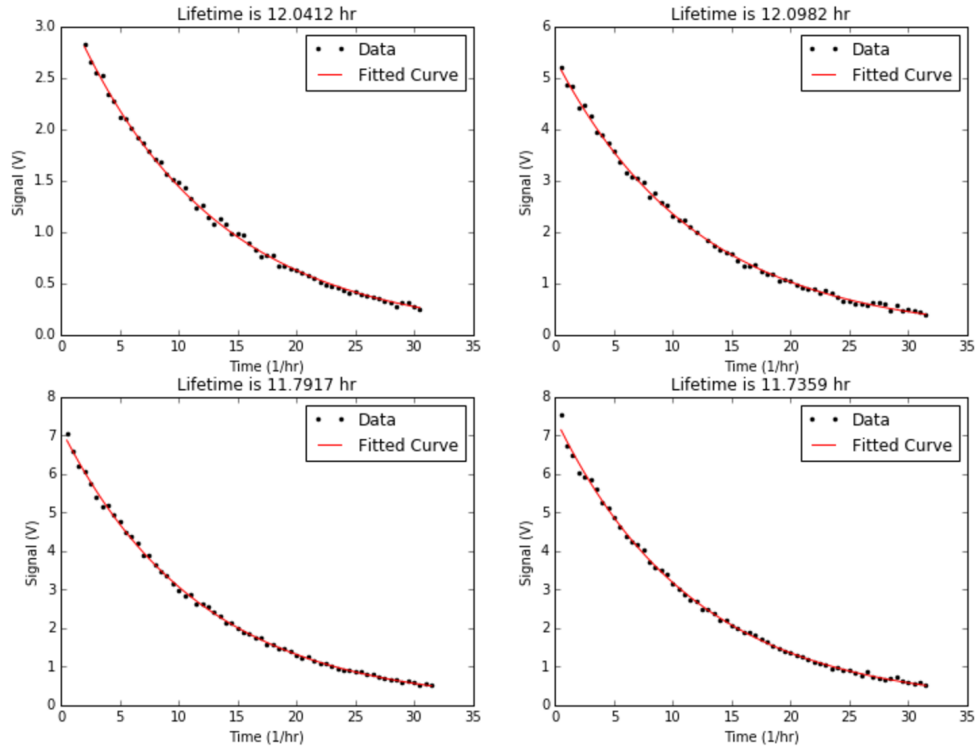


Figure 5.19: Four spindowns of Goldrush before elevating the cell. All four measurements display similar lifetime with no obvious sign of degradation.

which led to an increase in lifetime to 14.81 hr, the longest lifetime we had measured at the time with metal cells.

To understand the additional relaxation rates introduced by metal surfaces, a control cell, Pyrah, was made with pure Pyrex was produced. The control cell had a lifetime of 19.71 hr before elevation, and 26.52 hr after being lifted by 10 cm. Since Pyrah had the same dimensions as Goldrush, a direct comparison suggested the additional relaxation rate due to the metal tube was around $1/25\text{ hr}$.

5.6.4 Horizontal Cells

The increase of lifetime after elevating Goldrush and Pyrah motivated us to make more compact cell designs. This resulted in a design very similar to that of a convec-

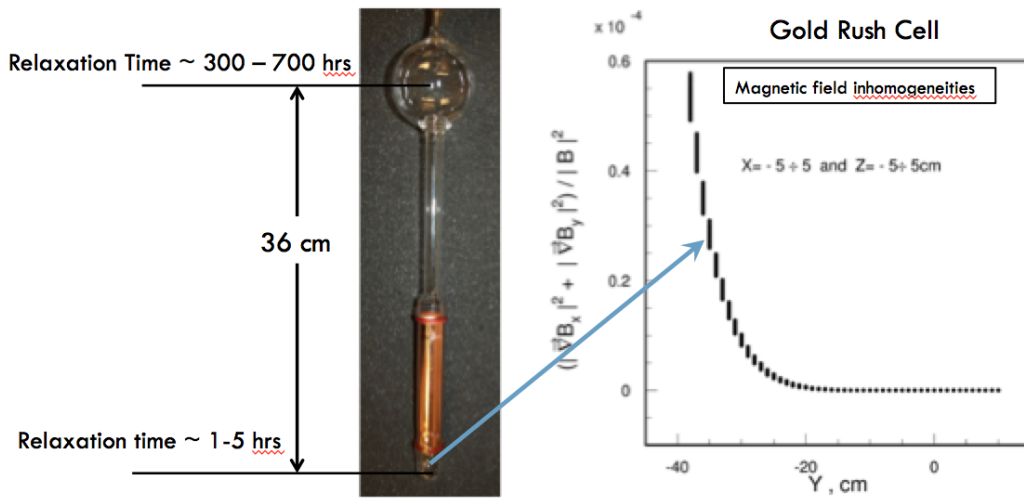


Figure 5.20: Shown on the right is the inhomogeneities vs. vertical distance from the center of the field. Shown on the left is the cell Goldrush with relaxation time due to field inhomogeneities as displayed on the right.

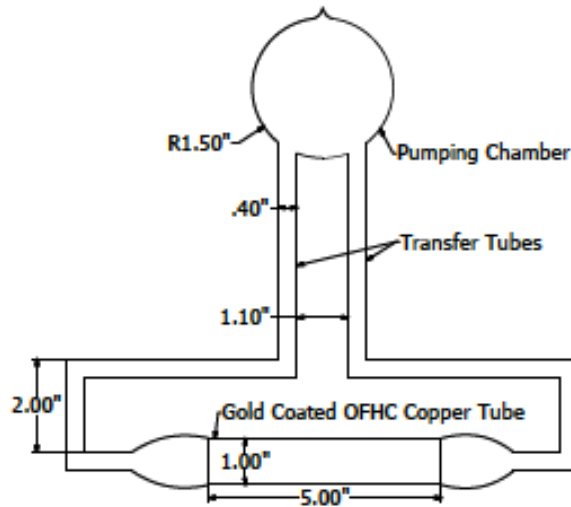


Figure 5.21: Design of the horizontal cell GoldenVec.

tion style cells with the metal tube placed horizontally. The overall vertical length was shortened from 15.75" to about 10". The dimensions of this style of cells can be seen in Fig. 5.21.

The first horizontal cell was GoldenVec. It had a lifetime of 10.6 hr, which was

shorter than we had hoped for. Up to this point, all test cells were filled using the noble gas purifier in our lab. A convection cell filled at the time that used the cryogenic trap to condense the impurities in the gas turned out to have much greater lifetime compared to the previous convection cell of the same design but used the noble gas purifier. In light of this, GoldenVec2 was created with the same design as that of GoldenVec and filled using a cryogenic trap. GoldenVec2's lifetime was measured to be 15.6 hr, the longest lifetime of metal cells we have obtained to date. All test cells from then on were filled using the same cryogenic trap.

5.6.5 GE180 Cells

It was widely acknowledged that the impermeable aluminosilicate glass GE180 had less associated wall relaxation rates than that of the borosilicate glass Pyrex. Since GoldenVec2 and Goldrush had demonstrated good enough lifetime, it was time we started exploring GE180 cells with metal tubes. Two GE180 test cells, GoldenVec180 and GoldenVec360, were made with the design as seen in Fig. 5.21. Because of the difficulty in bonding GE180 to OFHC copper, Corning 7052 was used as the transition glass. The measured lifetime of GoldenVec180 and GoldenVec360 were 4.43 hr and 3.01 hr, respectively. Since GE180 glass normally provide longer relaxation time, we made additional cells to test hypotheses to explain the short lifetime.

The first suspect occurred to us was the transition glass Corning 7052, since it had never been tested in our group. As we had experience with an alternative transition glass, canary glass (uranium glass), we built two test cells with 5" long by 1" OD tubes of the canary glass in place of copper tubes. The first was a replicate of the vertical cell Goldfinger and named as Tweety. The second was a replicate of the horizontal cell GoldenVec and named as Sylvester.

Tweety had a lifetime of 22.7 hr, which was quite close to the lifetime of the control cell Pyrah, 26.52 hr. A shorter lifetime was expected as uranium is paramagnetic, however, the result of Tweety proved that that expectation was incorrect and canary glass could in fact be used to build target cell.

Sylvester was fabricated in the same way that GoldenVec was in that the canary glass tube and the GE180 portion directly connected to the tube were not annealed in a oven. The results of Sylvester were also unexpected as the lifetime was only 6.39 hr even in the absence of metal. This lifetime was shorter than that of GoldenVec and GoldenVec2. At this point, we narrowed down the causes of such short lifetime to the last two: 1. The melt of the GE180 glass had too much impurities. 2. Insufficient annealing resulted in more remaining micro-fissures in the glass.

The first possibility is easy to understand and could be easily tested with a simple spherical cell built from the same melt of GE180. Kappa1 was produced for this exact purpose. Hybrid Mixture of Rb and K was used instead of Rb because Kappa1 was also intended for future measurements of the physical quantity κ_0 which require hybrid mixtures. Kappa1 was found to have a lifetime of 72 hr, so the cause of high relaxation in previous GE180 cells was not the melt itself.

As mentioned in previous sections, to keep the glass-metal seals intact, all glass parts not directly attached to metal tubes were placed in a oven for annealing. Larger amount of micro-fissures could still exist in the glass directly attached to metal. This could potentially lead to the short lifetime we observed with the GE180 cells up to this point. To test the hypothesis, Goldfinger180 was built following the design of Goldfinger. However, the glass directly attached to the metal tube that did not go into the oven was intentionally made shorter by our glassblower. During the fill process, a leak at the Houskeeper seal had to be fixed with two coats of an epoxy sealant Stycast 1266. The lifetime was measured to be 10.4 hr before elevation, and

12.4 hr after elevating in the same manner as Goldrush and Pyrah. The result both demonstrated the feasibility of using gold coated OFHC copper with GE180 and further confirmed the significance of glass annealing.

5.6.6 Titanium Tubes

Although gold coated OFHC copper was the main focus of the study due to the ease of manufacturing, titanium was also investigated for its stronger tensile strength. However, the results of the two titanium cells were not satisfactory. A test cell with bare titanium tube, Titan, had lifetime too short to be measured. The other cell TitanVec with gold coated titanium tube had lifetime of only 0.52 hr. Because of the difficulty in coating gold onto titanium surface, parts of gold coating peeled off the surface during the cleaning process with our ultrasonic cleaner. ^3He was exposed to part of the titanium surface underneath, which could be the reason for the bad relaxation properties. As a result, titanium was not investigated further.

Chapter 6

Conclusions and Discussion

The work presented in this thesis has made it possible to design and begin producing the next-generation polarized ^3He targets for use at Jefferson Laboratory. These next-generation targets are being developed and produced in two steps, which are referred to internally at JLab as the Stage-I and Stage-II designs. The Stage-I targets contain a volume of 3 STP liters of ^3He , the same quantity that was contained in the cell Antoinette, the results from which were described in Chapter 4. The Stage-II targets, while similar in geometry, are larger and will contain 6 STP liters of ^3He . At the time of this writing, the first Stage-I target cell has already been produced and is undergoing bench tests. When using only half the design laser power, the target has already achieved a polarization of 65%, higher than what is needed for actual running (although we note that this is without the depolarizing effects of an electron beam). These early tests are quite encouraging when extrapolated to the full laser power that will be used. Also, the conceptual design of the Stage-II target cells has been completed, and was evaluated in a review, conducted in March of 2016, of the polarized ^3He target that is being built for the Hall A Super Bigbite Spectrometer (SBS) experiment to measure G_E^n (E12-09-016), the electric form factor of the neutron.

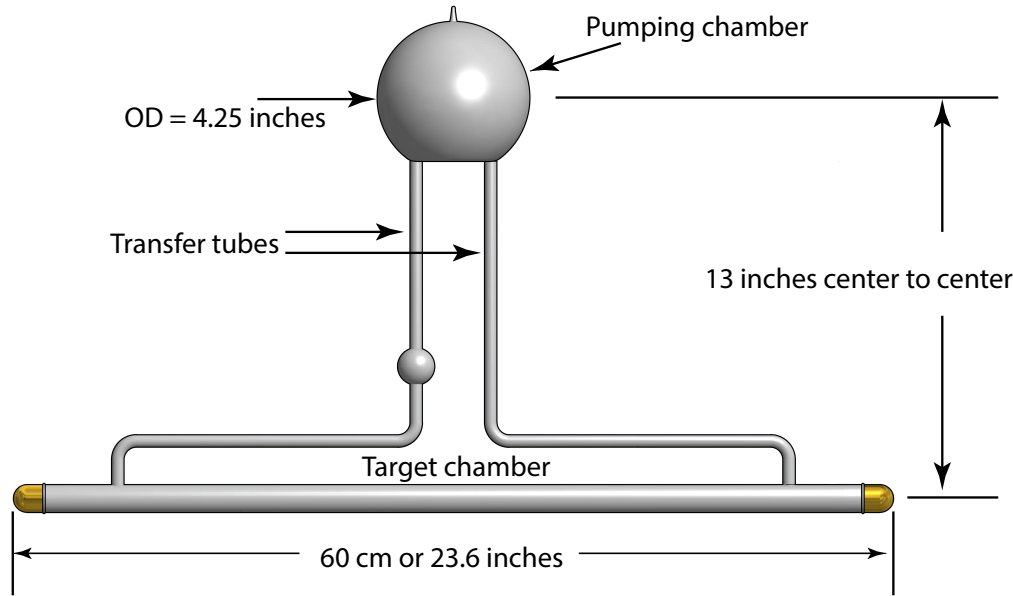


Figure 6.1: Design of next-generation target for upcoming SBS G_E^n experiments.

The design for the SBS G_E^n target is shown in Fig 6.1.

6.1 Overall Design of Next-Generation Polarized ^3He Targets

The target-cell design illustrated in Fig. 6.1 incorporates multiple features that distinguish it from earlier polarized ^3He targets based on spin-exchange optical pumping. The basic geometry is what we refer to as a “convection-style” cell, in which the pumping and target chambers are connected by two transfer tubes, one of which is heated, resulting in controllable convective flow between the target’s two principle chambers. The development of convection-style cells was an important part of the thesis work of Peter Dolph, and is well documented in Ref. [19]. Subsequent to the work described in [19], our group constructed and tested two convection-style prototype target cells.

Another distinguishing feature of the design shown in Fig. 6.1 is that it is sig-

nificantly larger than previous target cells, containing 6 STP liters of ^3He , and has a target chamber that is 60 cm in length, 50% longer than any target cells previously operated at JLab. The confidence that this target will achieve polarization $> 60\%$ in $60 \mu\text{A}$ of beam came as a direct result of the work described in Chapter 4, and published in Ref. [18]. While much of the data presented in Ref. [18] were obtained prior to the work described here, most of the analysis was performed as part of this work, including a determination of the coefficient characterizing spin-exchange between potassium and ^3He .

Data included in ref. [18] that were specifically obtained as part of this thesis work included all of the studies of the cell Antoinette, which contained roughly 3 STP liters of ^3He . While target-cells containing 3 STP liters of ^3He were used during the first Hall A G_E^n experiment (E02-013), commercial narrow-band high-power diode-laser arrays, which are critical to achieving high performance, were not yet available during both testing and the experiment itself. Thus, Antoinette was the first target cell tested with narrow-band lasers that contained both 3 STP liters of ^3He and an alkali-hybrid mixture for optical pumping. As such, Antoinette became a proof of principle for both of the above-mentioned prototype convection-style target cells, as well as the first production Stage-I target cell that is undergoing testing at the time of this writing.

In short, the work presented here provided the basis for designing the high-performance Stage-I and Stage-II target cells that will be used in future JLab experiments. The proof-of-principle began with the cell Antoinette, and continued with the two prototype convection-style target cells (both of which also contained roughly 3 STP liters of ^3He). The first actual Stage-I target cell looks very promising in early tests, providing further confidence in the design of the Stage-II target cells that will soon be produced.

6.2 Incorporating Metal End Windows

Prior to the work described here, there was only very limited experience with spin-polarized noble gases in cells containing metal. The reason is that the introduction of any new material generally causes spin relaxation greatly in excess to that caused by the walls of the glass container. The target-cell design shown in Fig. 6.1, however, incorporates metal end windows so that even a fairly intense electron beam will not cause the target cell to rupture, even after multiple weeks of operation. One of the important achievements of the current work was the development of a technique for producing metal surfaces that induce spin relaxation at an acceptably slow rate. We further have demonstrated a means for making transitions between glass and metal, even when operating at the high pressures used in our polarized ${}^3\text{He}$ targets. We describe next why metal end windows based on the techniques demonstrated here are likely to have an almost negligible effect on the overall performance of our target cells.

The spin relaxation caused by metal end windows in future target cells can be calculated using the equation $\Gamma_{metal} = \rho_{metal} S_{metal} / V_{total}$ (see Chapter 2.4). Furthermore, the relaxivity associated with metal can be extracted by comparing a glass-and-metal test cell (such as GoldRush in Table. 5.1) with an all-glass control cell (such as Pyrah in Table.5.1). The relaxivity for Pyrah can be computed to be 0.0314 cm/hr⁻¹, and when compared with GoldRush, indicates a relaxivity of 0.123 cm/hr⁻¹ for the metal. Using this relaxivity and the design dimensions for the target end windows, the additional relaxation times would be 1/93.06 hr⁻¹ for Stage-I cells and 1/186.12 hr⁻¹ for Stage-II cells.

During the 6 GeV era where only 10-15 μA was used, glass end windows were already running into risk of rupturing after 4-6 weeks of being exposed to the electron

beam. If rupturing was solely due to radiation damage, one would expect the glass windows to rupture after roughly a week of being used in an electron beam of $60 \mu\text{A}$, which would be much less than the time required for the experiment to complete. On the other hand, experience at JLab suggests that even very thin metal windows would be able to survive the electron beam. As a an example, aluminum as thin as 2 mils has been routinely used in JLab without failing. The fact that metal end windows will conduct heat better further suggests that they will be more suitable for the planned experiment. While some work remains to determine the optimal configuration for the window itself, the work presented here provides the critical technology that previously prevented us from using metal end windows in our targets.

6.3 Summary

We have confidence that convection style targets with metal end windows will not only give high ^3He polarization in both the pumping and target chambers, but also survive the high electron beam currents planned for the future experiments. The work done in this thesis has demonstrated that the additional spin-relaxation rate due to surfaces in metal end windows will be negligible for our purposes and has provided techniques for connecting metal end windows to glass. All the tests so far have been performed on test cells with metal tubes. Before a target cell with next-generation design can be produced, tests exploring techniques for making hemispherical metal end caps should be carried out. However, with techniques established so far, we believe the next-generation design will be used to great success in the upcoming experiments planned for the 12 GeV era.

Bibliography

- [1] Thad G. Walker and William Happer. Spin-exchange optical pumping of noble-gas nuclei. *Rev. Mod. Phys.*, 69:629–642, Apr 1997. (Cited on p. [xii](#), [9](#), [13](#), [19](#), [21](#), [22](#), [23](#), [24](#), [59](#))
- [2] M. V. Romalis, E. Miron, and G. D. Cates. Pressure broadening of rb d₁ and d₂ lines by ³he, ⁴he, n₂, and xe: line cores and near wings. *Phys. Rev. A*, 56(6), 1997. (Cited on p. [xii](#), [15](#), [16](#), [63](#))
- [3] High-performance nuclear-polarized ³He targets for electron scattering based on spin-exchange optical pumping. *PhD thesis, University of Virginia*, 2010. (Cited on p. [xiii](#), [49](#), [50](#), [71](#))
- [4] Inc. Delstar Metal Finishing. <https://www.delstar.com/electropolishing>. (Cited on p. [xv](#), [94](#), [95](#))
- [5] Daniel Matyas. Characterizing ³he nuclear spin relaxation in vessels of glass and metal. *Master thesis, University of Virginia*, 2016. (Cited on p. [xv](#), [97](#), [98](#))
- [6] Yuan Zheng. Low field mri and the development of polarized nuclear imaging (pni)-a new imaging modality, 2015. (Cited on p. [xv](#), [102](#), [104](#), [106](#))
- [7] P. L. Anthony, R. G. Arnold, H. R. Band, H. Borel, P. E. Bosted, V. Breton, G. D. Cates, T. E. Chupp, F. S. Dietrich, J. Dunne, R. Erbacher, J. Fellbaum,

- H. Fonvieille, R. Gearhart, R. Holmes, E. W. Hughes, J. R. Johnson, D. Kawall, C. Keppel, S. E. Kuhn, R. M. Lombard-Nelsen, J. Marroncle, T. Maruyama, W. Meyer, Z.-E. Meziani, H. Middleton, J. Morgenstern, N. R. Newbury, G. G. Petratos, R. Pitthan, R. Prepost, Y. Roblin, S. E. Rock, S. H. Rokni, G. Shapiro, T. Smith, P. A. Souder, M. Spengos, F. Staley, L. M. Stuart, Z. M. Szalata, Y. Terrien, A. K. Thompson, J. L. White, M. Woods, J. Xu, C. C. Young, and G. Zapalac. Determination of the neutron spin structure function. *Phys. Rev. Lett.*, 71:959–962, Aug 1993. (Cited on p. 1, 3, 8)
- [8] M. S. Albert, G. D. Cates, B. Driehuys, W. Happer, B. Saam, C. S. Springer, and A. Wishnia. Biological magnetic resonance imaging using laser-polarized ^{129}xe . *Nature*, 370. (Cited on p. 1)
- [9] M. G. Huber, M. Arif, T. C. Black, W. C. Chen, T. R. Gentile, D.S. Hussey, D. A. Pushin, F. E. Wietfeldt, and L. Yang. Precision measurement of the $n-^3\text{He}$ incoherent scattering length using neutron interferometry. 102, 2009. (Cited on p. 1)
- [10] Gerald A. Miller. Charge densities of the neutron and proton. *Phys. Rev. Lett.*, 99:112001, Sep 2007. (Cited on p. 1)
- [11] C. E. Carlson and M. Vanderhaeghen. Empirical transverse charge densities in the nucleon and the nucleon-to- δ transition. *Phys. Rev. Lett.*, 100:032004, Jan 2008. (Cited on p. 1)
- [12] M. K. Jones, K. A. Aniol, F. T. Baker, J. Berthot, P. Y. Bertin, W. Bertozzi, A. Besson, L. Bimbot, W. U. Boeglin, E. J. Brash, D. Brown, J. R. Calarco, L. S. Cardman, C.-C. Chang, J.-P. Chen, E. Chudakov, S. Churchwell, E. Cisbani, D. S. Dale, R. De Leo, A. Deur, B. Diederich, J. J. Domingo, M. B. Epstein, L. A.

- Ewell, K. G. Fissum, A. Fleck, H. Fonvieille, S. Frullani, J. Gao, F. Garibaldi, A. Gasparian, G. Gerstner, S. Gilad, R. Gilman, A. Glamazdin, C. Glashausser, J. Gomez, V. Gorbenko, A. Green, J.-O. Hansen, C. R. Howell, G. M. Huber, M. Iodice, C. W. de Jager, S. Jaminion, X. Jiang, W. Kahl, J. J. Kelly, M. Khayat, L. H. Kramer, G. Kumbartzki, M. Kuss, E. Lakuriki, G. Lavessière, J. J. LeRose, M. Liang, R. A. Lindgren, N. Liyanage, G. J. Lolos, R. Macri, R. Madey, S. Malov, D. J. Margaziotis, P. Markowitz, K. McCormick, J. I. McIn tyre, R. L. J. van der Meer, R. Michaels, B. D. Milbrath, J. Y. Mougey, S. K. Nanda, E. A. J. M. Offermann, Z. Papandreou, C. F. Perdrisat, G. G. Petratos, N. M. Piskunov, R. I. Pomatsalyuk, D. L. Prout, V. Punjabi, G. Quéméner, R. D. Ransome, B. A. Raue, Y. Roblin, R. Roche, G. Rutledge, P. M. Rutt, A. Saha, T. Saito, A. J. Sarty, T. P. Smith, P. Sorokin, S. Strauch, R. Suleiman, K. Takahashi, J. A. Templon, L. Todor, P. E. Ulmer, G. M. Urciuoli, P. Vernin, B. Vlahovic, H. Voskanyan, K. Wijesooriya, B. B. Wojtsekhowski, R. J. Woo, F. Xiong, G. D. Zainea, and Z.-L. Zhou. G_{E_p}/G_{M_p} ratio by polarization transfer in $\vec{e} p \rightarrow e \vec{p}$. *Phys. Rev. Lett.*, 84:1398–1402, Feb 2000. (Cited on p. 2)
- [13] S. Riordan, S. Abrahamyan, B. Craver, A. Kelleher, A. Kolarkar, J. Miller, G.D. Cates, N. Liyanage, B. Wojtsekhowski, A. Acha, K. Allada, B. Anderson, K.A. Aniol, J.R.M. Annand, J. Arrington, T. Averett, A. Beck, M. Bellis, W. Boeglin, H. Breuer, J.R. Calarco, A. Camsonne, J.P. Chen, E. Chudakov, L. Coman, B. Crowe, F. Cusanno, D. Day, P. Degtyarenko, P.A.M. Dolph, C. Dutta, C. Ferdi, C. Fernandez-Ramirez, R. Feuerbach, L.M. Fraile, G. Franklin, S. Frullani, S. Fuchs, F. Garibaldi, N. Gevorgyan, Gilman R., A. Glamazdin, J. Gomez, K. Grimm, J.-O. Hansen, J.L. Herraiz, D.W. Hig inbotham, R. Holmes, T. Holmstrom, D. Howell, C.W. de Jager, X. Jiang, M.K.

Jones, J. Katich, L.J. Kaufman, M. Khandaker, J.J. Kelly, D. Kiselev, W. Korsch, J. LeRose, R. Lindgren, P. Markowitz, D.J. Margaziotis, S. May-Tal Beck, S. Mayilyan, K. McCormick, Z.-E. Meziani, R. Michaels, B. Moffit, S. Nanda, V. Nelyubin, T. Ngo, D.M. Nikolenko, B. Norum, L. Pentchev, C.F. Perdrisat, E. Piasetzky, R. Pomatsalyuk, D. Protopopescu, A.J.R. Puckett, V.A. Punjabi, X. Qian, Y. Qiang, B. Quinn, I. Rachek, R.D. Ransome, P.E. Reimer, B. Reitz, J. Roche, G. Ron, O. Rondon, G. Rosner, A. Saha, M.M. Sargsian, B. Sawatzky, M. J. Segal, Shabestari, A. Shahinyan, Yu. Shestakov, J. Singh, S. Sirca, P. Souder, S. Stepanyan, V. Stibunov, V. Sulkosky, S. Tajima, W.A. Tobias, J.M. Udiás, G.M. Urciuoli, B. Vlahovic, H. Voskanyan, K. Wang, F.R. Wesselmann, J.R. Vignote, S.A. Wood, J. Wright, H. Yao, and X. Zhu. Measurements of the electric form factor of the neutron up to $q^2 = 3.4$ gev 2 using the reaction ${}^3\text{He}(\vec{e}, e'n)pp$. *Phys. Rev. Lett.*, 105:262302, Dec 2010. (Cited on p. 2)

- [14] G. D. Cates, C. W. de Jager, S. Riordan, and B. Wojtsekhowski. Flavor decomposition of the elastic nucleon electromagnetic form factors. *Phys. Rev. Lett.*, 106:252003, Jun 2011. (Cited on p. 2)
- [15] I.C. et al. Cloet. *Few-Body Syst.*, 46, 2009. (Cited on p. 2)
- [16] X. Qian, K. Allada, C. Dutta, J. Huang, J. Katich, Y. Wang, Y. Zhang, K. Aniol, J. R. M. Annand, T. Averett, F. Benmokhtar, W. Bertozzi, P. C. Bradshaw, P. Bosted, A. Camsonne, M. Canan, G. D. Cates, C. Chen, J.-P. Chen, W. Chen, K. Chirapatpimol, E. Chudakov, E. Cisbani, J. C. Cornejo, F. Cusanno, M. M. Dalton, W. Deconinck, C. W. de Jager, R. De Leo, X. Deng, A. Deur, H. Ding, P. A. M. Dolph, D. Dutta, L. El Fassi, S. Frullani, H. Gao, F. Garibaldi, D. Gaskell, S. Gilad, R. Gilman, O. Glamazdin, S. Golge, L. Guo, D. Hamil-

- ton, O. Hansen, D. W. Higinbotham, T. Holmstrom, M. Huang, H. F. Ibrahim, M. Iodice, X. Jiang, G. Jin, M. K. Jones, A. Kelleher, W. Kim, A. Kolarkar, W. Korsch, J. J. LeRose, X. Li, Y. Li, R. Lindgren, N. Liyanage, E. Long, H.-J. Lu, D. J. Margaziotis, P. Markowitz, S. Marrone, D. McNulty, Z.-E. Meziani, R. Michaels, B. Moffit, C. Muñoz Camacho, S. Nanda, A. Narayan, V. Nelyubin, B. Norum, Y. Oh, M. Osipenko, D. Parno, J. C. Peng, S. K. Phillips, M. Posik, A. J. R. Puckett, Y. Qiang, A. Rakhman, R. D. Ransome, S. Riordan, A. Saha, B. Sawatzky, E. Schulte, A. Shahinyan, M. H. Shabestari, S. Širca, S. Stepanyan, R. Subedi, V. Sulkosky, L.-G. Tang, A. Tobias, G. M. Urciuoli, I. Vilardi, K. Wang, B. Wojtsekhowski, X. Yan, H. Yao, Y. Ye, Z. Ye, L. Yuan, X. Zhan, Y.-W. Zhang, B. Zhao, X. Zheng, L. Zhu, X. Zhu, and X. Zong. Single spin asymmetries in charged pion production from semi-inclusive deep inelastic scattering on a transversely polarized ${}^3\text{He}$ target at $Q^2 = 1.4 \sim 2.7$ gev^2 . *Phys. Rev. Lett.*, 107:072003, Aug 2011. (Cited on p. 3, 8)
- [17] E. Babcock, B. Chann, T. G. Walker, W. C. Chen, and T. R. Gentile. Limits to the polarization for spin-exchange optical pumping of ${}^3\text{He}$. *Phys. Rev. Lett.*, 96:083003, Mar 2006. (Cited on p. 4, 28, 74, 76, 77, 81)
- [18] Jaideep T. Singh, P. A. M. Dolph, W. A. Tobias, T. D. Averett, A. Kelleher, K. E. Mooney, V. V. Nelyubin, Yunxiao Wang, Yuan Zheng, and G. D. Cates. Development of high-performance alkali-hybrid polarized ${}^3\text{He}$ targets for electron scattering. *Phys. Rev. C*, 91:055205, May 2015. (Cited on p. 4, 58, 124)
- [19] P. A. M. Dolph, J. Singh, T. Averett, A. Kelleher, K. E. Mooney, V. Nelyubin, W. A. Tobias, B. Wojtsekhowski, and G. D. Cates. Gas dynamics in high-luminosity polarized ${}^3\text{He}$ targets using diffusion and convection. *Phys. Rev. C*, 84:065201, Dec 2011. (Cited on p. 5, 60, 64, 66, 67, 123)

- [20] W. G. Houskeeper. The art of sealing base metals through glass. *Transactions of the American Institute of Electrical Engineers*, XLII:870–877, 1923. (Cited on p. 5, 90, 91)
- [21] M. Amarian, L. Auerbach, T. Averett, J. Berthot, P. Bertin, W. Bertozzi, T. Black, E. Brash, D. Brown, E. Burtin, J. R. Calarco, G. D. Cates, Z. Chai, J.-P. Chen, Seonho Choi, E. Chudakov, E. Cisbani, C. W. de Jager, A. Deur, R. DiSalvo, S. Dieterich, P. Djawotho, M. Finn, K. Fissum, H. Fonvieille, S. Frullani, H. Gao, J. Gao, F. Garibaldi, A. Gasparian, S. Gilad, R. Gilman, A. Glamazdin, C. Glashausser, E. Goldberg, J. Gomez, V. Gorbenko, J.-O. Hansen, F. W. Hersman, R. Holmes, G. M. Huber, E. W. Hughes, T. B. Humensky, S. Incerti, M. Iodice, S. Jensen, X. Jiang, C. Jones, G. M. Jones, M. Jones, C. Jutier, A. Ketikyan, I. Kominis, W. Korsch, K. Kramer, K. S. Kumar, G. Kumbaratzki, M. Kuss, E. Lakuriqi, G. Laveissiere, J. Lerose, M. Liang, N. Liyanage, G. Lolos, S. Malov, J. Marroncle, K. McCormick, R. McKeown, Z.-E. Meziani, R. Michaels, J. Mitchell, Z. Papandreou, T. Pavlin, G. G. Petratos, D. Pripstein, D. Prout, R. Ransome, Y. Roblin, D. Rowntree, M. Rvachev, F. Sabatie, A. Saha, K. Slifer, P. A. Souder, T. Saito, S. Strauch, R. Suleiman, K. Takahashi, S. Teijiro, L. Todor, H. Tsubota, H. Ueno, G. Urchioli, R. Van der Meer, P. Vernin, H. Voskanian, B. Wojtsekhowski, F. Xiong, W. Xu, J.-C. Yang, B. Zhang, and P. Zolnierczuk. Q^2 evolution of the generalized gerasimov-drell-hearn integral for the neutron using a ${}^3\text{He}$ target. *Phys. Rev. Lett.*, 89:242301, Nov 2002. (Cited on p. 8)
- [22] S. Riordan, S. Abrahamyan, B. Craver, A. Kelleher, A. Kolarkar, J. Miller, G. D. Cates, N. Liyanage, B. Wojtsekhowski, A. Acha, K. Allada, B. Anderson, K. A. Aniol, J. R. M. Annand, J. Arrington, T. Averett, A. Beck, M. Bel-

- lis, W. Boeglin, H. Breuer, J. R. Calarco, A. Camsonne, J. P. Chen, E. Chudakov, L. Coman, B. Crowe, F. Cusanno, D. Day, P. Degtyarenko, P. A. M. Dolph, C. Dutta, C. Ferdi, C. Fernández-Ramírez, R. Feuerbach, L. M. Fraile, G. Franklin, S. Frullani, S. Fuchs, F. Garibaldi, N. Gevorgyan, R. Gilman, A. Glamazdin, J. Gomez, K. Grimm, J.-O. Hansen, J. L. Herraiz, D. W. Higinbotham, R. Holmes, T. Holmstrom, D. Howell, C. W. de Jager, X. Jiang, M. K. Jones, J. Katich, L. J. Kaufman, M. Khandaker, J. J. Kelly, D. Kiselev, W. Korsch, J. LeRose, R. Lindgren, P. Markowitz, D. J. Margaziotis, S. May-Tal Beck, S. Mayilyan, K. McCormick, Z.-E. Meziani, R. Michaels, B. Moffit, S. Nanda, V. Nelyubin, T. Ngo, D. M. Nikolenko, B. Norum, L. Pentchev, C. F. Perdrisat, E. Piasetzky, R. Pomatsalyuk, D. Protopopescu, A. J. R. Puckett, V. A. Punjabi, X. Qian, Y. Qiang, B. Quinn, I. Racheck, R. D. Ransome, P. E. Reimer, B. Reitz, J. Roche, G. Ron, O. Rondon, G. Rosner, A. Saha, M. M. Sargsian, B. Sawatzky, J. Segal, M. Shabestari, A. Shahinyan, Yu. Shestakov, J. Singh, S. Širca, P. Souder, S. Stepanyan, V. Stibunov, V. Sulkosky, S. Tajima, W. A. Tobias, J. M. Udiás, G. M. Urciuoli, B. Vlahovic, H. Voskanyan, K. Wang, F. R. Wesselmann, J. R. Vignote, S. A. Wood, J. Wright, H. Yao, and X. Zhu. Measurements of the electric form factor of the neutron up to $Q^2 = 3.4$ gev^2 using the reaction ${}^3\text{he} \xrightarrow{\gamma} (\vec{e}, e'n)pp$. *Phys. Rev. Lett.*, 105:262302, Dec 2010. (Cited on p. 8)
- [23] F. D. Colegrove, L. D. Schearer, and G. K. Walters. Polarization of he^3 gas by optical pumping. *Phys. Rev.*, 132:2561–2572, Dec 1963. (Cited on p. 8)
- [24] T. E. Chupp, M. E. Wagshul, K. P. Coulter, A. B. McDonald, and W. Happer. Polarized, high-density, gaseous ${}^3\text{He}$ targets. *Phys. Rev. C*, 36:2244–2251, Dec 1987. (Cited on p. 8)

- [25] B. Larson, O. Hausser, P. P. J. Delheij, D. M. Whittal, and D. Thiessen. Optical pumping of rb in the presence of high-pressure ${}^3\text{He}$ buffer gas. *Phys. Rev. A*, 44:3108–3118, Sep 1991. (Cited on p. 16)
- [26] N. R. Newbury, A. S. Barton, P. Bogorad, G. D. Cates, M. Gatzke, B. Saam, L. Han, R. Holmes, P. A. Souder, J. Xu, and D. Benton. Laser polarized muonic helium. *Phys. Rev. Lett.*, 67:3219–3222, Dec 1991. (Cited on p. 8, 27)
- [27] M. A. Bouchiat, T. R. Carver, and C. M. Varnum. Nuclear polarization in he^3 gas induced by optical pumping and dipolar exchange. *Phys. Rev. Lett.*, 5:373–375, Oct 1960. (Cited on p. 8)
- [28] W. Happer, G.D. Cates, M.V. Romalis, and C.J. Erickson. U.s. patent no. 6318092. 2001. (Cited on p. 9)
- [29] Earl Babcock, Ian Nelson, Steve Kadlecik, Bastiaan Driehuys, L. W. Anderson, F. W. Hersman, and Thad G. Walker. Hybrid spin-exchange optical pumping of ${}^3\text{He}$. *Phys. Rev. Lett.*, 91:123003, Sep 2003. (Cited on p. 9, 59)
- [30] Alcock C., V. Itkin, and H. M.K. *Canadian Metallurgical Quarterly*, 23, 1984. (Cited on p. 10)
- [31] S. Appelt, A. Ben-Amar Baranga, C. J. Erickson, M. V. Romalis, A. R. Young, and W. Happer. Theory of spin-exchange optical pumping of ${}^3\text{He}$ and ${}^{129}\text{Xe}$. *Phys. Rev. A*, 58:1412–1439, Aug 1998. (Cited on p. 10)
- [32] M.E Wagshul and T.E. Chupp. Optical pumping of high-density rb with a broad-band dye laser and gaalas diode laser arrays: Application to ${}^3\text{he}$ polarization. *Phys. Rev. A.*, 40, 1989. (Cited on p. 14)
- [33] E. Merzbacher. *Quantum Mechanics*. 1998. (Cited on p. 16)

- [34] M.E. Wagshul and T.E. Chupp. Laser optical pumping of high-density rb in polarized ^3He targets. *Phys. Rev. A*, 49:3854–3869, 1994. (Cited on p. 20)
- [35] L. D. Schearer, F. D. Colegrove, and G. K. Walters. Large He^3 nuclear polarization. *Phys. Rev. Lett.*, 10:108–110, Feb 1963. (Cited on p. 20)
- [36] D. K. Walter, W. Happer, and T. G. Walker. Estimates of the relative magnitudes of the isotropic and anisotropic magnetic-dipole hyperfine interactions in alkali-metal–noble-gas systems. *Phys. Rev. A*, 58:3642–3653, Nov 1998. (Cited on p. 25)
- [37] A. Ben-Amar Baranga, S. Appelt, M. V. Romalis, C. J. Erickson, A. R. Young, G. D. Cates, and W. Happer. Polarization of ^3He by spin exchange with optically pumped rb and k vapors. *Phys. Rev. Lett.*, 80:2801–2804, Mar 1998. (Cited on p. 26, 59, 72)
- [38] Rodger L. Gamblin and Thomas R. Carver. Polarization and relaxation processes in He^3 gas. *Phys. Rev.*, 138:A946–A960, May 1965. (Cited on p. 27, 38)
- [39] L. D. Schearer and G. K. Walters. Nuclear spin-lattice relaxation in the presence of magnetic-field gradients. *Phys. Rev.*, 139:A1398–A1402, Aug 1965.
- [40] G. D. Cates, S. R. Schaefer, and W. Happer. Relaxation of spins due to field inhomogeneities in gaseous samples at low magnetic fields and low pressures. *Phys. Rev. A*, 37:2877–2885, Apr 1988. (Cited on p. 27, 38, 39, 103)
- [41] A. Abragam. *Principles of Nuclear Magnetism*. (Cited on p. 30, 63, 86)
- [42] M. V. Romalis and G. D. Cates. Accurate ^3He polarimetry using the rb zee-mann frequency shift due to the Rb– ^3He spin-exchange collisions. *Phys. Rev. A*, 58:3004–3011, Oct 1998. (Cited on p. 30, 41, 44)

- [43] I. I. Rabi, N. F. Ramsey, and J. Schwinger. Use of rotating coordinates in magnetic resonance problems. *Rev. Mod. Phys.*, 26:167–171, Apr 1954. (Cited on p. 32, 33)
- [44] G. D. Cates, D. J. White, Ting-Ray Chien, S. R. Schaefer, and W. Happer. Spin relaxation in gases due to inhomogeneous static and oscillating magnetic fields. *Phys. Rev. A*, 38:5092–5106, Nov 1988. (Cited on p. 35, 39)
- [45] Earl Babcock, Ian A. Nelson, Steve Kadlecak, and Thad G. Walker. ^3He polarization-dependent epr frequency shifts of alkali-metal- ^3He pairs. *Phys. Rev. A*, 71:013414, Jan 2005. (Cited on p. 41, 44)
- [46] G. Breit and I. I. Rabi. Measurement of nuclear spin. *Phys. Rev.*, 38:2082–2083, Dec 1931. (Cited on p. 42)
- [47] J.D. Jackson. *Classical Electrodynamics*. (Cited on p. 44)
- [48] F. Bloch. Nuclear induction. *Phys. Rev.*, 70:460–474, Oct 1946. (Cited on p. 53)
- [49] M. Leduc R. Barbe and F. Laloe. Experimental verifications - measurement of the $\text{he}3$ self-diffusion coefficient. 35:935–951, 1974. (Cited on p. 56)
- [50] W. C. Chen, T. R. Gentile, T. G. Walker, and E. Babcock. Spin-exchange optical pumping of ^3He with rb-k mixtures and pure k. *Phys. Rev. A*, 75:013416, Jan 2007. (Cited on p. 59)
- [51] Thad G. Walker, Joseph H. Thywissen, and William Happer. Spin-rotation interaction of alkali-metal- he -atom pairs. *Phys. Rev. A*, 56:2090–2094, Sep 1997. (Cited on p. 59)

- [52] B. Chann, E. Babcock, L.W. Anderson, T.G. Walker, W.C. Chen, T.B. Smith, A.K. Thompson, and T.R. Gentile. Production of highly polarized ${}^3\text{He}$ using spectrally narrowed diode laser array bars. *Journal of applied physcis*, 94:6908–6914. (Cited on p. 59)
- [53] B. Chann, E. Babcock, L. W. Anderson, and T. G. Walker. Measurements of ${}^3\text{He}$ spin-exchange rates. *Phys. Rev. A*, 66:032703, Sep 2002. (Cited on p. 72)
- [54] Spin-exchange optical pumping with alkali-metal vapors. *PhD thesis, University of Wisconsin-Madison*, 2005. (Cited on p. 73)
- [55] N. R. Newbury, A. S. Barton, G. D. Cates, W. Happer, and H. Middleton. Gaseous ${}^3-{}^3\text{He}$ magnetic dipolar spin relaxation. *Phys. Rev. A*, 48:4411–4420, Dec 1993. (Cited on p. 76)
- [56] Alkali-hybrid spin-exchange optically-pumped polarized ${}^3\text{He}$ targets used for studying neutron structure. *PhD thesis, University of Virginia*, 2010. (Cited on p. 76)
- [57] T. G. Walker, I. A. Nelson, and S. Kadlecak. Method for deducing anisotropic spin-exchange rates. *Phys. Rev. A*, 81:032709, Mar 2010. (Cited on p. 82)
- [58] T. V. Tscherbul, P. Zhang, H. R. Sadeghpour, and A. Dalgarno. Anisotropic hyperfine interactions limit the efficiency of spin-exchange optical pumping of ${}^3\text{He}$ nuclei. *Phys. Rev. Lett.*, 107:023204, Jul 2011. (Cited on p. 82)
- [59] J. Schmiedeskamp, W. Heil, W. E. Otten, K. R. Kremer, A. Simon, and J. Zimmer. Paramagnetic relaxation of spin polarized ${}^3\text{He}$ at bare glass surfaces. *The European Physical Journal D - Atomic, Molecular, Optical and Plasma Physics*, 38(3):427–438, 2006. (Cited on p. 83)

- [60] W. A. Fitzsimmons, L. L. Tankersley, and G. K. Walters. Nature of surface-induced nuclear-spin relaxation of gaseous he^3 . *Phys. Rev.*, 179:156–165, Mar 1969. (Cited on p. 84, 88)
- [61] Nuclear relaxation of ${}^3\text{he}$ gas on various solid surfaces. *Canadian Journal of Physics*, 1971. (Cited on p. 85, 88, 89)
- [62] Charles Kittel. *Introduction to Solid State Physics*. (Cited on p. 86)
- [63] J. Frenkel. *Kinetic Theory of Liquids*. (Cited on p. 86, 87)
- [64] W. Heil, H. Humblot, E Otten, M Schafer, R Sarkau, and M Leduc. Very long nuclear relaxation times of spin-polarized ${}^3\text{he}$ in metal coated cells. *Phys. Rev. A*, 201:337–343, May 1995. (Cited on p. 88)
- [65] Ming F. Hsu, G. D. Cates, I. Kominis, I. A. Aksay, and D. M. Dabbs. Sol-gel coated glass cells for spin-exchange polarized ${}^3\text{He}$. *Applied Physics Letters*, 77(13):2069–2071, 2000. (Cited on p. 88)
- [66] R. M. Barrer. *Diffusion in and through Solids*. (Cited on p. 88)
- [67] W. Smythe. *Static and Dynamic Electricity*. (Cited on p. 88)
- [68] J. Korringa. Nuclear magnetic relaxation and resonance line shift in metals. *Physica*, 16, 1950. (Cited on p. 89)
- [69] C. P. Slichter. *Principles of Magnetic Resonance*. (Cited on p. 89)
- [70] Physics of practical spin-exchange optical pumping. *PhD thesis, University of Wisconsin-Madison*, 2001. (Cited on p. 89)
- [71] Larson Electronic Glass. <http://www.larsonelectronicglass.com>. (Cited on p. 91)

- [72] Able Electropolishing Advanced Metal Improvement Technologies. *http://www.ableelectropolishing.com.* (Cited on p. 91)
- [73] Epner Technology Inc. *http://www.epner.com.* (Cited on p. 91)
- [74] G. D. Cates. Polarized targets in high energy physics. *Proceedings of the 1993 Summer Institute on Particle Physics: Spin Structure in High Energy Processes (SSI93)*, SLAC-R-444:185–207, 1993. (Cited on p. 91)
- [75] A. Deninger, W. Heil, W. E. Otten, M. Wolf, K. R. Kremer, and A. Simon. Paramagnetic relaxation of spin polarized ^3He at coated glass walls. *The European Physical Journal D - Atomic, Molecular, Optical and Plasma Physics*, 38(3):439–443, 2006. (Cited on p. 94)
- [76] P. Callaghan. *Principles of Nuclear Magnetic Resonance Microscopy*. (Cited on p. 101)